Quantifying Flood Depth:

Remote Estimation of Flood Depths with Fast Response Tools
by

Roberto Javier Escobar Mou

A thesis submitted in partial fulfillment of the requirements for the degree of

Master of Science
in Water Resources Engineering

Department of Civil and Environmental Engineering
University of Alberta

Abstract

Flood depth modelling has seen significant improvements in recent years. Historically, it relied heavily on large datasets, which were difficult to gather and handle. Simple, fast response methods, such as RICorDE and FwDET, are potentially suitable for assessments of flood scenarios where detailed hydraulic data might not be available or necessary. In this study, the performance of flood depth estimation algorithms RICorDE v1.0.1 and FwDET v2.1 was assessed for the 2020 Fort McMurray ice jam flood event. To assess their performance, the models were calibrated using a hand drawn case study event flood extent, and the resulting depth outputs from the fast response models were compared against a calibrated HEC-RAS model from Alberta Environment and Protected Areas (EPA) as well as high water mark (HWM) depths collected for the case study event, also from EPA. In the comparative assessment, the fast response RICorDE model achieved an R^2 value of 0.69 when compared to the calibrated HEC-RAS model, while FwDET achieved a value of 0.86. In relation to the surveyed HWM-derived depths, the fast response tools established point connections with fewer data points than the calibrated HEC-RAS model. In the surveyed depths assessment, RICorDE exhibited a Root Mean Square Error (RMSE) value of 0.58 meters, and FwDET had an RMSE of 0.20 meters. The calibrated HEC-RAS model, to which both fast response models were compared, presented a high point connection with an RMSE difference of 0.41 meters. Additionally, we assessed the Height Above Nearest Drainage (HAND) maps integrated into the fast response model RICorDE as a basis for flood depth estimations. HAND maps represent the elevation of a point on the landscape relative to the nearest stream or drainage network. In their assessment, the discrepancies in elevation points when creating HAND maps using either a stream or drainage network as reference points was evaluated. Specifically, the study investigated the impact of generating HAND maps based on these features on the accuracy of estimating flood extent. The findings indicate that defining drainage as a continuous streamline using flow accumulation algorithms yielded a more precise depiction of flood extent, in contrast to maps where drainage is delineated along the boundary between water and land. In conclusion, the study demonstrated that fast response flood models can generate flood depth estimations with high correlation to observations and physical models, especially in

areas with flat topography and high-quality DEM data. These estimations are highly dependent on accurate delineation of flood extent, which can also be obtained from minimal data using HAND models.

Preface

This report is the result of my graduation research, and it is the final part of the MSc in Water Resource Engineering at University of Alberta. The work for this manuscript was performed under Evan Davies at the department of Civil and Environmental Engineering.

I stumbled across the fast-response estimations of flood depth from Seth Bryant work from the University of Alberta library, this introduced me to the subject of flood depth-damage curves and eventually lead me the fast-response flood depth damage estimations, the subject of this thesis.

I would like to thank my supervisor Evan Davies as well as Seth Bryant for the advises given, discussions, recommendations, and corrections they made to this thesis during this process. I would also like to thank the developers of the fast-response tools evaluated on this thesis Sagy Cohen for developing the FwDET tool, and Seth Bryant for developing RICorDE tool.

Acknowledgements

My deeply generous thanks to all individuals who positively influenced my academic and personal growth during this period. Especially to Dr. Evan Davies, my MSc supervisor, whose guidance and encouragement nurtured my critical thinking. To Seth Bryant for his patient guidance through the technical aspects of this thesis. Dr. Jennifer Nafziger for her assistance with technical aspects of the HEC-RAS model and for measuring and providing the high water marks for the case study event.

To individuals and institutions who assisted during the data collection process, and specifically Dr. Heather McGrath of Natural Resources Canada, and James Choles of Alberta Environment and Protected Areas (AEPA) for generously providing survey elevations, LiDAR imagery, hydrological models, and aerial images.

I express my gratitude to OpenAI for granting access to ChatGPT, a valuable resource that helped me with idea generation, research insights, and grammatical and stylistic edits throughout the research.

Finally, I would like to thank the Panamanian institution, Secretaría Nacional de Ciencia, Tecnología e Innovación (SENACYT), whose funding enabled me to pursue my masters studies at the University of Alberta.

Table of Contents

List of Tables

List of Figures

Glossary of Terms and Acronyms

Digital Elevation Model (DEM)	Representation of the bare ground (bare earth) topographic surface of the Earth excluding trees, buildings, and any other surface objects.
Geographic Information System (GIS)	Computer-based tools used to store, visualize, analyze, and interpret geographic data.
Height Above Nearest Drainage (HAND)	A drainage normalizing terrain index, contains the vertical distance between a location and its nearest stream.
HR-DEM	High Resolution Digital Elevation Model
HWM	High water marks
Hydro-connection	Refers to the interconnectedness or linkage between different elements within a hydrological system. In the context of this research, it describes a successful pathway through which water transfers with a dry DEM cell to the stream or waterbody boundary.
Ice runs	A scenario of river ice breaking apart in the spring and flowing downstream.
Inverse distance weighted (IDW) Interpolation	Determines cell values using a linearly weighted combination of a set of sample points.
Local Drain Direction (LDD)	The natural direction of water flow determined by the terrain's topography.
Light Detection And Ranging (LiDAR)	LiDAR is a type of active remote sensing that measures the elevation of the Earth surface using the round-trip duration of a laser onboard an aerial platform.
Whitebox Tools (WBT)	Standalone geospatial analysis library, a collection of GIS tools contained within a compiled binary executable command.
Water Surface Elevation (WSE)	Refers to the height of the water surface above a specific datum, such as sea level or a local reference point. It represents the vertical position of the water surface.

Water Surface Layer (WSL)	The surface layer of any body of water, be it an ocean, river, or lake. It is the layer that is directly exposed to the atmosphere.

1. Introduction

According to Public Safety Canada (2022), Canada is facing a growing vulnerability to floods, largely due to the impacts of climate change, urban development, infrastructure expansion, and the concentration of assets in flood-prone areas. The Adaptation Action Plan from the Government of Canada (2023a) indicates that ongoing climate trends are expected to amplify the financial impacts of floods on Canadian society in the coming years. It is estimated that a mere inch of floodwater can lead to an estimated $27,000 in combined damages to an average one-storey home (Kharazi & Behzadan, 2021; Federal Emergency Management Agency, 2021). On a larger scale, floods have resulted in extensive financial losses, with the U.S. reaching estimations per event of $4.5 billion from 2021-2023 and total cost estimate of $196.6 billion from 1980-2023 (NOAA National Centers for Environmental Information [NCEI], 2024). In Canada, insured losses from floods have exceeded $30 million per event, with an estimated $5.5 billion in losses recorded between 2012 and 2021 (Insurance Bureau of Canada, n.d.; Catastrophe Indices and Quantification Inc., n.d.). These losses not only disrupt communities but also have significant implications for the economy.

Deeper floods pose a greater risk of causing damage and endangering lives. Estimating flood depth enables prediction, mitigation, and planning for the impacts of flooding on both human communities and natural ecosystems (U.S. Geological Survey, National Severe Storms Laboratory, World Meteorological Organization, n.d.). It aids emergency responders and infrastructure planners in executing evacuation procedures and designing resilient infrastructure. Moreover, it assists environmental and climate specialists in assessing the environmental impacts and researching trends related to climate change. Insurance companies also rely on flood depth damage estimation for evaluating the risk and potential costs to human life, infrastructure, and property.

Flood depth serves as a key variable in estimating flood damage and is essential for calculating insurance premium enable insurance companies to accurately assess damages and estimate claims. Various methodologies can be used to determine flood depth, encompassing direct measurements, remote sensing, hydrological or hydraulic modelling, empirical relationships derived from historical data, and crowdsourcing initiatives. Common methods for measuring floods include unit hydrograph, stochastic and statistical, Rational, MacMath, Kirpich, Mockus, SCS, and Snyder methods (Necati, 2016). Remote sensing techniques, GIS techniques, modelling and simulation, machine learning methods, and mathematical and statistical approaches are also employed for flood depth estimation (Daniel et al., 2021). Algorithms have also been developed to map floods using SAR data, and different digital elevation models (DEMs) have been used for estimating flood depth (Cian et al., 2018). Unmanned Aerial Vehicles (UAVs) combined with high-resolution multispectral imagery have been used to map flood inundation and depth in near-real time (Wienhold et al., 2023). These diverse methods serve to estimate flood or flood depth, yet each may present its own limitations and yield different results for the same location; hence, the selection of the appropriate method is crucial for obtaining accurate results.

In the realm of remote sensing, traditional techniques for estimating flood depth rely on Digital Elevation Models (DEMs) to create a Water Surface Layer (WSL), representing the elevation of the flood surface. Additionally, DEMs play a critical role in delineating flow direction and channel networks (Tarboton, 1997), essential for hydrological tools like Height Above the Nearest Drainage (HAND) maps, which serve as proxies for flood risk assessment. While hydrodynamic models commonly rely on DEMs to estimate flood depth, the process can be challenging because of the substantial data requirements. Simpler and faster tools such as the Rolling HAND Inundation Corrected Depth Estimator RICorDE by Bryant et al. (2022) and Floodwater Depth Estimation Tool FwDET by Cohen et al. (2019) require a smaller amount of data to simulate flood depths and have been tested on riverine, coastal, and pluvial floods.

In the context of flood vulnerability, flood insurance emerges as a crucial instrument for safeguarding communities located in flood-prone regions. It offers financial protection determined by a price signal that aligns with the actual flood risk, encouraging risk-averse behaviour in these communities. Price signals are related to economic estimation of flood damage is facilitated through the development of depth-damage functions. Pistrika et al. (2014) presents a methodology for creating these functions, calculating damage based on structural and material impacts. Damage functions, contingent on building types, are used to construct depth damage curves (McGrath et al., 2019; FEMA, 2020; Scawthorn et al., 2006). Accurate quantification of impacts and damages is essential for insurance coverage and flood risk assessment, where flood depth assumes a significant role. Additionally, as emphasized by Cian et al. (2018), flood depth data plays a crucial role in emergency response efforts. This data assists in determining accessibility to affected areas, devising effective intervention strategies, calculating water volumes, allocating resources for water pumping, and swiftly estimating intervention and reconstruction costs.

1.1. Flood vulnerability in northern regions

When it comes to flood risk management, it is crucial to monitor spatial and temporal variations in river and floodplain water depth. However, temporal and spatial variability are significant sources of uncertainty (Azizat, 2018). This is especially pertinent in northern regions characterized by severe winters and the influence of river ice on hydraulic dynamics, including the occurrence of ice jams (Madaeni et al., 2020). Such observations play a pivotal role in operational hydrology, facilitating timely and informed decision-making processes.

In comparison to riverine and pluvial floods, ice jam floods are common in northern regions and their complex nature presents unique challenges. Das and Lindenschmidt (2020) state that ice jam floods can be more destructive than open-water flooding, resulting in infrastructure destruction, property damage, and fatalities. Some high-latitude northern regions are becoming more vulnerable due to climate change, which is altering river ice regimes and influencing the severity of ice-jam flooding in frigid locations (Das & Lindenschmidt, 2021). Significant property and infrastructure impacts can result from river ice-jam flooding in those locations (Lindenschmidt, 2024). Therefore, it is essential to comprehend and measure the flood risk in these areas to lower hazards and boost resilience (Rokaya, 2018).

1.1.1. Ice Jam floods

In regions prone to harsh winters, the formation and accumulation of ice triggers ice breakup events that significantly impede river flow and often result in flooding. Ice jam floods are a natural consequence of the winter ice cover regime, arising from intricate interactions between dynamic hydraulic, thermodynamic, and structural processes (Wang et al., 2024). The study of the complex phenomenon of ice jams has gained attention over the last decades, particularly due to the inherent unpredictability and irregularity of natural streams (Beltaos 2008, Lindenschmidt et al. 2018, Pawłowski 2019).

Ice jams can take on various forms, with some lasting a few hours while others persist for several days. Breakup jams are known for their sudden releases, which can lead to hazardous events and substantial physical disruptions, posing a threat to the civil infrastructure and the environment. To underscore the significance of ice jam floods, a previous study by French (2018) reported an annual cost of approximately $300 million US attributed to river ice jams in North America. This underscores the economic and environmental impacts of ice jams and highlights the importance of understanding and managing this phenomenon to mitigate its effects.

Accurately forecasting the potential damage caused by ice jam events is crucial for planners and emergency responders. Predicting the impacts of ice jams involves considering various dynamic interactions between thermodynamic components, such as temperature changes, the formation of ice jams, and the buildup of ice under ice dams. These interactions can be complex and challenging to model accurately due to the unpredictable nature of ice movement and jam formation. Therefore, forecasting the potential damage caused by ice jam events requires advanced modelling techniques and a comprehensive understanding of the factors influencing ice jam dynamics. Further, ice jams have dynamic effects that impact both upstream and downstream flow conditions in rivers or streams. Upstream, the obstruction caused by the jam disrupts the natural flow of the river, leading to a rise in water levels. Additionally, the backwater effect amplifies this rise, extending the inundation further upstream. Downstream, flow rates decrease as the jam blocks the passage of water.

However, when the ice jam breaks, it can unleash a release wave, posing flood risks to areas downstream.

Hicks (2016) expands on the dynamic complexities of downstream release waves. She explains that the rapid breaking or fragmentation of river ice in spring or early summer generates downstream water waves and ice runs. Moreover, the influential factors that influence the relative speeds of ice and water during an ice jam release, such as geomorphological features, can decelerate ice runs, leading to a water wave advancing ahead of the ice run. Nafziger et al. (2016) expand on the effect of ice jam breaks under water waves, specifically the complicated dynamics encountered in ice jams and how they complicate the ability to assess the speed and form of water waves as well as the velocity and size of ice runs when the ice jam releases. Furthermore, accumulated ice under ice runs can interact with pre-existing ice jams, potentially augmenting their volume and momentum, thereby contributing to flooding. Assessing downstream release water waves is important because the quantity and height of water carried by the downstream wave itself can lead to water overtopping additional ice dams, and the magnitude of these waves will affect the flood risk for downstream areas.

Presently, there is a scarcity of ice jam flood data, as evidenced by the development of novel modelling approaches and frameworks to address this data scarcity issue (Lindenschmidt et al., 2019; De Coste et al., 2021). Additionally, challenges in modelling ice jam floods are often attributed to the lack of comprehensive data (Beltaos, 2010; Beltaos, 2021). Consequently, most models remain unable to incorporate many of the complex dynamics encountered in ice jam flood events.

1.2. Flood depth maps

In ice jam flooded areas upstream of the jam, it is important to determine floodwater depth since it serves as an indicator of flood damage. One method for assessing flood depth and damage uses flood maps, which are available online, sourced from various institutions and databases, and play a crucial role in flood management and disaster response. However, these maps often have limitations, including specificity to certain regions and lacking information on water depth. An alternative, hydraulic models, can simulate water depths with accuracy, but are time-consuming to prepare and require extensive data compilation and calibration, making them less practical for real-time or event-specific applications. An immediate response in estimating flood damage requires flood depth determination. Such information is also important for preventive measures and facilitating post-event recovery efforts. Therefore, the ability to rapidly produce flood depth estimations is important for regions susceptible to frequent flooding. Additionally, in regions lacking sufficient data for complex modelling, the availability of low-input flood depth estimations is essential. They enable authorities to make informed decisions and allocate resources effectively to mitigate the impacts of flooding and enhance resilience in vulnerable areas.

Swiftly estimating flood depth can be achieved through observations, including those from social media and stop signs along flooded roads (Fohringer et al., 2015; Kharazi and Behzadan, 2021). Methods such as DEM-based inundation depth derivation (Cian et al., 2018) and tools like RICorDE (Bryant et al., 2022) and FwDET (Cohen et al., 2019) use DEMs and water extent to provide rapid flood depth information. This depth information is crucial for assessing potential damage to buildings, determining road closures, and aiding authorities in prioritizing mitigation efforts.

To convert damage into economic insights, knowledge of the pre-disaster market value and replacement cost of affected structures is crucial (Chang et al., 2023). Governments, organizations, or agencies provide material or financial assistance based on these estimates (Ballocci et al., 2023). However, the generation and effectiveness of damage curves are limited by the scarcity of flood depth data, monitoring limitations, and the region-specific nature of damage functions (Endendijk et al., 2023; Martello et al., 2023; Sulong & Romali, 2022).

1.3. Objectives

The main aim of this thesis is to assess and study gridded flood depths for the 2020 Fort McMurray ice jam flood event generated with fast response flood depth estimation tools. Based on Geographic Information System (GIS) and requiring a DEM, flood extent map, and a map of permanent waterbodies, these tools include a Natural Resources Canada model called RICorDE v1.0.1. The specific objectives are to,

1. Assess the performance of the rapid flood depth estimation tools RICorDE under an ice jam flood event by comparing their gridded depths against FwDET and known values of the 2020 Fort McMurray flood.
2. Assess the accuracy of the Height Above Nearest Drainage (HAND) model for generating flooded extent and depth maps.
3. Assess Whitebox Tools (WBT) hydro-correction methods for Digital Elevation Maps towards stream hydro-connection by studying the effect of depressions on flow accumulation.

The outlined objectives aim to comprehend and assess the effectiveness of RICorDE methodologies relative to the latest version of FwDET, with the objective of improving RICorDE performance in handling the Fort McMurray 2020 ice jam event in future iterations of the algorithm.

The evaluation of RICorDE scrutinizes its hydro-correction and HAND methodologies. Various depression-fixing algorithms are also investigated to address water-land boundary hydro-connections and assessed their impact on hydrological tools reliant on accurate flow direction. This was imperative as these algorithms are integrated into the RICorDE v1.0.1 algorithm and its computations related to the HAND model. In RICorDE, steps 1 and 2 are important inputs to step 3, the results of the flood depth estimation tools themselves. On the other hand, FwDET implements a lesser number of processes to its algorithm resulting in a less complex methodology. Main highlight from FwDET v2.1 is its implementation of a slope filter and its efficiency in removing outliers prior the generation of flooded depths. In FwDET steps 1 and 2 are not directly related to step 3. However, to evaluate the performance of FwDET under a HAND map an algorithm run was made following the two HAND methodologies explored in objective 2. Finally, the derived flood depths from the fast response tools are compared with a calibrated HEC-RAS hydraulic model and surveyed HWM of the flood event to evaluate their performance against known values.

1.4. Thesis overview

The thesis commences with Chapter 2, which provides a literature review that covers topics such as depressions, flow direction, flood mapping methodologies, HAND maps, flood depth estimation techniques, and the hydraulic properties of river ice. Following this, Chapter 3 describes the case study area, its geographical location, the collected data, and preliminary data processing procedures. Chapter 4 presents the methods followed to achieve the objectives results and the approaches followed towards the outcomes presented. Chapter 5 presents the study results, covering the validation points and performance reports for the algorithms investigated as well as discussion material. Finally, Chapter 6 presents the conclusions and potential future research directions.

2. Literature review

Without adaptation, the impacts of global warming are projected to exacerbate direct flood damages significantly. It is estimated that with a temperature increase of 1.5°C to 2°C beyond pre-industrial levels by 2040, direct flood damages could double, while at 3°C, they could increase by 2.5 to 3.9 times (Intergovernmental Panel on Climate Change, 2022). This escalation in flood risks is attributed to anticipated climate hazards such as sea level rise, storm surges, and intensified rainfall patterns. Given floods adverse impacts on trade, population, and aquatic life, it is imperative to mitigate and predict flood risks and damages effectively.

Flood depth can be utilized to estimate economic damage to buildings by quantifying the relationship between flood depth and the damage caused by floodwaters. There are plentiful approaches to estimate flood depth. The more complex ones require numerous data to model hydraulic flow, while the simpler methods require flood extent and terrain data alone. A complex approach is often time consuming and is restricted by the availability of hydraulic data. Simpler approaches are also limited by data availability; however, DEMs are widely available on online databases and flood extent may be generated from visual or surveyed data.

While flood depth maps may be generated manually, algorithms that automatically develop these maps have been presented in the literature. Height Above Nearest Drainage (HAND) maps commonly used as an inundation proxy to estimate extent or depth is crucial for fast response flood risk analysis and is often coupled with flood depth estimation algorithms. HAND algorithms necessitate continuous downslope flow from each DEM elevation point toward the water boundary to depict elevation. This delineation process relies on the use of flow direction algorithms. Among various approaches for determining flow direction, the most utilized method is D8 flow, which directs flow towards the lowest elevation point among the eight neighboring points. In addition to HAND maps, flow direction algorithms are utilized in hydrological and hydraulic modelling to determine the path or direction of water flow across a terrain surface.

When using flow direction algorithms, DEM depressions may obstruct flow. Obstructed flow hinders the performance of flow direction dependant algorithms. To solve the problematic caused by depressions encountered in DEMs, depression fixing algorithms are used, of which there are many as well as plenty of literature on their performance and methods. Overall, this section looks to have a deeper look into the literature as well as the distinct fast response flood depth methodologies and their subprocesses. We will also discuss ice jams and how they affect water flow.

2.1. DEM depressions

A depression is a point or region that is lower than all other nearby points. Each depression has a distinct catchment area. The exit of a depression is the lowest point along the depression catchment border, while the "inner area" of the depression is the portion of the depression that is lower than the outlet point (Figure 1). Depressions can and have been referred to by several names. Lindsay (2016) presents a typology to help clear up this confusion, found in Figure 2.

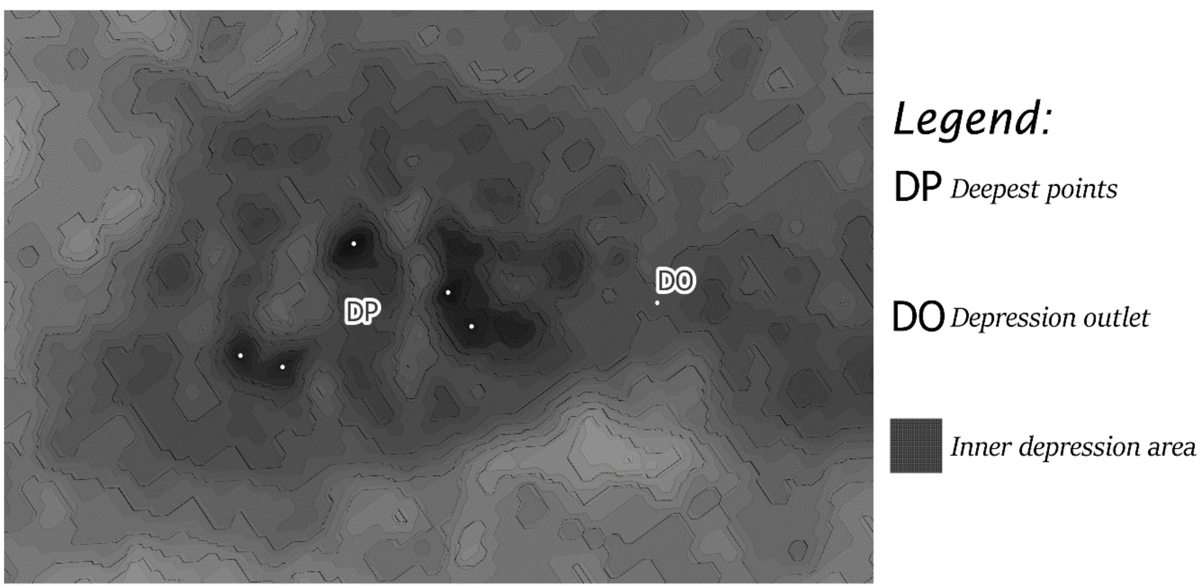

Figure 1. Display of a depression inner area, outlet, and catchment. Reproduced from Band (1986).

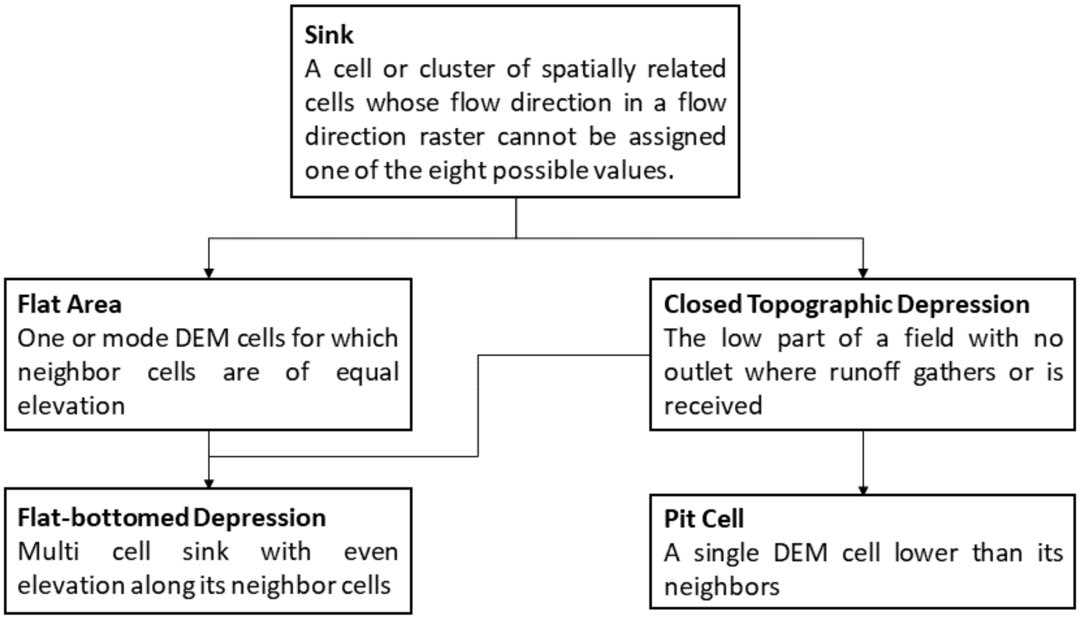

Figure 2. Typology of features found in DEMs that interrupt modelled flow paths and require flow enforcement. Reproduced from Lindsay (2016).

DEMs exhibit depressions when portions of the grid cells have a lower elevation than the cells around them. The existence of surface depressions in DEMs prohibits simulated water flow from draining to outlets, resulting in disconnected stream-flow patterns and false internal sub-watersheds flowing into these depressions. Therefore, surface depression detection and elimination is a vital step in the automated modelling of surface runoff based on DEMs. The standard procedure is to find and eliminate surface depressions in the DEM during the first phase of hydrologic analysis. This must be addressed before topographic attributes and terrain features linked to flow directions can be derived from DEMs in a hydrologically correct way.

DEM depressions can be natural terrain features or fictitious depressions. False depressions reveal flaws in DEMs and can be caused by input data mistakes, interpolation flaws during DEM creation, truncation or rounding of interpolated values, or averaging of grid cells elevation values (Lindsay and Creed, 2006). They are predominant in landscapes with high variations or irregularities in terrain elevation because of the reduced vertical precision of the DEMs in this sort of location (scattering effect). However, natural depressions are normally rare or absent in most terrain types and are far less common than spurious depressions (Wang, Qin, & Zhu, 2019).

2.2. Determining flow direction in DEMs

Flow directions in DEMs is typically assigned based on grid-cell elevations and the path of steepest descent. Flow directions are an essential component for modelling near-surface flow dynamics, aiding the representation of water flows throughout the landscape.

The variety of flow direction delineation methodologies is presented in Table 1. The D4 algorithm directs flow from a focal cell to one of its four surrounding cells to the north, south, east, or west. The D8 method employs the clockwise indexing method in its flow delineation algorithm. The D∞ or D-INF method allows for flow divergence, where flow can be directed to one or more neighboring cells, defining flow direction as an angle in radians toward the steepest downward slope (Tarboton, 1997). Additionally, the Multiple Flow Direction (MFD) algorithm proportionally distributes flow to all downstream neighbors, with steeper neighbors receiving a greater proportion of flow compared to others (Qin et al., 2007).

Table 1. Primary flow direction algorithms.

Flow direction algorithms	Diagram	Description
D4	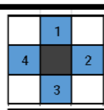	One direction in a straight line, either horizontally or vertically
D8	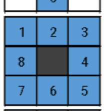	One of its eight adjacent or diagonal neighbors with the steepest downward slope.
DINF	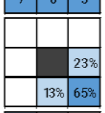	Encoded as a continuous (floating point) quantity between 0 and 2π encoded as an angle in radians, counter-clockwise from east.
MFD	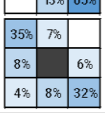	According to the height gradient between the adjoining cells, partitions flow from each cell to as many as eight of its neighbors.

D8 flow direction for a cell (i, j) can be represented as:

$$D8_{ij} = argmax(Slope_{ij})$$

Where:

- $D8_{ij}$ is the flow direction of the cell (i, j)
- $Slope_{ij}$ is the slope of the terrain at cell (i, j).
- $argmax$ returns the direction with the maximum slope.

The D∞ or D-INF flow direction algorithm can be expressed as follows:

$$\theta = \operatorname{atan}\left(\frac{dz}{dx}, \frac{dz}{dy}\right)$$

Where:

- θ is the flow direction angle, measured in degrees clockwise from the north.
- dz/dx is the rate of change of elevation in the x-direction (east-west).
- dz/dy is the rate of change of elevation in the y-direction (north-south).

Problems related to the presence of excessive surface roughness and depressions in terrain surfaces can pose challenges to flow direction modelling. The challenge arises in the context of cells inside closed depressions where flow directions tend to be erroneous (Wang et al., 2019). Closed depressions are elevation points without a lower point in the slope. Closed depressions have been a longstanding issue in the context of flow direction computations, creating situations where flow is directed towards such locations and is unable to 'escape', leading to computational challenges.

Addressing the complexities of flow directions in depressions derived from unrevised DEMs requires careful consideration of various strategies and information to ensure the accuracy of hydrological modelling and related analyses. For this reason, hydrologically correcting DEMs is a critical step when working with flow direction reliant algorithms. Raising depression elevations to the minimum value required to permit continuous drainage flow from that cell to an outlet. Research by Tarboton et al. (1991) indicates that topographical depressions in DEMs affect approximately 0.9-4.7% of 30-meter grid cell DEM. Hydro-conditioning depressions requires altering DEM elevations by establishing flow directions and drainage structures in alignment with downslope slopes. The outcomes of hydro-correction algorithms are affected by the chosen DEM resolution and correction method. Studies have proposed an optimal resolution range of 5-30 meters for hydrological applications (Yuan et al., 2023; Topp, 2014). Several depression-processing algorithms have been developed, each utilizing various tactics and considering different information to establish proper flow patterns in depressions. Hydro-correction algorithms primarily differ in how they modify elevations to eliminate depressions, and are typically categorized into three techniques: smoothing, filling, and breaching. Figure 3 provides a visual representation of the three. In terms of flow direction, several processing algorithms have been developed to identify flow directions in depressions without necessitating extensive DEM revisions. Correcting depressions and flat areas are complex tasks because of the multitude of possible flow directions in the two-dimensional space. Hydro-correction algorithms often aim to determine the optimal path, known as the lowest spill elevation path or least-cost path. This path minimizes the cost for surface water to fill up depressions, resulting in changes to flow patterns, especially when simulating hydrographs.

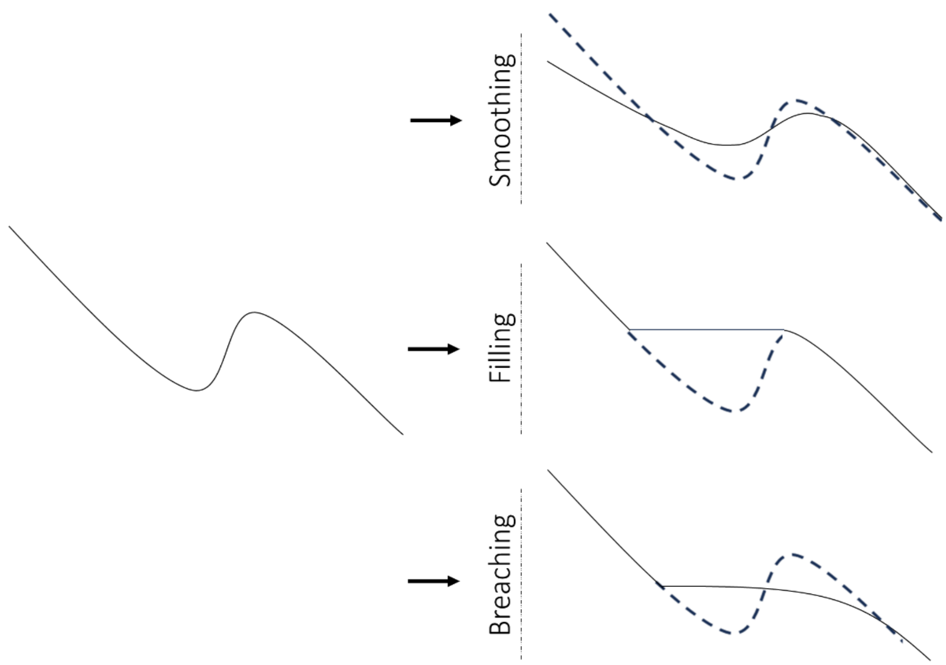

Figure 3. Schematic diagram of the depression-processing algorithms with the DEM-revising strategy. Reproduced from Wang et al., (2019). a) Smoothing filter. b) Depression Filling. c) Depression Breaching.

The performance of flow direction algorithms has been widely investigated. The choice of flow direction method in hydrological and inundation studies influences the accuracy of results. For example, when employing single-flow direction (SFD) algorithms for flow routing in DEMs, Fairfield and Leymarie (1991) and Bogaart et al. (2006) mentioned that limitations often manifest themselves as inaccurate flow lines and an inability to generate distinct flow paths. Multiple flow direction algorithms such as D∞ and the Multiple Flow Direction (MFD) address some of these issues. However, these also encounter challenges, particularly concerning the criteria used to partition flow into multiple downslope pixels. In another study, Zheng et al. (2018) evaluated the performance of D8 and D∞ flow direction algorithms with the generation of HAND datasets. Their study revealed that the D∞ approach showed preferable outcomes because of its ability to smooth HAND values, effectively averaging sharp differences between neighboring grid cells observed in the D8 approach. When analyzing flood inundation and channel hydraulic parameters using HAND data, the D∞ technique proved more suitable for simulating lateral water expansion across the landscape.

Unconventional techniques to delineate flow direction in DEMs are also presented in the literature. Contour path-tracing algorithms present alternative means to establish flow directions, potentially presenting a remedy to grid-based flow routing issues (Moore et al., 1988; Menduni and Riboni, 2000; Mizukoshi and Aniya, 2002). Yet, contour path-tracing algorithms introduce their own challenges, including oversampling elevation data at specific contour levels and a lack of elevation estimates between these levels, which may limit their ability to account for slope information (Wise, 2000). Moreover, contour-based methods could lead to data gaps due to oversampling certain contour heights (Wu et al., 2009). These diverse approaches, each with distinct strengths and limitations, offer important choices for terrain analysis and hydrological modelling. Practitioners must select the most suitable method based on the specific requirements and characteristics of their study area.

The original methods in handling depressions were proposed by Marks et al. (1989) and O'Callaghan and Mark (1984). The general approach in addressing surface depressions is to treat depressions as individual ponds or reservoirs, simulating how they would flood. The smoothing filter, the simplest of the three approaches, leads to significant information loss in non-problematic DEM sections when applied indiscriminately across the entire terrain (Pathak et al., 2015). The loss of terrain features negatively affects the representation of topographic features, particularly drainage features like headwater streams, prompting the need for corrective measures in hydrological analyses.

The depression filling algorithms typically elevate cells within a depression area to align with the value of the lowest cell on the depression outer boundary if it holds a higher elevation value, the elevation of the depression cells permits a continuous flow along the depression. Various methodologies to determine and fill the lowest value within a depression are available. A common approach involves simulating floodwater to identify the specific level at which overflow begins from an outlet, aiming to establish a monotonically decreasing route of cells leading to the dataset edge. Some of the well-known algorithms that detect and fill surface depressions include those by Jenson and Domingue (1988), Planchon and Darboux (2001), and Wang and Liu (2006).

Planchon and Darboux (2001) filling method is based on 8-connected grids and comprises two stages: locating local minima and filling them from bottom to top by investigating nearby areas to find outlets. Executed iteratively, this algorithm effectively handles embedded depressions by iteratively flooding the surface to gradually explore the terrain from eight alternating directions, draining excess water from each cell to its downslope paths. Ultimately, it removes water in depressions to the level of the highest pour point on the flow channel to an outlet, leaving flat depression surfaces.

Wang and Liu (2006) introduced the concept of “spill elevation” and progressive construction of optimal spill paths through priority queue and least-cost search techniques. Spill elevation represents the minimum elevation a cell requires to spill water to an outlet of the DEM border, ensuring the lowest possible elevation for interior cells by linking them to the lowest outlet. The method identifies outlets on the DEM border, constructs flow paths, iterates optimal flow paths and spill elevations, fills spotted depth grid cell values, and partitions watersheds. The Wang and Liu (2006) method exhibits a lower number of steps than Planchon and Darboux (2001), resulting in an improved computational efficiency.

Depression breaching is an alternative to depression filling and reduces the impact on the topographical landscape. As outlined by Rieger (1998), this technique lowers grid cell elevations along a narrow breach channel, linking the bottom of a confined depression to a downhill point. Progressively reducing elevations along that path until reaching the nearest neighboring cell lower than the depression bottom elevation. Compared to previous methodologies, depression breaching significantly reduces the impact on the topography and flow paths when contrasted with depression filling techniques (Soille, 2004b; Lindsay and Creed, 2005; Lindsay and Dhun, 2015).

Different alternatives have been developed for choosing the remote grid cell in a pit for breaching algorithms (Lindsay and Dhun 2015 on: Lindsay and Creed 2005, Soille et al. 2003 and Soille 2004a, and Schwanghart et al. 2013). Schwanghart et al. (2013) proposed a breaching method that selects breach paths following a least-cost optimization. Lindsay (2016) introduced a selective breaching method, offering users the option to either breach or fill the DEM. It involves four steps: assigning cell elevation and identifying pit cells, raising cells slightly below the elevation of their lowest neighboring cell, priority flood-based depression breaching, and a subsequent filling following the established flood order.

The breaching approach has difficulty with deep depressions. To address these problems, Lindsay and Dhun (2015) presented an approach that implements both breaching and filling approaches in a single algorithm. Breaching results in lower alterations, while filling addresses the depressions that have no breaching solution. Implementing breaching before a filling phase reduces the overall impact on the elevation dataset compared to exclusively following a filling approach. For example, Lindsay and Dhun (2015) showed that the depression breaching method modified elevations of 86.5% fewer grid cells than its counterpart solution. This reduced alteration in elevations and enhanced the depiction of surface hydrological flow routes in the DEM without requiring additional information like drainage ditch and stream vectors, particularly when the DEM exhibited greater resolution than the available drainage information. Finally, drainage enforcement, an alternative breaching method, faces hurdles due to the absence of embarkment underpasses in LiDAR DEMs, leading to potentially erroneous data (Barber and Shortridge, 2005).

To compare filling, breaching, and hybrid techniques, Soille (2003) and Lindsay and Creed (2005) evaluated the most suitable scenarios for employing each method. Their concluded that hybrid strategies slightly outperformed a breach-only approach and had the least influence on simulated flow pathways. Lindsay (2016) suggested that in isolated pits, a single cell filling method delivered superior outcomes compared to its breaching counterpart; however, single filling approaches are typically combined with other filling techniques. In summary, many alternative approaches exist, with the ones considered in this study listed in Table 2.

Table 2. Hydro-correcting algorithms considered.

Hydrological Correction tools	Fill Type	Flow direction algorithm	Implementation	Reference
BreachDepressions	Depression Breaching, Depression filling	D8	WBT	Lindsay, J. B. (2016)
BreachDepressionsLeastCost	Depression Breaching, Depression filling	D8	WBT	Lindsay and Dhun (2015)
RichDEM: Depression-Breaching	Depression Breaching	D4, D8	RichDEM	Barnes (2018)
RichDEM:Depression-Filling	Depression filling	D4, D8	RichDEM	Barnes (2018)
Pit Remove	Depression filling	D8, D-INF	TauDEM	USU Watershed Sciences, n.d.
FillDepressions	Depression filling	D8	WBT	Whitebox Geospatial Analysis Tools, n.d.
FillDepressionsPlanchonAndDarboux	Depression filling	D8	WBT	Planchon and Darboux (2002)
FillDepressionsWangAndLiu	Depression filling	D8	WBT	Wang and Liu (2006)
FillSingleCellPits	Depression filling	D8	WBT	Whitebox Geospatial Analysis Tools, n.d.

2.3. Synthetic Aperture Radar (SAR) based flood extent mapping

Flood extent maps derived from remote sensing data can provide valuable calibration and validation data for hydraulic models of river flow processes (Schumann et al., 2009). Flood maps serve multiple purposes, including aiding in emergency flood relief management, developing precise hazard maps, and facilitating risk assessment and emergency preparedness and response. They play a crucial role in assisting urban planners and engineers in designing resilient infrastructure and formulating growth plans (Federal Emergency Management Agency, 2024).

Remote sensing images can be used to identify land-water boundaries and determine water elevation along a shoreline, as high resolution DEMs and earth observation data become more widely available globally. Many methodologies to generate flood extent maps from remote sensing are found in the literature. For example, Cian et al. (2018) utilized sequences of satellite Earth Observation (EO) imagery combined with topographical data to estimate temporal and geographical fluctuations in water elevations at the land-water interface. Giordan et al. (2018) presented a threshold approach that looks for a backscattering value below which a pixel is identified as water. Matgen et al. (2016) used a HAND model to normalize the topography of a drainage network to generate flood extent and depth maps. Their approach started by mapping the water surface from the SAR dataset, which were used to generate depth maps in respect to drainage. Cian et al. (2018) presents a variety of flood depth estimation algorithms by means of high-resolution LiDAR and SAR images. The paper offers a thorough analysis of the use of cutting-edge technologies in flood depth estimation. In addition, Cian et al. (2018) presents a novel method for precisely detecting flood depth by combining image processing and manual retrieval.

When generating flood extent maps with SAR, limitations can be encountered within urban and vegetated areas, since multiple factors combine to define the backscattering signal in these conditions. Moisture, for example, has a substantial influence in bare soil, increasing the backscattering value compared to dry conditions, whereas flooded vegetation causes a double-bounce effect, making it appear brighter in a SAR image (Amitrano et al., 2021). Gaps may exist in urban areas, such as shaded areas or intricate urban structures, where SAR backscattering may not indicate the presence of water (Amitrano et al., 2021). These are often related to the backscattering effect caused by the complicated geometry and diversity of materials encountered (Tretyak et al., 2021). To name a few, building dihedral and trihedral reflection, the presence of metal surfaces which heighten the backscatter effect. However, backscattering limitations are a common issue across all SAR applications.

2.4. Height Above Nearest Drainage maps for flood risk assessment

Height Above Nearest Drainage (HAND) maps, first introduced by Rennó et al. (2008), are a simplified model for rapid flood inundation mapping. HAND algorithms use stream networks to assess elevations, relying on local drainage patterns and flow accumulation methods to level out terrain, helping locate high and low points. The equation to calculate the vertical distance between each cell in a DEM and the nearest drainage of HAND map can be expressed as follows:

$$HAND = DEM - (DN + HAND_0)$$

Where

- $HAND$ is the Height Above Nearest Drainage value for a particular cell.
- DEM is the elevation value of the cell in the DEM.
- DN is the elevation value of the nearest point on the drainage network.
- $HAND_0$ is an offset value added to the HAND to account for factors such as vegetation height or streambed depth.

DEMs should undergo hydro-correction before generating HAND maps to ensure a continuous downslope towards drainage for every grid elevation. Hydro-correction of DEM values enable the HAND algorithm to accurately depict the necessary elevation points for each cell via flow direction algorithms. Failure to connect cells to the water-land boundary can result in gaps within the HAND map, leading to inaccuracies in HAND values. For instance, in Figure 4, we observe a non-filled HAND map exhibiting such gaps, which compromises the accuracy of the HAND values and the overall map integrity. Additionally, to increase the validity of the HAND map, it is advisable to incorporate the elevation difference introduced to the original case study DEM. For example, subtracting the filled DEM difference in elevation ensures that the HAND maps accurately reflect the true elevation values of the terrain, especially in areas where the DEM has been modified to achieve hydrological consistency. This difference is calculated using the equation:

$$HAND_0 = HAND - \ (Fill - DEM)$$

Where:

- $HAND_0$ is the offset of the HAND map, representing the difference in the filled DEM.
- $HAND$ is the HAND map achieved from the previous equation.
- $Fill$ is the hydro-corrected DEM used to generate the HAND map.
- DEM is the elevation value of the cell in the DEM.

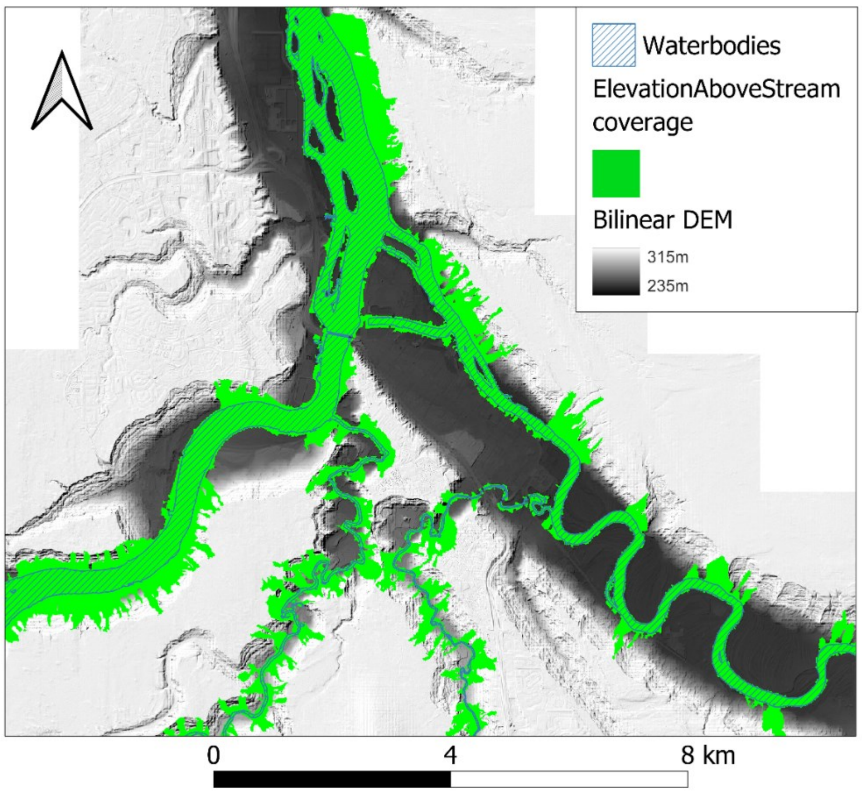

Figure 4. In this figure we can see how failing to hydro-correct the DEM causes cells to not be accurately depicted in the HAND algorithm. The green extent presents the problematic HAND cells that are hydro-connected to the water-land boundary.

HAND maps have been extended to cover worldwide regions with 30-meter resolutions (Donchyts et al., 2016; Yamazaki et al., 2019) and can provide the means to derive multiple hydraulic properties of rivers (Zheng et al., 2018). For example, previous studies have used HAND maps to generate flood maps and have been previously integrated in hydrological simulations to simulate flow (Nobre et al., 2011 and Nobre et al., 2016). Overall, HAND maps contribute to mapping flood inundation extent (McGrath et al., 2018), assessing flood risk, and supporting hydrological modelling (Aristizabal et al., 2022). It provides a tool for various hydrological applications that, although unable to explicitly simulate flow dynamics or the physics of flooding, can rapidly estimate potential inundation using topographic relationships with minimal input data. It is noteworthy that different flow direction algorithms may yield varying results. In studies by Tarboton (2016) and Liu et al. (2016), it was found that the choice of flow direction algorithm can impact the accuracy of HAND maps, with the D∞ algorithm outperforming the D8 algorithm.

In conclusion, HAND maps have emerged as a valuable resource with global coverage, capable of derivation of essential hydraulic properties of rivers. These maps have found utility in diverse applications, from generating flood maps to supporting hydrological simulations and assessing flood risk. While HAND maps offer rapid estimations of inundation potential based on topographic relationships, it is noteworthy the potential influence of flow direction algorithms on their accuracy. Thus, while HAND maps provide valuable insights into flood dynamics, careful consideration of underlying algorithms is essential for their reliable application in hydrological modelling and risk assessment.

2.5. Fast response flood depth estimation tools

Rapid response flood depth estimation tools streamline the process compared to traditional flood depth estimation methods by determining flood depth with a DEM and flood extent alone, generating horizontal water levels along the river that are comparable to those derived from 1D hydrodynamic models (Zwenzner and Voigt, 2009, Matgen et al., 2007). Methods have been explored and validated in the past for fast response flood depth estimations, these involve the generation and growing of continuous shoreline values to generate a WSL and inundation raster (Cian et al., 2018; Cohen et al., 2018; Cohen et al., 2019; Bryant et al., 2022; Elkhrachy 2022; Cohen et al., 2022).

The methodology of fast response flood depth estimations shares common elements such as utilizing high-resolution SAR images and lidar data for accurate flood depth estimation as well as the integration of three fundamental hazard grids interconnected through the following equation:

$$Depth = WSE - DEM$$

Where:

- Depth is the water depth in meters
- DEM is the Digital Elevation Model (DEM) ground elevations
- Water Surface Elevation (WSE) is the height of the water

The equation just presented applies for the FwDET methodology. However, the equation may vary since the Rolling HAND Inundation Corrected Depth Estimator (RICorDE) estimates flood depth with a HAND map instead of a DEM (Bryant et al., 2022), while the Floodwater Depth Estimation Tool (FwDET) utilizes a DEM (Cohen et al., 2018). RICorDE incorporates a higher degree of parameter processing into its computations, for which HAND maps, which reclassify the terrain by measuring vertical distance instead of showing absolute elevations, are essential. Integrating a HAND map into RICorDE facilitates calibration based on observed flood data and other hydrological parameters. In the case of RICorDE, which extrapolates edge depth values into an inundation region, the equation would be:

$$Depth = WSE_{HAND} - HAND$$

Where:

- Depth is the water depth in meters
- HAND is the case study HAND map
- WSE_{HAND} is the extrapolated height of the water on the HAND map

The WSL is the top layer of the flood water and is obtained thorough the interpose of the flood boundary datapoints. For this reason, fast response flood depth estimation algorithms are highly dependent on an accurate flood extent. Generally, an accurate flood extent still introduces problems into the generation of an accurate WSL necessitating further processing. For example, a steep terrain along the flood-land boundary can result in the extrapolation of irregular elevation, resulting in unrealistic elevation depth transitions. Flood boundary processing presented on RICorDE and FwDET address discrepancies prior to the WSL generation. RICorDE v1.0.1, for example, statistically processes the flood boundaries with statistical principles such as quartile filtering while FwDET v2.1 eliminates areas where a flood would be unlikely through a slope filter.

Methods used to interpose a WSL from the flood boundary include Euclidean distance, IDW Interpolate and Cost Allocation. Euclidean distance is a measurement of the straight-line distance between two points in Euclidean space, calculated using the Pythagorean theorem. Inverse Distance Weighting (IDW) is a spatial interpolation method utilized to estimate values at unknown locations by considering the values at surrounding known locations. This method assigns weights to neighboring points based on their proximity to the target location. Cost Allocation, on the other hand, is a spatial analysis technique employed to determine the least-cost path or distribute costs across a surface according to predefined criteria. Euclidean distance calculations can be performed using Grow Distance in GRASS, while QGIS provides IDW Interpolate as part of its integrated tools. Euclidean distance was initially integrated within documented versions of FwDET v1 but later migrated to Cost Allocation. Literature by Cohen et al. (2019) suggests that Cost Allocation resulted in the preferred method but was not integrated in the latest FwDET v2.1 QGIS tool for lack of integration in the default QGIS software. RICorDE mentions both Cost Allocation and IDW Interpolate in its algorithm suggesting the incorporation of both within its process.

Cohen et al. (2018) introduce FwDET v1.0 methodology for improved remote sensing analysis of coastal flooding, employed for determining water depth by subtracting the topographic elevation at each grid-cell within the flooded area from the local floodwater height, which is measured above mean sea level (*amsl*). Later, Cohen et al. (2019) introduces FwDET v2.0, presenting the implementation of Cost Allocation algorithms and a runtime efficiency. In Cohen et al. (2022) FwDET v2.1 introduces a slope filter into its methodology. Similarly, RICorDE v1.0.1 estimates flood depth across a flooded domain by incorporating HAND maps and cost distance algorithms to extrapolate flood boundary values into a flood depth inundation raster (Bryant et al., 2022). The workflow of RICorDE can be found outlined in Table 3.

Table 3. RICorDE phases and steps towards depth computations as originally presented in Bryant et al., (2022).

Phase	Steps
First	a) Merge waterbodies with approximate inundation polygons.
	b) Generate points on valid edges
	c) Sample HAND values
	d) HAND inundation from q3 value
	e) Apply max. inundation filter onto flood extent
Second	a) Sample HAND values
	b) Force floor and ceiling
	c) Build interpolated HAND values on the surface
	d) Mask out interior region
	e) Interpolate interior values
	f) Smooth (low-pass filter)
	g) Generate HAND inundation set
	h) Generate WSL set
	i) Mosaic using HAND grid
Third	a) DEM is substracted from WSL mosaic to obtain raw depth raster
	b) Less or equal to 0 depths are removed
	c) Depth raster is clipped to match extent of the hydraulic corrected inundation

There is a substantial amount of documentation evaluating the performance of RICorDE and FwDET under riverine, coastal, and pluvial flood events and little or no documentation on the use of these approaches under ice jam flood events. Ice jam floods pose unique challenges to rapid response strategies, such as the inability to accurately estimate ice volume, and potential limitations in flood delineation from the presence of residual ice along riverbanks, which obstructs the identification of flood boundaries.

RICorDE has been evaluated under the 2018 pluvial flood along the Saint John River at Fredericton and the Rivière des Prairies 2017 flood where it outperformed previous version of FwDET-QGIS achieving an RMSE of 79 and 51 cm for the inundation events (Bryant et al., 2022). During an inland coastal flood event induced by the 2019 tropical cyclone Idai in Mozambique where comparative observational records of sea level rise for the flood event were scarce hindered the precise detection of changes in sea level (Mester et al., 2023). FwDET performance has been reported under the following flood events: the 2017 and 2018 US hurricane season floods, the 2018 floods in the Philippines and Nigeria, and 1988 to 2022 floods in Australia. In the US, FwDET produced an RMSD of 0.38m in the St. Vrain Creek flood in Colorado in 2013, and an RMSD of 0.37m in the Brazos River and San Jacinto River flood in Texas in May 2016 (Cohen et al., 2018). In the Brazos River case study presented in Cohen et al. (2019) FwDET produced a small -0.16m average difference between the model and FwDET v2.0 water depth calculation. In semi-arid regions of Australia, it produced an average underprediction of 0.32m and an inter-quartile range (IQR) of 0.23m–0.39m (Penton et al., 2023).

Cohen et al. (2018) and Cohen et al. (2019) some of the limitations in the methods used for generating a water surface layer and in determining the local floodwater elevation are presented. On the generation of a water surface layer, Euclidean distance was found to incorrectly assign elevations from boundary grid cells across the waterbody due to shorter distances in Euclidean calculations. Additionally, Cost Allocation showed elevation differences compared to hydrodynamic models, with abrupt linear transitions observed in various areas. Fast-response tools also face topographic constraints when estimating flood depth. According to Cohen et al. (2019), underestimations often occur near riverbanks and shores due to boundary cells not representing the complete extent of floodwater. This discrepancy results in the floodwater level appearing lower near the boundary grid than its actual level further inland.

These methodologies highlight the importance of fast and reliable flood depth estimation for economic impact assessment and rapid loss estimation during flood events. They demonstrate the integration of advanced technologies like SAR images and LiDAR data to enhance the accuracy and efficiency of flood depth estimations in various scenarios.

2.6. Influence of river ice on river hydraulic properties

River ice can substantially impact river hydraulic properties, as described in Hicks (2016), key alterations induced by river ice include an increase in the river wetted perimeter and overall channel resistance leading to modifications in the velocity profile that elevate water level. Das and Lindenschmidt (2001) offer valuable insights into river ice relationships and explores various climate impacts on ice-related floods.

Ice-jam flood depth estimations entail intricate analyses and methodologies due to the complexities involved. Ice jams pose significant flood hazards, particularly in areas susceptible to extensive ice formation during winter seasons. The magnitude of ice jam floods is influenced by various factors, including the speed at which release waves propagate, the geometric characteristics of the jam, the condition of the ice, interactions between the ice and water, and the occurrence of temporary jamming followed by subsequent re-release phenomena (Hutchison and Hicks, 2007). Nafziger et al., (2016), along with data cited by Beltaos (2014) and Hutchison and Hicks (2007), offered compelling evidence of the dynamics associated with these events, including wave velocities dynamics. Comprehensive risk assessment necessitates meticulous data gathering and thorough analysis. The monitoring of water level conditions during ice-jam events presents challenges due to the presence of various parameters that extend beyond stream discharge, many of which are inherently unpredictable. A lack of water level data may lead to the utilizing historical data or hydrological models and simulation techniques to estimate water levels in areas where data is lacking. Water level data is important for an effective water resource management. Likely, fast response flood depth estimation tools are valuable for estimating flood depth and can obtain predictions with minimal data (See Chapter 2.5). In contrast, when estimating ice jam floods, river ice characteristics factors such as ice strength, porosity, volume, ice-cover type, ice-jam toe location, and length all play essential roles. River ice characteristics that can be unavailable or hard to measure are relevant during the estimation of river ice water level. For instance, under equivalent discharge conditions, the presence of a thick ice cover and roughness can lead to considerable water level elevations (Das and Lindenschmidt, 2001).

When forecasting ice jam floods, climate characteristics assume a critical role, particularly when considering factors such as river discharge, air temperature, and ice duration. Studies, such as those conducted by Das and Lindenschmidt (2021), Borshch et al. (2001), Rokaya et al. (2019), and Bonsal et al. (2006), demonstrate that the inclusion of climate characteristic variables significantly enhances the accuracy of ice-cover breakup predictions. Additionally, the influence of large-scale atmospheric and oceanic oscillations on ice duration has shown to impact the forecasting of ice-related events.

In summary, river ice profoundly affects hydraulic properties, leading to changes in wetted perimeter and channel resistance, ultimately elevating water levels. Understanding these dynamics is crucial for effective flood risk management. Conventional ice-jam flood depth estimations require detailed analyses due to the complexities involved, necessitating consideration of factors like ice strength, volume, and location. While water level monitoring during ice-jam events presents challenges, it is essential for effective water resource management. Climate characteristics also play a pivotal role in forecasting ice-related floods, with studies emphasizing the importance of variables like river discharge and air temperature. Integrating these factors enhances the accuracy of flood predictions, providing valuable insights for mitigating risks associated with ice-related events.

3. Case study location and description

Fort McMurray is located at the confluence of the Athabasca and Clearwater Rivers. It experiences an annual average precipitation of 391 mm from 1999 to 2023, predominantly falling from May to September (Weatherstats, 2024). Incidents of ice jam formation are particularly prevalent along the Athabasca River. Near the point where the Clearwater River converges with the Athabasca River, ice flows originating upstream often come to a halt. This phenomenon is significantly influenced by the presence of several bars and islands downstream of Fort McMurray (Groeneveld & Zare, 2022).

The topography in the vicinity of the Clearwater River is well-documented in Crown and Twardy (1975). They describe the topography of the Clearwater River as comprising flatlands that exhibit an undulating to smooth terrain, with an elevation of approximately 244 meters above sea level. This elevation is notably 61 to 91 meters lower than the adjacent uplands. Due to the ground surface proximity to the Clearwater River, internal drainage in this area is limited, rendering it susceptible to flooding. South of Fort McMurray, the landscape is described as relatively flat, situated within valleys flanked by steep slopes on at least one side. According to Pierdicca et al. (2018), the Clearwater River is surrounded by terrain formations with heights above 2 meters, described as "*steeply sloping walls*", with DEM slope inclinations of up to 40°. Figure 5 provides aerial imagery of the case study flood event as well as an overview of the project geographical location, and the broader region.

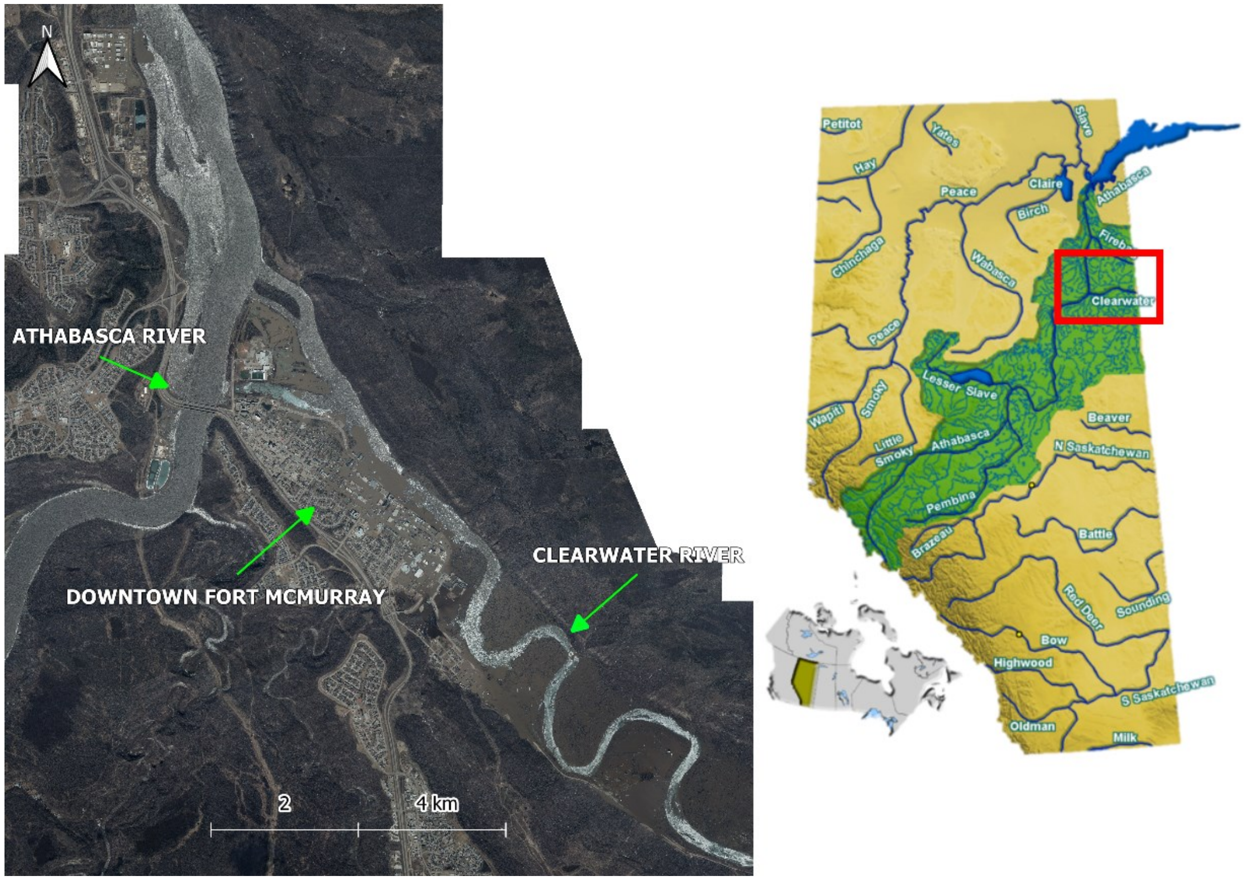

Figure 5. Aerial image of the study area in Fort McMurray, captured on April 28, 2020. This image provides a comprehensive view of the region, emphasizing three geographical features: Athabasca River, Clearwater River, and the Downtown Fort McMurray area. The red box provides a visual approximate of the left panel extent.

Crown and Twardy (1975) characterize the Athabasca River and Fort McMurray town topography as an undulating landscape, featuring cliffs along the river and highly steep irregular slopes. The region also contains segments with interlocking spurs, where long, unidirectional slopes are prevalent. Athabasca River has an elevation of approximately 205 meters above sea level. It is steep and features several rapids and bed discontinuities. Many of these rapids descend only a few meters, until the river transforms from a steep single channel into a wider channel with numerous islands and its slope falls dramatically from 0.00067 to 0.00014 near Fort McMurray (Nafziger et al., 2021).

3.1. Athabasca river

The Athabasca River is documented by Zare et al. (2022) as an uncontrolled river system that spans more than 1200 kilometers, draining a vast expanse of over 154,880 square kilometers of boreal forest and grasslands in the Canadian northwest. The Athabasca River has an average discharge of 783 m^3/s, a maximum discharge of 4,790 m^3/s, and a minimum discharge of 75 m^3/s (Benke and Cushing, 2011). Its annual flows come mostly from spring mountain runoff, and the river flows north. It traverses a region subject to challenging climatic conditions, including short summers and prolonged, frigid winters, making it susceptible to ice jam floods. Ice jams obstruct the outflow of the Clearwater River and cause water levels to rise, resulting in bank overflows. During the 2020 Fort McMurray ice jam flood event the station 07DA001 recorded a minimum flow of roughly 231 m^3/s in March 2020, right before the river ice melted; thereafter, data gaps were encountered for the next three months at the gauge station and discharge data resumed in June 2020 with a flow of 2510 m^3/s.

3.2. Clearwater river

The Clearwater River originates in the boreal forest of northwestern Saskatchewan and joins the Athabasca River in northeastern Alberta, covering 295 kilometers and draining an area of approximately 30,800 km^2. The middle section of the river meanders through the interior plains, while downstream, the lower region has steep valley walls composed of limestone and dolomite. Like the Athabasca River, the Clearwater River annual flow comes mostly from spring mountain runoff driven by increase precipitation and snowmelt. Additionally, the river flows in the northern direction. Floods have been recorded during summer months, attributed to intense rainfall within the drainage basin. Lower flows occur during winter when precipitation accumulates as snow. Station 07CD001 (Clearwater River at Draper) data show that from 2020 to 2022 an average discharge of 159 m^3/s, a peak discharge of 538 m^3/s in June 2020, and a minimum discharge of 55.6 m^{3W}/s in March 2020, right before the river ice melts. Additionally, during spring season the gauge station documents a discharge of 103 m^3/s during April and 308 m^3/s during May.

3.3. Ice Jam flood discharge events at Fort McMurray

Historical records, as documented in Hutchison and Hicks (2007), provide insights into ice jam releases along the Athabasca River, an area extending from Crooked Rapids to the Water Survey of Canada (WSC) gauge located just downstream of Fort McMurray. This annual ice breakup process naturally gives rise to substantial ice jams, especially when these coincide with large-scale breaking fronts spanning hundreds of kilometers, elevating flood risks. The flooding of extensive low-lying areas along the riverbanks is a direct consequence of the presence of these ice jams and ice rushes. Figure 6 shows the three gauges from Fort McMurray, which encountered water level gaps for April 2020 during the ice jam flood. This is a common occurrence since upstream ice jam discharges can result in rapid fluctuations in water levels and the swift transport of water and ice that might disrupt gauge stations.

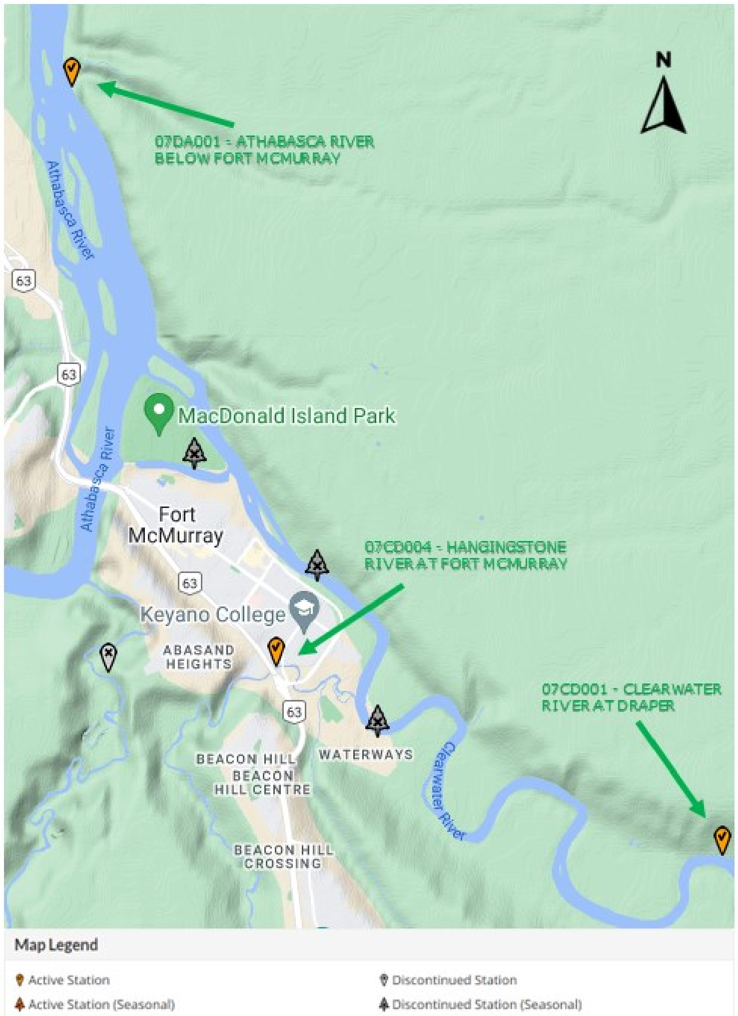

Figure 6. Gauge stations at Fort McMurray with data gaps for the 2020 ice jam flood event. Extracted from the Environment and Climate Change Canada Historical Hydrometric Data web site (https://wateroffice.ec.gc.ca/mainmenu/historical_data_index_e.html) on November 28, 2023.

In 2020, a delayed spring season and substantial snowfall culminated in an explosive river ice breakup along the Athabasca River and Peace River (Nafziger et al., 2021). Observations and monitoring of this event revealed it to be the third-highest flood levels recorded since 1875. Issues related to the uncertainty of water level measurements during the ice breakup process were present due to the malfunctioning and presence of inaccurate data in gauge stations. HWMs were surveyed and available, as shown in Figure 7, depicting some of these reference points along the riverbanks. These HWMs provided data to complement the compromised gauge information, aiding the assessment of the event impact and helping to enhance flood forecasting and post-flood analysis.

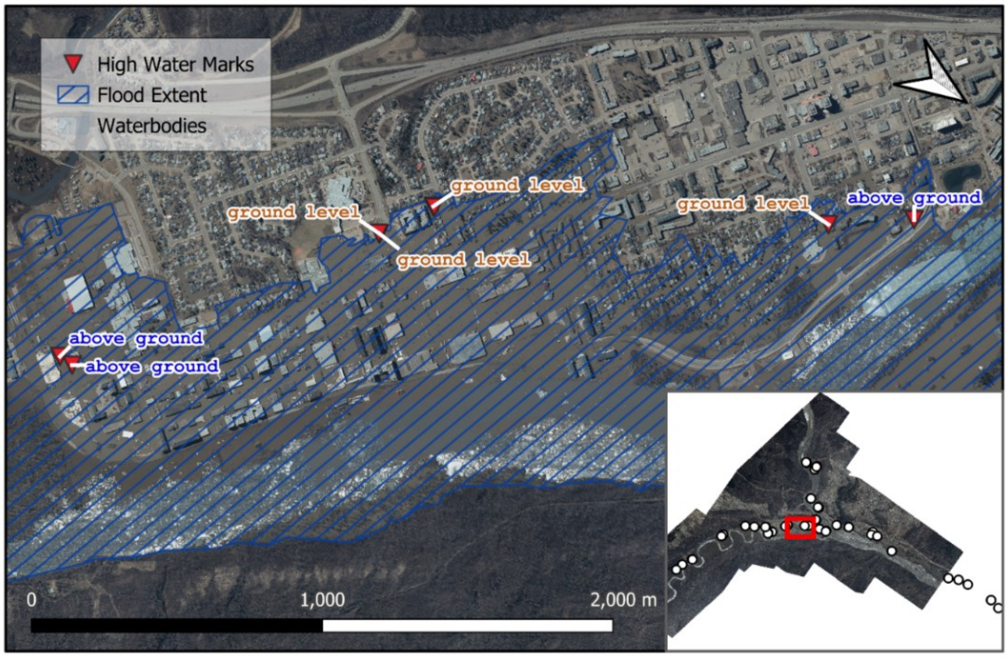

Figure 7. High water marks for the case study marked as "above ground" and "ground level," the high water marks are displayed below an aerial image of the 2020-04-28 ice jam flood event in the Fort McMurray town area. The accompanying minimap provides an overview of the extended area, highlighting the extent and locations of the surveyed high water marks.

Dikes in downtown Fort McMurray were breached, leading to widespread inundation (Figure 8). Total estimated flood damages exceeded $1.1 billion, including $522 million in insured damages and $617 million in uninsured damages, as reported by the Insurance Bureau of Canada (IBC) in 2020 (Adriano, 2021). The disaster resulted in the displacement of 13,000 people between April 26 and May 2, with one fatality reported downstream of Fort McMurray. The impact of this flood is largely attributed to floodwater rather than a combination of ice blocks and floodwater.

Figure 8. These images capture the Fort McMurray flood on April 27, 2020. In the top image, one can see buildings in Fort McMurray town submerged in floodwaters. The second image shows the backwater resulting from the ice jam, which has filled the Clearwater River, spanning from one valley wall to the opposite. Image source: McMurray Aviation (2020).

Hatch and Golder Associates (2021) employed the HEC-RAS model designed for the Fort McMurray Flood Hazard Study to simulate the 2020 ice jam event. Their findings revealed that the case study ice volume in the 2020 ice jam exceeded 28 million cubic meters. Furthermore, the 2020 ice jam elevated water levels in Fort McMurray to levels representing a 1:50 to 1:100 annual exceedance likelihood for ice jam levels.

3.4. Data collected

This section provides an overview of the case study data collected. Data used in this work include DEM, aerial images, waterbodies aerial images and polygons, flood extent aerial images and polygons, a calibrated HEC-RAS model, and collected HWM. Table 4 offers a list of the datasets collected for easy reference.

Table 4. Datasets collected and used in their raw form. The first column shows the dataset name, the second their source, the third their type, and the fourth the capture date. Note: AEP is the same agency as AEPA are the same agency

Dataset	Source	Type	Capture date
DEM	AEP	Raster 0.50m	2016-10-7/13
Aerial image	AEP	Raster 0.15m	2020-04-28
AI Waterbodies	AEP	Polygon	2020
Flood extent	NRCAN	Polygon	2020-04-28
HWM	AEP	.cvs	2020-01-05

3.4.1. Digital Elevation Model

The case study DEM encompasses the Fort McMurray area, including the regions along the Athabasca and Peace Rivers. It was provided by EPA but was collected by Airborne Imaging (2017) between October 7 to October 13, 2016, employing a Leica ALS70 LiDAR system. Documentation of the DEM dataset by Airborne Imaging (2017) suggests it was created with an ArcGIS software using the 3D-Analyst extension and the TerraScan software to generate the raster 50cm grids.

Documentation from Airborne Imaging (2017) lists a vertical accuracy of 15cm in open, flat terrain, which was validated through independent ground truth surveys and aerial imaging assessments. Additionally, the dataset exhibited minor vertical discrepancies, which were expected, particularly in more challenging conditions, such as densely vegetated areas and locations near sharp topographical features.

3.4.2. Waterbodies

Two distinct sets of waterbodies were acquired for this research (Figure 9). The first set was provided under the Open Government Licence – Alberta, from the National Hydro Network (NHN). The second set was provided by H. McGrath and M. Turgeon-Pelchat (pers. Communication, Dec 2022), and was generated through AI-based techniques (NRCAN, 2020). This dataset consisted of water features extracted from optical satellite imagery, including WorldView-2 & 3 and GeoEye-1.

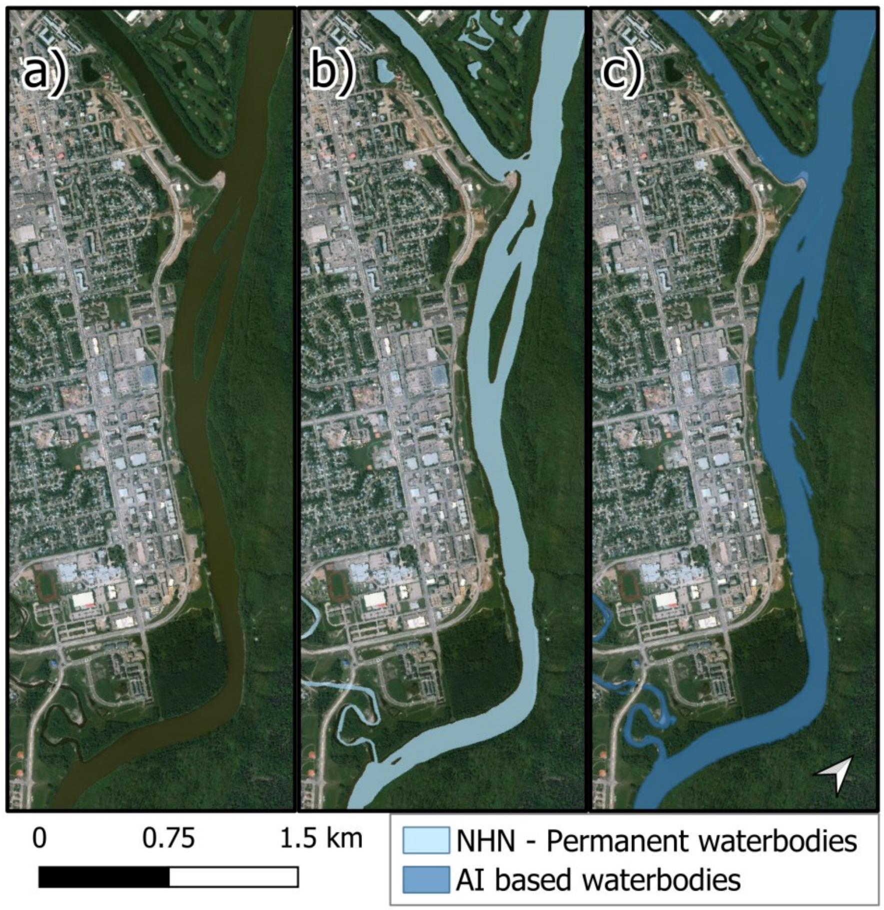

Figure 9. Comparative map showcasing the overlaid NHN and AI based waterbodies in the Fort McMurray town extent. a) Aerial image, b) NHN permanent waterbodies, c) AI based waterbodies.

The workflow for the second set of waterbodies from Natural Resources Canada, Government of Canada (2020), the Geo Deep Learning involves the AI raw extraction of water features, a post-processing phase that refines the delineation of the extracted features by reducing the number of non-stream vertices in the polygons. Observations suggest that the waterbodies dataset from Geo Deep Learning was more accurate and was therefore used for the study.

3.4.3. Flood extent

A flood extent polygon dataset was available for the flood event from NRCAN, and an additional manually-drawn flood polygon was generated. The NRCAN flood polygons correspond to images from April 28, 2020, and were obtained from the Floods in Canada archive (Government of Canada, 2023b). This dataset, however, did not match the aerial photos of the flood event. Therefore, a hand-drawn flood extent polygon for the flood event was prepared by superimposing the Aerial Photos and surveyed HWMs of the flood event. Only the hand-drawn polygon was utilized.

3.4.4. HEC-RAS calibrated model

A validated 1D Steady flow HEC-RAS model calibrated for the 2020 Fort McMurray event was provided by Alberta Environment and Protected Areas (AEPA; N. Kovachis, pers. communication, May 30 2023). The steady state WSL output of the HEC-RAS model exhibited gaps in two cross-sections, attributed to “digital levees” that restricted the flow of water from the river to the Fort McMurray downtown area. Figure 10 illustrates these gaps, depicted as white areas within the flooded extent polygon outline, where the HEC-RAS WSL layer is visible. This observation suggests that during the model run water was unable to flow upwards, resulting in erroneous gaps in the water elevation layer. This problem stemmed from the presence of high upstream levees designed to curtail inundation.

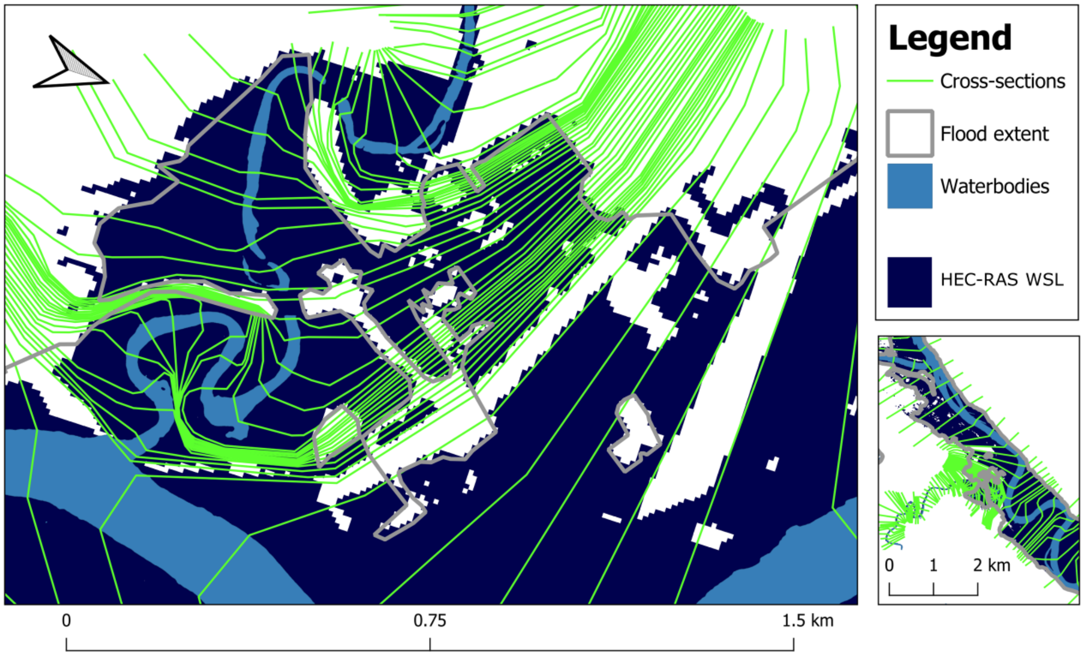

Figure 10. Cross section and WSL for Fort McMurray from the calibrated HEC-RAS model for the 2020 ice jam flood event. The green lines show the cross sections, the grey lines delineate the hand drawn flood extent, the light blue shows the permanent water bodies, and the dark blue shows the HEC-RAS derived flooded area.

3.4.5. Aerial images

Aerial images of the flood event were taken on April 28, 2020, at a resolution of 0.15 meters and a World Equidistant Cylindrical projection (EPSG) with a specific Coordinate Reference System (CRS) of 3779 and are provided under a licensing arrangement from Open Government Licence – Alberta. They were shipped by AEPA Geospatial Data Distribution Provincial Centre (AEP.Data@gov.ab.ca) via portable Hard Drive (AEPA; M. Currie, pers. communication, Dec 14, 2022) and required 40.8GB of storage space.

3.4.6. High Water Marks

A total of 67 HWM were surveyed by Alberta Environment and Protected Areas (AEPA) on May 1, 2020. Of the 67 HWMs, several were collected north of the Athabasca River, beyond the scope of the case study area. Some were obscured by dense forest cover, while others were situated beneath roof structures. The majority were tagged at ground level, with a few affixed to objects within the flood boundary. The HWMs were initially referenced under the Canadian Geodetic Vertical Datum CGVD28 system and maintained a reference time for the Global Positioning System (GPS) epoch of 2002.

4. Methods

This chapter outlines the methods employed for assessing hydro-correction algorithms, generating and evaluating HAND maps, and deriving flood depth results, along with their subsequent evaluation.

In section 4.1, the data processing steps are presented. In section 4.2, the methodologies for hydro-correction generation and evaluation, as well as HAND map generation and evaluation, are introduced. Specifically, in section 4.2.1, the overall hydro-connectivity of the hydro-correction algorithms to drainage is assessed, and alterations to the original case study DEM are examined. In section 4.2.2, the methods employed for generating HAND maps are detailed, along with their assessment. Section 4.3 covers the fast response depth estimation for RICorDE and FwDET, as well as their methods of evaluation. Section 4.3.1 focuses on the calibration process of RICorDE, while section 4.3.2 discusses how FwDET was executed; both explain the methodologies employed for their evaluation. Lastly, section 4.3.3 presents the methodologies used to evaluate the flood depth raster, with section 4.3.3.1 covering the HEC-RAS depth correlation and section 4.3.3.2 addressing the high water mark validation. A visual representation of the workflow followed to generate fast response flood depth estimations is presented in Figure 11.

The workflow shows three main steps: 1. Data collection, 1.1 DEM hydro-correction, 2. Depth estimation, and 3. Evaluation.

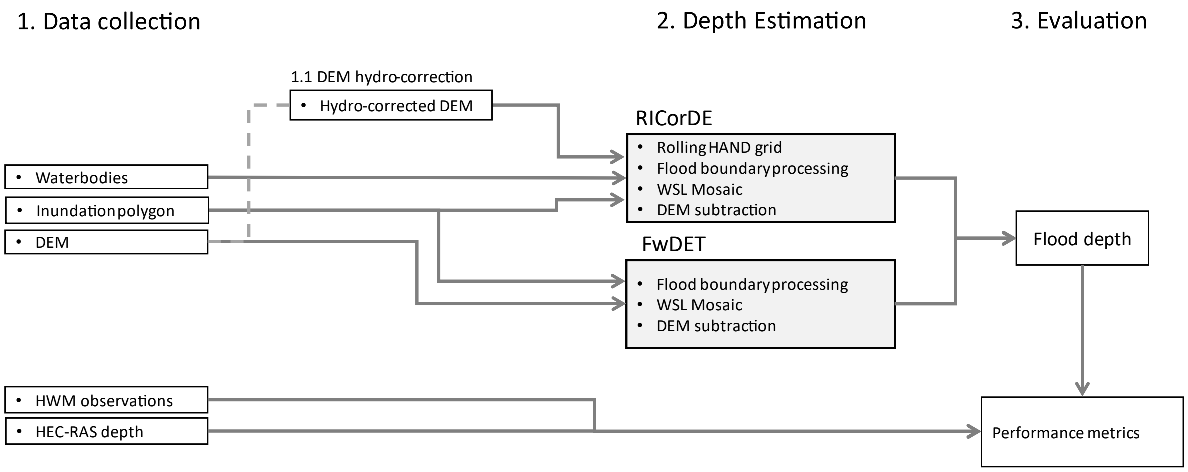

Figure 11. Fast response flood depth estimation workflow followed for the generation of depth maps of RICorDE and FwDET.

4.1. Data processing

Data processing was necessary for some datasets to ensure their validity or compatibility with other datasets and tools. Table 5 lists the datasets processed and the necessary changes. The DEM processing involved a resampling in 32-bit float format with bilinear interpolation using "*GDAL: Warp*", which changed its grid cell resolution from 0.5 meters with 1,932,374,592 cells to 10 meters with 4,830,997 cells. Waterbody geometries were fixed using QGIS engrained tools and small waterbodies including ponds, minor streams, and false waterbodies were manually removed. The hand-drawn flood extent required no modification. The HEC-RAS model levees were increased to allow upstream water flow and permit inundation along problematic cross-sections (Figure 10). The resulting depth from the steady flow HEC-RAS run was used as a validation point in the correlation analyses. The aerial images did not require any processing. Lastly the surveyed HWM elevation and location data for the event were converted to match the DEM, by adjusting the default GPS epoch of the HWMs from 2002 to 2011 using the NRCAN tool TRX (Government of Canada, 2022), and CGVD28 datum to the CGVD2013a using NRCAN tool GPS·H

(Government of Canada, 2023c). The HWM conversion was required for it to be compatible with the case study DEM.

Table 5. Processing underwent to each of the datasets utilized in this research.

#	Dataset	Processing underwent
1	DEM	Resampled to a 10-meter resolution, 32-bit Float format with Bilinear interpolation using GDAL: Warp.
2	Waterbodies	Fix geometries and the removal of relatively small waterbodies including ponds, minor streams, and false waterbodies.
3	Flood extent	Hand-drawn flood extent did not receive additional processing
4	HEC-RAS model	Levees at problematic cross-sections lowered.
5	Aerial images	Aerial images did not receive any type of processing
6	HWM	GPS epoch 2002 to 2011 using the NRCAN tool TRX, and from CGVD28 datum to CGVD2013a using NRCAN tool GPS·H

4.2. Hydrologic terrain analysis tools

Hydrologic terrain analysis tools work with DEMs to derive various hydrological parameters such as flow direction, flow accumulation, drainage networks, and watershed delineation. This thesis uses HAND maps to evaluate flood map generation. HAND maps encompass hydro-correction techniques and there are different methodologies to generate HAND maps. Prior to generating HAND datasets, hydro-connection towards a stream for each cell of the DEM is advised. This hydro-connection can be achieved through hydro-correction algorithms; however, there are numerous algorithms and methods available. For this reason, a group of hydro-correction methodologies were tested to ensure the correct generation of the HAND map. Additionally, two HAND map generation approaches are outlined. Both methods determine the drainage boundary for the HAND maps differently, with the first determining elevation with respect to a threshold-based streamline and the second with respect to a user input water-land boundary.

4.2.1. Hydro-correction method evaluation

Many hydro-correction algorithms exist (Table 2). Hydro-correction algorithms facilitate the creation of DEMs that ensure continuous flow towards the designated DEM exit point. This continuous flow characteristic in DEMs is essential for generating HAND maps, as they rely on accurate drainage assignment. This section uses hydro-correction algorithm methods exclusively from the WhiteboxTools QGIS plugin (Lindsay, 2014) v2.3.0. The hydro-correction algorithms from the WBT QGIS plugin were tested and evaluated towards drainage hydro-connection. The name of the hydro-correction tools presented in this section is listed in Table 6, these being grouped into filling and breaching methodologies. The filling methodologies are typically not very adjustable while breaching methodologies typically present a degree of customizability. Because most of the evaluated methodologies have little to no parameters these were not altered for this study.

The performance of the hydro-correction algorithms was quantitatively evaluated by determining the number of alterations to the original DEM and the number of cells hydro-connected to the waterbody boundary. The DEM utilized for this analysis underwent the same processing as the one utilized for the Fort McMurray 2020 case study (Table 5), this being a Float32 10m bilinear DEM.

Table 6. Evaluated Depression Fixing Approaches from WhiteboxTools

WBT	**Filling**	a.	FillDepression
		b.	FillDepressionPlanchonAndDarboux
		c.	FillDepressionWangAndLiu
		d.	FillSingleCellPits
	Breaching	a.	BreachDepression
		b.	BreachDepressionLeastCost

The hydro-corrected dataset evaluation consisted of determining the number of cells altered from the initial dataset, named *Cells altered*, the percentile cumulative change in elevation expressed as:

Overall change = ((Total cumulative elevation after filling - Total cumulative elevation) / (Total cumulative elevation)) x 100

Where:

- *Total cumulative elevation* = the sum of elevation for all the cells in the case study extent
- *Total cumulative elevation after filling* = the sum of filled cells in the case study extent.

Additionally, the hydro-connection from each hydro-correction tool was tested with the ElevationAboveStream tool, which does not generate cells when these do not connect with the water-land boundary. The percentage of grid cells hydro-connected to the waterbodies boundary is defined *Effectiveness*. Finally, the processing speed for each of these hydro-correction methods under their default parameters was evaluated using a computer with an Intel(R) Core(TM) i7-10750H CPU @ 2.60GHz and 16GB of RAM.

4.2.2. Height Above Nearest Drainage generation and evaluation

To evaluate the validity of HAND generation methodologies implemented in this study the two known methods were employed to generate HAND datasets of the Fort McMurray area and evaluated under the generation of flood maps and gridded flood depth maps. Both HAND generation methods were conducted in QGIS v3.32 and the DEMs were filled using the Wang and Liu (2006) methodology.

Both methodologies differ in the way in which they define drainage. The first HAND map generation method was conducted using the GIS and remote sensing software package WhiteBoxTools v2.3.0 tool ElevationAboveStream. ElevationAboveStream creates HAND maps relative to a waterbody boundary polygon. The second HAND map generation method uses the map algebra and environmental dynamic PCRaster v0.3.0 QGIS plugin processes to generate a HAND map relative to a streamline. The waterbodies utilised from the first methodology are the same listed under Table 5, while the streamline used in the second methodology was derived from a flow accumulation threshold. For the second methodology, delineating streamlines from a flow accumulation process enables the precise automated depiction of stream distribution harmonized with the drainage network.

The compiled script to generate HAND maps following the PCRaster method is found at Appendix D. The script was run in QGIS v3.32 with the QGIS PCRaster plugin installed (plugins.qgis.org/plugins/pcraster_tools, Karssenberg et al., 2010) with an input accumulation threshold of 100,000 cells. The main steps followed by the presented script that generate the HAND map in relation to the streamline are the following:

1. Generate flow direction by assigning a value from 1 to 8 of each cell of the DEM.
2. Determine accumulated material flowing into each downstream cell.
3. Extract accumulated cells following input threshold.
4. Generate sub-catchments from flow direction and extracted accumulated cells.
5. For each cell, assign the minimum value of the cells that belong to the same area to the cell itself.
6. Subtract the DEM from the previous step to obtain the HAND map.

To derive a flood extent map from the HAND maps the elevation values located under the HWMs “should be 0” category was sampled, possible outliers were filtered by removing q1 and q3 sampled values, finally the rest of the HAND elevation values were averaged. Furthermore, to assess the performance of both HAND maps in generating flood extent maps, both were later evaluated using a confusion map and matrix later presented in section 5.2. A confusion map facilitates the visualization of the results depicted in the confusion matrix, showcasing the spatial distribution of classification errors by classifying each cell as one of four of the following types. "True Positive" indicates cases where the model accurately predicts the positive class, while "True Negative" denotes accurate predictions of the negative class. On the other hand, "False Positive" refers to instances of erroneous positive predictions, and "False Negative" represents instances of mistaken negative predictions. The equations used to generate the confusion map were applied within the QGIS Raster Calculator and for the matrix on Excel. The equations are the following:

- for True Positive (TP), *("Tool" > 0) AND ("HECRASdepth" > 0)*
- for True Negative (TN), *("Tool" <= 0) AND ("HEC-RASdepth" <= 0)*
- for False Positive (FP), *("Tool" > 0) AND ("HECRASdepth" <= 0)*
- for False Negative (FN), *("Tool" <= 0) AND ("HECRASdepth" > 0)*

Where “*Tool*” is either PCRaster HAND map or ElevationAboveStream HAND map and “*HECRASdepth*” is the calibrated HEC-RAS flood depth.

4.3. Fast response flood depth estimation tools generation and evaluation

For the case study, a flood depth layer for each tool was produced using both RICorDE and FwDET, with one set in their default form and the other in their calibrated/altered form. The processed datasets presented in Table 5 were the initial inputs for the runs. The workflow of both tools is shown in Figure 12. Later in this section, the methodologies utilized to generate flood depth estimations under the Fort McMurray 2020 ice jam flood event as well as the methodologies used to evaluate their results against observed values are presented.

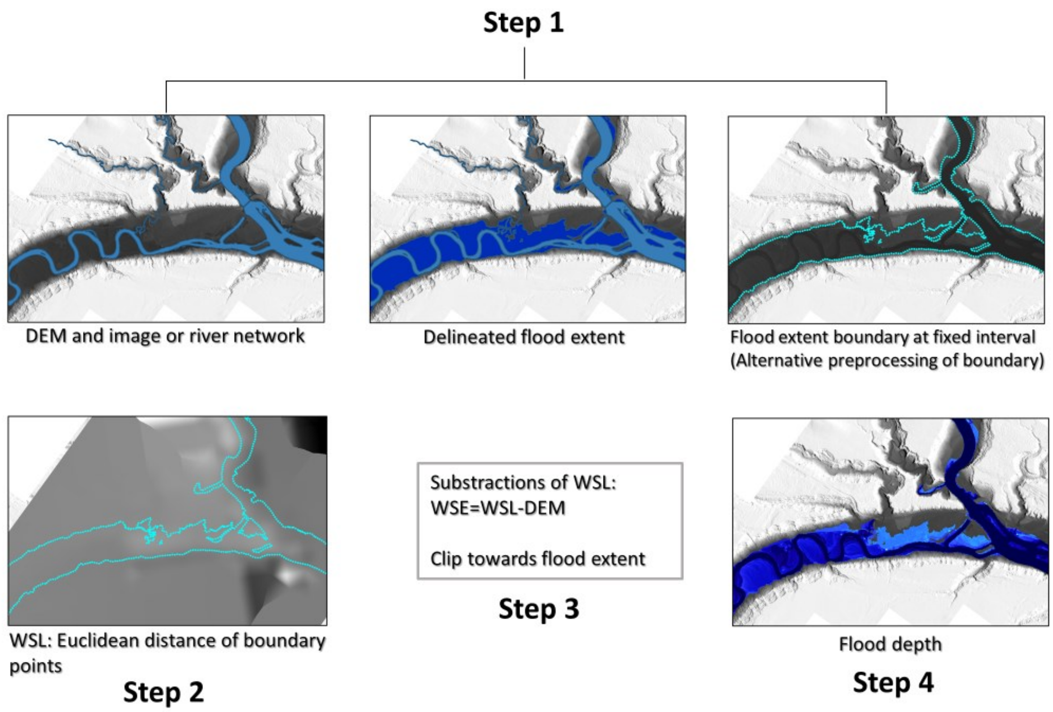

Figure 12. Simplified rapid response flood depth generation workflow. Reproduced from Hao et al. (2021).

4.3.1. Flood depth estimations using RICorDE v1.0.1

The instructions as well as the algorithm to run RICorDE v1.0.1 are in its GitHub repository (NRCan, 2023).

Prior to the RICorDE run, the case study inputs listed in Table 5 were clipped to match the area of interest. The waterbodies were transformed into raster format using the *"Rasterize"* tool within the QGIS toolbox. The rasterized output matched the pixel size, width, and height of the clipped DEM. The rasterization of the waterbodies was an important step, it assured compatibility within the tools integrated in the RICorDE workflow, otherwise incompatibilities related to dimensions within the tools may be encountered.

Three distinct RICorDE datasets are presented in this study. The first presents RICorDE in its default form, the second presents it after calibration, and the last presents the same calibrated RICorDE model, but uses an alternative HAND layer.

The alternative HAND layer defines drainage as a streamline derived from D8 flow accumulation algorithms with a threshold of 100,000 cells.

Default RICorDE parameters produced inundation gaps within the Fort McMurray town area. Thus, parameter calibration was conducted with a focus on improving the accuracy of flood extent representation. The calibration process aimed to increase the number of true positives inside the Fort McMurray town area flooded domain. The specific iterations and parameter alterations of RICorDE are detailed in Table 7. The final parameter calibration is as follows:

```
[b1Bounds]               Filter values for the HAND beach values
qhigh=0.6                Quartile to use for upper bound
cap=7.8                  Maximum value to allow for upper bound
qlow=0.1                 Quartile to use for lower bound
floor=0.5                Minimum value to allow for lower bound
[beach2]                 HAND value samples on inun2 beach
method=pixels            Method for extracting beach from the inundation raster
[hgInterp]               Interpolated beach2 HAND values
distP=2.0                Distance coefficient for whitebox.IdwInterpolation
pts_cnt=5                Number of points to include in search (IdwInterpolation)
[hgSmooth]               Smoothed rolling HAND grid (low-pass filtering)
raster resolution *3
max_grade = 0.1          Maximum hand value grade to allow (hg:smooth)
neighborhood_size = 1    Neighbourhood size for grass7:r.neighbors
max_iter=2               Maximum number of smoothing iterations to allow
precision=0.1            Precision of resulting HAND values
[hInunSet]               Set of HAND inundation rasters
animate=False            Flag to create animations of outputs.
[hWslSet]                Set of WSL rasters
max_fail_cnt=5           Maximum number of wsl failures to allow
[depths]                 Gridded depths
precision=5              Rounding to apply for delta calculation
```

Table 7. RICorDE calibration iteration showing the datasets utilized, parameters changed and observations.

#	Run name	GDAL: Warp	Flood polygon	Waterbodies	Parameter changes	Observations
1	default_floodCANpoly	Bilinear, 10m, Float33	Floods in Canada	NRCAN AI waterbodies	cap from 7 to 9	Underestimations within low slope regions
2	default_hand-drawnpoly	Bilinear, 10m, Float33	Hand Drawn	NRCAN AI waterbodies	cap from 7 to 9	Underestimations within low slope regions
3	low-smooth	Bilinear, 10m, Float33	Hand Drawn	NRCAN AI waterbodies	cap from 7 to 9, Smooth iter from 5 to 1	Depth decreased within beach.
4	low-smooth2	Bilinear, 10m, Float33	Floods in Canada	NRCAN AI waterbodies	cap from 7 to 9, Smooth iter from 5 to 2	Lower flood depth within beach areas.
5	neighbors	Bilinear, 10m, Float33	Floods in Canada	NRCAN AI waterbodies	cap from 7 to 9, Smooth iter from 5 to 2, Neighbors size 7 to 1	Needs tweeks on qhigh. Would use a tweeked version over 4
6	precision-calibration	Bilinear, 10m, Float33	Floods in Canada	NRCAN AI waterbodies	cap from 7 to 9, Smooth iter from 5 to 2, Neighbors size 7 to 2, precision from 1 to 5	Increase in beach values ranging around 0.005m. Depth is also 0.01m higher than previews in some areas.
7	qhigh-calibration	Bilinear, 10m, Float33	Floods in Canada	NRCAN AI waterbodies	cap from 7 to 7.8, Smooth iter from 5 to 2, Neighbors size 7 to 2, precision from 1 to 5, qhigh from 0.9 to 0.7	Reducing qhigh lowers HWM connectivenes on beach depth (#40&41), and some flood boundary (#16 to 20).
8	HAND-ofp	Bilinear, 10m, Float33	Floods in Canada	NRCAN AI waterbodies	cap from 7 to 7.8, Smooth iter from 5 to 2, Neighbors size 7 to 2, precision from 1 to 5, qhigh from 0.9 to 0.7, HAND inserted to ofp	Increases depth and extent in some area.
9	handDrawnPoly	Bilinear, 10m, Float33	Hand Drawn	NRCAN AI waterbodies	cap from 7 to 7.8, Smooth iter from 5 to 2, Neighbors size 7 to 2, precision from 1 to 5, qhigh from 0.9 to 0.7	Beach extent is greater and so is its overall depth within mid-sections.
10	handDrawnpoly_HAND-ofp	Bilinear, 10m, Float33	Hand Drawn	NRCAN AI waterbodies	cap from 7 to 7.8, Smooth iter from 5 to 2, Neighbors size 7 to 2, precision from 1 to 5, qhigh from 0.9 to 0.7, HAND inserted to ofp	Similar to the previews. Good overlay with 10 when low values.

4.3.1.1. RICorDE calibration iteration

Model calibration, as defined by WT Tech (2024), refers to the process of adjusting a model by incorporating information, often from experimental data, to enhance its accuracy or predictive capability. It involves fine-tuning the model parameters to align its outputs with observed data, ensuring that the model provides reliable and meaningful results. As mentioned in Section 4.3.1, the default parameters of the RICorDE algorithm initially resulted in inundation gaps within the Fort McMurray town area, covering 74% of the area determined as flooded. A calibration step then used the base flood boundary of the flood event as a reference, and alteration of RICorDE parameters resulted in an increase of flooded cells along the boundary that covered 97% of the area determined as flooded. The percentage of true inundated extent along the calibration was quantified as the ratio of the modelled flood area to the total flooded area, expressed as *Effectiveness = Modelled flood / Flooded area*.

Calibrating RICorDE and its parameters required adjusting its hydro-correction method, Neighbours, Precision, and qHigh parameters (detailed in Table 7). The default settings and calibration used in this study may not apply to every flood scenario. Calibration is likely to be specific to each flood event, requiring re-calibration for each case study. The first calibration iteration changed the hydro-correction method within the RICorDE algorithm. For this step, the understanding acquired in section 4.2.1 allowed a proper selection of a hydro-correction method resulting in an increase in coverage (Figure 13b2). Increasing neighbors and precision resulted in an increase of the beach values, important to increase extent coverage. Finally, the qhigh filter was applied to the flood boundary. This last iteration achieved an overall coverage of 88% in the area presented in Figure 13b4 and was the flood depth output evaluated on later sections.

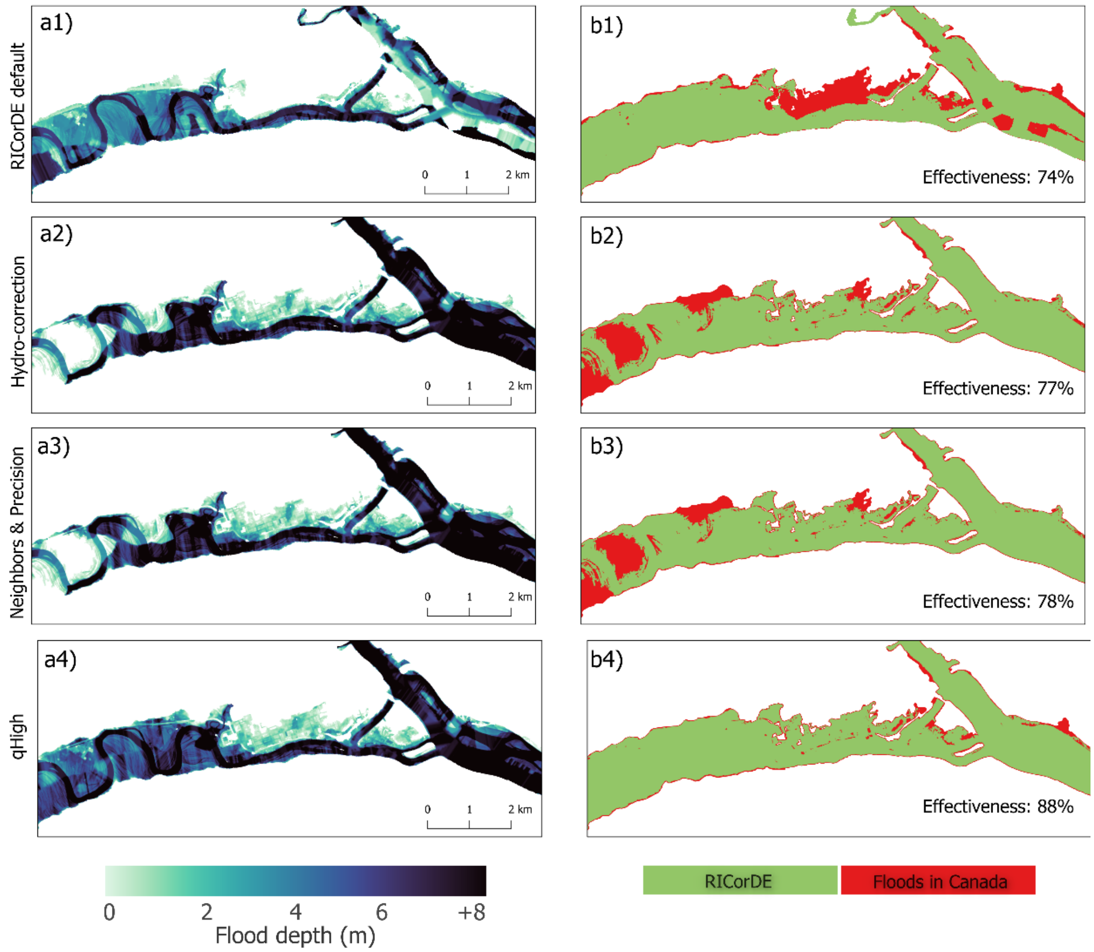

Figure 13. RICorDE calibration analysis. a1 to a4 show the flooded output while b1 to b4 the flooded output extent overlaid over the Floods in Canada flooded extent. Parameters altered are the following: a1) Default parameters (None), a2) Hydro-correction method, a3) Lower closest neighbors and increased precision, a4) Decreased qHigh. The green along the b column represents the RICorDE flooded area (>0) while the red the flooded area from Floods in Canada. Figure reproduced from Bryant et al. (2023).

4.3.2. Flood depth estimation using FwDET v2.1

The FwDET v2.1 runs were carried out by using its QGIS script accessible through its GitHub repository (CSDMS-contrib, 2023), using the DEM and flood polygon listed in Table 5 as its inputs and following the repository instructions. Flood depths via FwDET were incorporated as a comparison for RICorDE. This decision was prompted by the recent introduction, in FwDET version 2.1, of a preprocessing method aimed at removing flood boundary outliers through slope filtering. This method goal is to produce a smoother WSL by effectively eliminating outliers. By employing this methodology to evaluate RICorDE, we can also gauge the effectiveness of its slope filter. This will involve comparing its performance under default non-preprocessed conditions with its performance under processed conditions.

The complete methodology for computing FwDET water depths is detailed in the works of Cohen et al. (2018) and Cohen et al. (2022) and is as follows:

a) First, the inundation polygon is converted into a polyline layer, and a raster layer with the same grid-cell size and alignment as the input DEM is generated.
b) Then, the DEM values for these grid-cells, referred to as boundary grid-cells, are extracted.
c) Next, the boundary grid-cells are processed. The processing involves an optional averaging and filtering of outliers based on terrain inclination.
d) The next step entails using the nearest boundary grid-cell to assign the local floodwater elevation to each grid-cell within the flooded domain.
e) Finally, the floodwater depth is computed by subtracting the local floodwater elevation from each grid cell to the terrain elevation within the flooded domain.

Three different sets of flood depth outputs were generated using the FwDET tool. The first using the default parameters, the second applying a 3% slope filter, and the last with the 3% slope filter with HAND layer as input. The HAND layer utilized was generated using the PCRaster script with an D8 accumulation threshold of 100,000 cells.

4.3.3. Flood depth results methods of evaluation

In this section, the evaluation methods that assess the performance of RICorDE and FwDET against the case study observed values are outlined. The evaluation comprises two sections, validation using the calibrated HEC-RAS model output (Section 4.3.3.1.) and validation using the surveyed HWM depth (Section 4.3.3.2.).

Additionally, several statistical and visualization approaches were used. To evaluate flood extent, a confusion matrix and a confusion map were generated. For visualizing depth differences between predicted and actual depth grids, a difference map was created. To demonstrate the relationship between gridded cell depths, a linear regression heatmap was generated. A histogram illustrating the distribution of cells elevations was produced to showcase cell distribution. The surveyed HWMs of the flood event were utilized to assess the accuracy of depths derived from RICorDE and FwDET under the filtered HWMs, representing flood depth.

4.3.3.1. Evaluation with the calibrated HEC-RAS depth

The methods used to validate RICorDE and FwDET against the calibrated HEC-RAS model derived water surface layer depth are presented in the following order: confusion matrix and map for extent validation, difference map to evaluate visual differences in depth, linear-regression heatmap for depth correlation, and histogram for cell distribution.

The evaluation methods aimed to validate the spatial distribution of flood grids generated by RICorDE and FwDET through comparison with the calibrated HEC-RAS model grids. A confusion matrix and map (as explained in section 4.2.2.) were implemented for this validation. The equations utilized for generating both the confusion map and matrix are the following:

- for True Positive (TP), *("Tool" > 0) AND ("HECRASdepth" > 0)*
- for True Negative (TN), *("Tool" <= 0) AND ("HEC-RASdepth" <= 0)*
- for False Positive (FP), *("Tool" > 0) AND ("HECRASdepth" <= 0)*
- for False Negative (FN), *("Tool" <= 0) AND ("HECRASdepth" > 0)*

Where "*Tool*" is either RICorDE or FwDET and "*HECRASdepth*" is the calibrated HEC-RAS flood depth. Note that the confusion map was implemented using the QGIS Raster Calculator and the confusion matrix with Excel.

The difference map shows depth variations between both RICorDE and FwDET by following the equation *Difference = Modelled - Tool* where *Tool* is either the RICorDE or FwDET flood depth and *Modelled* is the calibrated HEC-RAS model depth.

It was generated under QGIS Raster Calculator, and the differences are presented via a color scale.

Similarly, a linear regression was applied to correlate the data points, providing insights into the relationship between the tool and validation points using linear-regression and metrics of evaluation. Due to the extensive data, a heatmap was utilized for visual representation of the linear regression correlation. Heatmaps employ color gradients in a two-dimensional space to depict the density, intensity, or concentration of values within a matrix or grid. Post heatmap evaluation, the area was categorized into three distinct domains for tool performance assessment. The *'Full domain'* covered the entire area of interest, totaling 97,040 assessed cells. The *'Clearwater River'* domain focused on the region along the river, encompassing 82,275 assessed cells. Lastly, the *'Fort McMurray town'* domain represented the town area and comprised 18,555 cells. For each of these cells, depth values for the default, calibrated and validation point were extracted. To sum up results from the heatmap evaluation, a table showcasing a number of metrics that summarizes the overall range, typical value, and variability within the dataset is presented for each of the domains and tools. The maximum and minimum values indicate the extremities of the data, while the average and median provide insights into the central tendency. Additionally, the standard deviation offers a measure of the data spread around the mean (Australian Bureau of Statistics., 2024), and the interquartile range highlights the dispersion of the middle 50% of the dataset (Statistics By Jim., 2021).

Lastly, a histogram was used to compare the cell distribution of the dataset against the observed values. The histogram interval was 0.1 meters and was limited to the "Full extent" domain defined previously. To facilitate the visualization of the histogram, a smooth average of the histogram values was computed and presented. To evaluate the similarities of the histogram with the modelled and calibrated cell distribution, a Chi-Square Test was conducted using the predefined Excel function CHISQ.TEST.

4.3.3.2. High Water Mark validation

Most of the surveyed HWM were strandlines delineating extent not depth. Therefore, during their processing the HWMs were categorized into groups through the examination of the HWMs location (interpolating the flood event aerial imagery) and description. A group of HWMs did not fall into the case study extent and others did not contain data, which reduced the number of available data points to 55 of the original 67. Table 8 lists the HWM categories. Most categories are self explanatory, including "*At ground level*", which presents strandlines positioned along the flood boundary; "*Above ground*", which presents above ground level or flooded cells; "*Unclear*", which were found along dense woodland or could be potentially misinterpreted because of their description "*Unreliable*", which exhibits descriptions that suggest inaccuracy or depths lower than zero meters when transformed to depth; "*Outside available area*", which are HWMs encountered outside the DEM extent; and "*No data*", which are points that lack geographical or elevation information.

Table 8. Surveyed high water mark Categories and Counts.

	Count
HWM Category	**Surveyed**
At ground level	17
Above ground	8
Unclear	18
Unreliable	10
Outside of available area	10
No data	2
Total	67

The HWM then underwent processing to match the DEM datum and epoch (see section 3.5.7.). Then, the HWMs categorized as "*Above ground*" were converted to depth following the equation *Depth = HWM – DEM*. To validate the modelled depths produced by RICorDE and FwDET against the observed HWM depths, the derived depths were plotted, and differences were quantified using RMSE analysis (Refer to section 5.3.2 for details).

5. Results and Discussion

This section presents and discusses the findings from the hydro-correction evaluation, HAND map algorithms, and both fast-response flood depth estimation algorithms applied to the Fort McMurray 2020 ice jam flood. It also discusses data limitations for the case study event.

5.1. Hydro-correction methods evaluation results and discussion

Six hydro-correction algorithms were assessed in terms of their performance in fixing DEM depressions. Figure 14 displays the number of hydro-connected cells, which are the cells with continuous flow leading to the predefined water-land boundary of the DEM. The assessment involved the examination of the altered DEM properties such as the number of cells hydro-connected towards the stream water-land boundary, and determining the extent and impact of alterations made to the DEM. Each panel in the figure corresponds to a hydro-correction tool, beginning with the bilinear DEM, followed by FillSingleCellPits, FillDepressionPlanchonAndDarboux, FillDepressionWangAndLiu, BreachDepression, and BreachDepressionLeastCost.

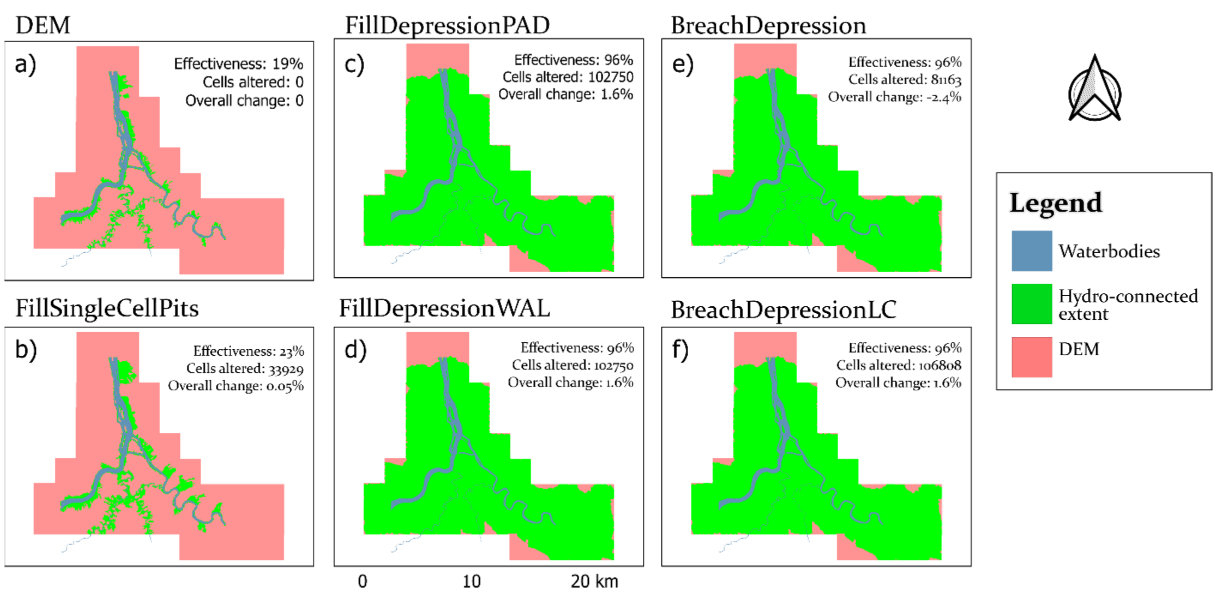

Figure 14. Percentage of cells from the depression fixing methodologies hydro-connected towards the stream polygon. Hydro-connected coverage percentage defined as Effectiveness, total

number of cells that were altered defined as Cells altered, and cumulative percentile change in elevation defined as Overall change.

The case study covers an area of 24,564,000 m^2, with the river waterbody polygon covering 1,354,660 m^2 of that area. Figure 14 presents the hydro-correction evaluation results, where hydro-connectivity towards the stream was measured for the hydro-correction methodologies. Figure 14 results suggest that a lack of hydro-correction makes hydrological tools reliant on flow direction and accumulation relatively useless, resulting in a hydro-connectivity towards the stream water-land boundary of 19% of the case study extent with 5.5% of it being just the river. Similarly, a fill single cell pits algorithm achieved the lowest coverage as well as the lowest number of altered cells among the evaluated tools and an overall hydro-connectivity of 23%; Lindsay (2016) suggests fill single cell approaches are intended to be paired with other types of correction tools, and the low hydro-connection achieved by this approach corroborates that observation. In contrast, evaluation of both filling and breaching approaches achieved a coverage of 96% of the total cells connected to the stream boundary with an overall cumulative elevation change of 1.6% of the total cells being altered. However, the least cost breach approach resulted in a slightly higher number of cells being altered, with 106,808 cells altered instead of 102,750. Notably, BreachDepression under its default parameters was the only to carve streams resulting in 81,163 cells being altered and burned, resulting in an overall cumulative elevation change of -2.4% of the total cells being the only approach that under its default parameters decreased elevations along the flow path.

Interestingly, depression filling algorithms, such as Planchon and Darboux (2002) and Wang and Liu (2006), produced the same number of alterations and extent, and thus created the same dataset; however, Wang and Liu (2006) required a lower computational time. This result matches Wang and Liu (2006) literature, which states that the implementation of a time complexity of $O\,(N \log 2\,\mathrm{N})$ in its methodology decreased computational time. Note that the FillDepression approach presented by WBT achieved the fastest computational time, however, was not presented in the results figure because of its identical outcome to the other filling approaches. In the context of the study objectives, the Wang and Liu (2006) filling approach was preferred over the others because of its simplicity, faster processing, and extensive literature.

The evaluation of processing time of the hydro-correction tools presented in Table 9 revealed that the filling WBT approach for depression filling (FillDepressions) achieved the fastest computation time of 0.17s, followed by FillDepressionWangAndLiu at 0.69s. Of the breaching methodologies, BreachDepressionLeastCost achieved the fastest processing at 0.22s, followed by BreachDepression using drainage enforcing techniques at 2.41s.

Table 9. Processing speed of the Depression Filling method from the WBT provider is compared against a Float32 10m bilinear DEM for the Fort McMurray region.

#	WBT Depression Filling Algorithm	Processing speed
1	Wang and Liu (2006)	0.698s
2	Planchon & Darboux (2001)	2.168s
3	FillDepression WBT	0.173s
4	BreachDepressionLeastCost	0.220s
5	BreachDepression (Drainage enforcing)	2.41s
6	FillSingleCellPits	0.88s

Overall, the presented findings show that while applying different methodologies, in practice most tools achieve the same hydro-connected coverage with differences in the number of cells altered (Figure 14) and speed (Table 9). In this case study, Wang and Liu (2006) emerged as the preferred depression-fixing tool due to its extensive documentation and widespread presence in the literature. However, BreachDepressionLeastCost offered advantages in terms of lower computation time and greater customizability, rendering it valuable for a diverse array of scenarios when properly calibrated. Speed was not considered a significant factor in this decision due to the size of the processed case study dataset, resulting in a processing time of less than a couple of seconds. Additionally, the hydro-connected approach visualization (Figure 14c, d, e, f) reveal data gaps downstream the river caused by a lack of waterbody delineation on the northern DEM extent. Data gaps suggest the algorithm was unable to hydro-connect cells downstream where the case study waterbodies end because of the upstream slope and lack of drainage.

5.2. Height Above Nearest Drainage map results and evaluation

The two HAND maps generated for the Fort McMurray area are presented in Figure 15, which shows key differences between a HAND map where drainage is defined 1) at the water-land boundary of the waterbody polygon and 2) as a flow accumulation streamline. Specifically, the first HAND dataset has a lower overall elevation while the second HAND map has a higher elevation overall. The difference in elevation between both datasets is attributed to the difference in elevation of the defined drainage, hence one establishes drainage at the water-land boundary from both extremes of the river and the other in a polyline streamline along to the thalweg.

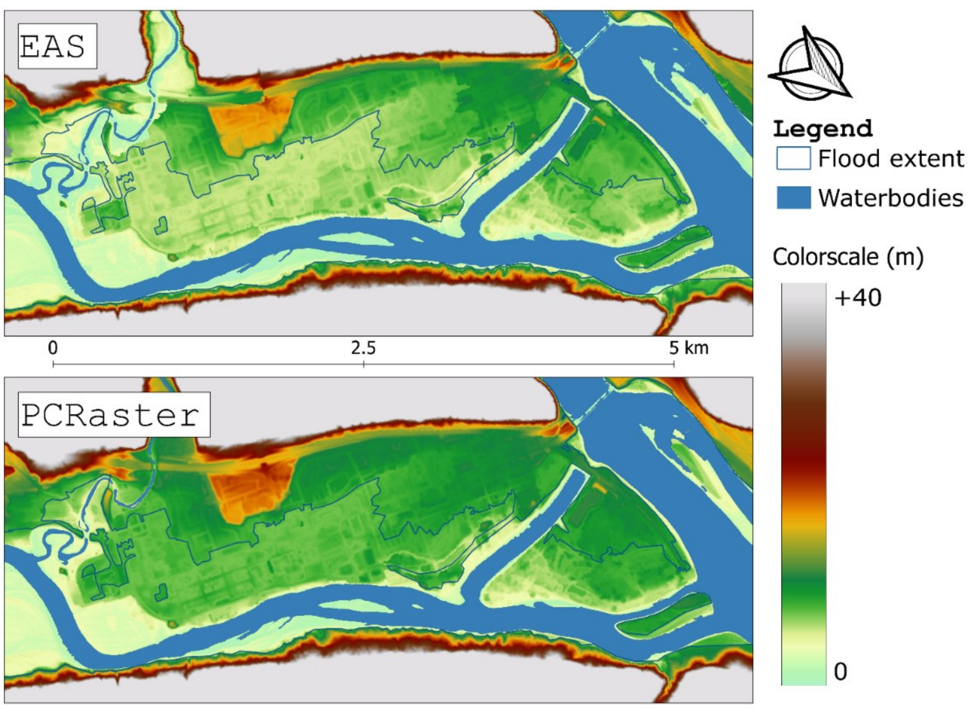

Figure 15. HAND datasets under the case study area. On the top we have the ElevationAboveStream algorithm, on the bottom we have the PCRaster script derived HAND layer.

HAND maps were employed to generate flood maps and for the flood depth analysis. The HWMs used to delineate the flood extent were averaged, and the value named "*NewAVG*" used to draw the flood extent is presented in Table 10. Resulting elevation values obtained from the averaging were used for the HAND derived flood extent evaluated in Figure 16 confusion map and matrix. Results indicate a higher number of accurate predictions of flood extent (True Positives; 19847 vs. 18947), a lower number of erroneous predictions (False Positives; 595 vs. 1495), and a lower number of mispredictions (False Negatives; 2325 vs. 2943) in the streamline-based HAND dataset. While the accumulation-based streamline HAND approach exhibited the opposite trend, it provided insight into the limitation of the methodology. For example, the extension of drainage towards the river boundary led to noticeable changes in the HAND catchment regions, possibly due to the presence of steep slopes along the water-land boundary.

Table 10. HAND flood extent processing underwent to the HWM categorized "above ground".

HAND HWM processing						
	MAX	MIN	Q1	Q3	AVG	NewAVG
EAS	7.24	6.15	6.39	7.03	6.66	6.53
PCRaster	9.04	7.06	8.00	8.68	8.21	8.10

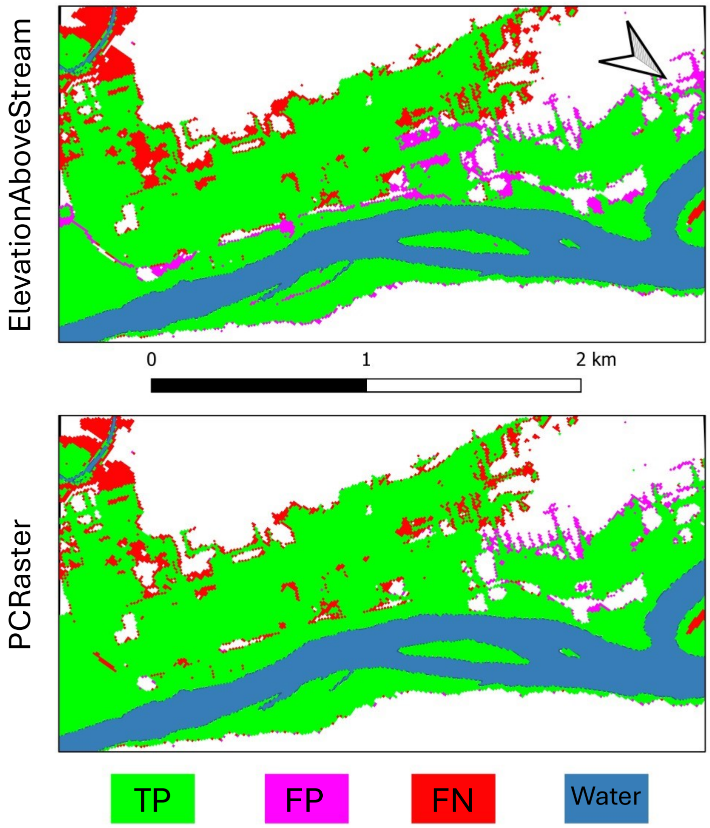

		HEC-RAS depth	
		Positive	Negative
EAS	Positive	18947	1495
	Negative	2943	

		HEC-RAS depth	
		Positive	Negative
PCRaster	Positive	19847	595
	Negative	2325	

Figure 16. Confusion map and matrix for both HAND methods explored against the calibrated HEC-RAS depth.

5.3. Gridded flood depths results

To assess the efficacy of the FwDET and RICorDE algorithms, the obtained depth grids were compared with the values from the calibrated HEC-RAS model and surveyed HWM. Specifically, depths from the calibrated version of RICorDE v1.0.1 and the slope-filtered FwDET v2.1 algorithm were benchmarked against the known values of the calibrated HEC-RAS flood depth. The comparison used two performance measures: 1) confusion and heat maps, and 2) the number of cells under each 0.1-meter elevation interval produced by the RICorDE, FwDET, HEC-RAS models The outcomes of these analyses are detailed in sections 5.3.1. and 5.3.2.

5.3.1. HEC-RAS flood depth correlation

Figure 17 visualizes each of the modelled case study depth grid layer outputs in their calibrated form, along with their percentile of flooded area not within the case study flooded polygon. This includes x) the calibrated HEC-RAS model WSL derived flood depth map, y) the calibrated RICorDE depth map, and z) the slope-filtered FwDET depth map. These flood depth layers underwent several evaluations presented in this section, beginning with a confusion map and matrix, followed by a difference map, linear regression, and analysis of gridded depth cell distribution.

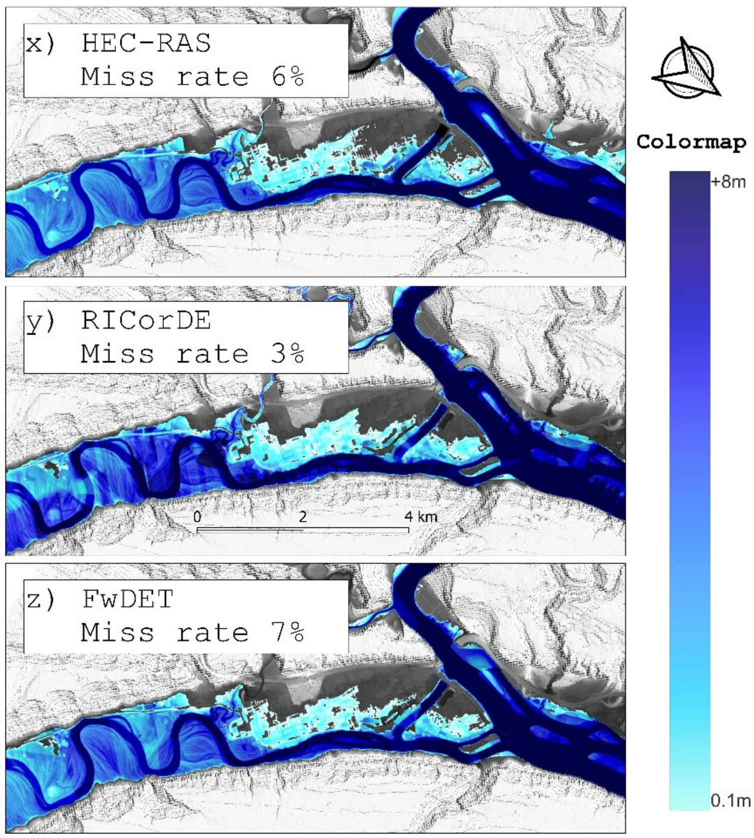

Figure 17. Flood depth maps for the 2020 Fort McMurray ice jam flood event, each displaying their respective miss rates, which were calculated using the case study flood extent. The miss rate was calculated as the percentile of depth extent not present in the case study flooded area.

The confusion matrix and map in Figure 18 show that RICorDE achieved a higher number of true positives than FwDET, achieved a higher number of accurate predictions (True Positives; 89,509 vs. 87,407) than FwDET, and a higher number of erroneous predictions (False Positives; 4,562 vs. 2,945), as well as a lower number of mispredictions (False Negatives; 1,266 vs. 3,368). RICorDE had a greater count of accurate predictions because it was calibrated to the flood extent polygon rather than the HEC-RAS depth. Thus, many of the false positives presented in the RICorDE flood depth extent were extensions of the beach values with depth values below 0.05 meters.

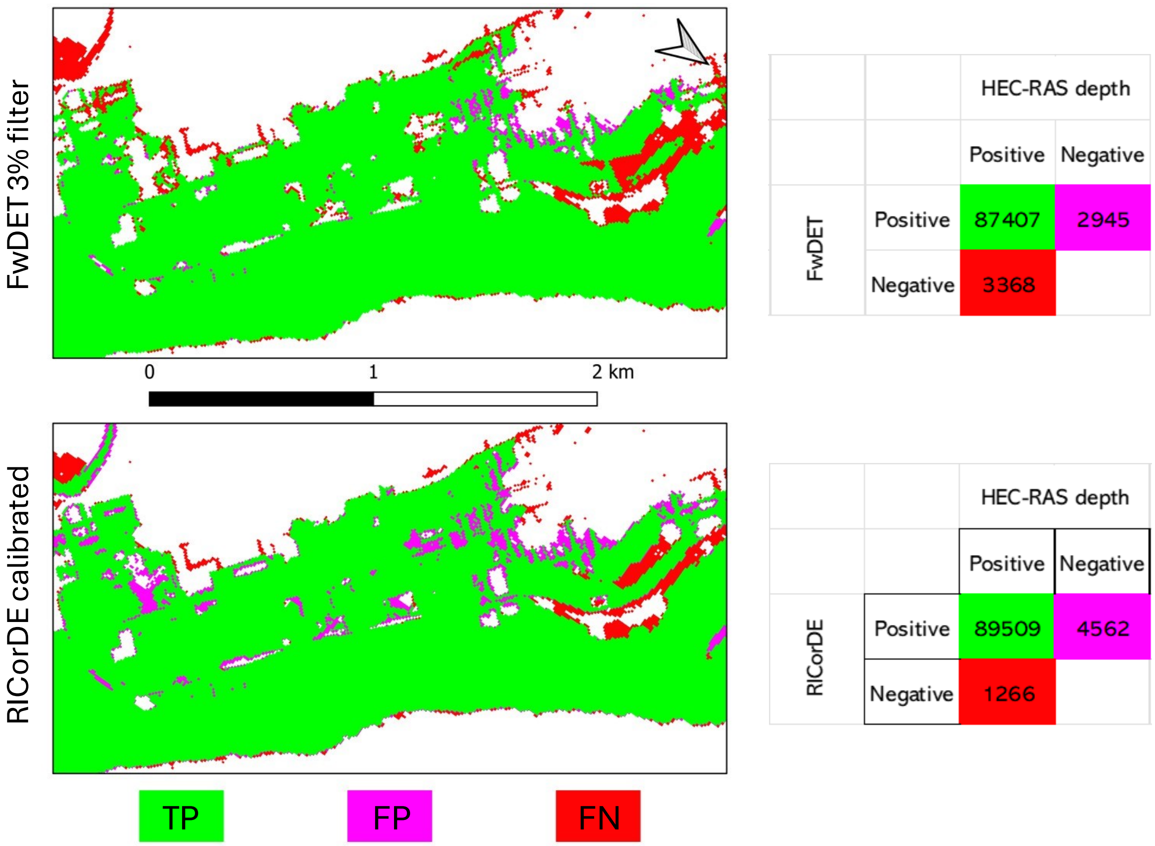

Figure 18. Confusion map illustrates the comparison between FwDET employing a 3% slope filter in the top row and RICorDE in its calibrated form in the bottom row under the Fort McMurry town extent. Confusion matrix showcases the data points and respective categories across the entire Full domain.

A difference map, depicted in Figure 19, illustrates the elevation variances between the fast-response flood depth estimation tools and the calibrated HEC-RAS model depth. The analysis revealed significant differences in certain areas, characterized by abrupt and distinct transitions that were not readily apparent in the water depth maps. The differences can be visualized in Figure 19 as a clear change in elevation in the river cross-section of RICorDE. In both models, clear transitions can be observed along the river channel, representing the interpolation of the flooded boundary. The results suggest that inaccurate flooded depths arose from the interpolation of unrealistic flood boundary elevations, as indicated by red for underestimations and blue for overestimations along the difference map. Visually, it appears that FwDET outperformed RICorDE, as RICorDE exhibited a higher prevalence of difference outliers in flooded depths, particularly in the Clearwater River area. Conversely, FwDET tended to overestimate depths in the Athabasca River.

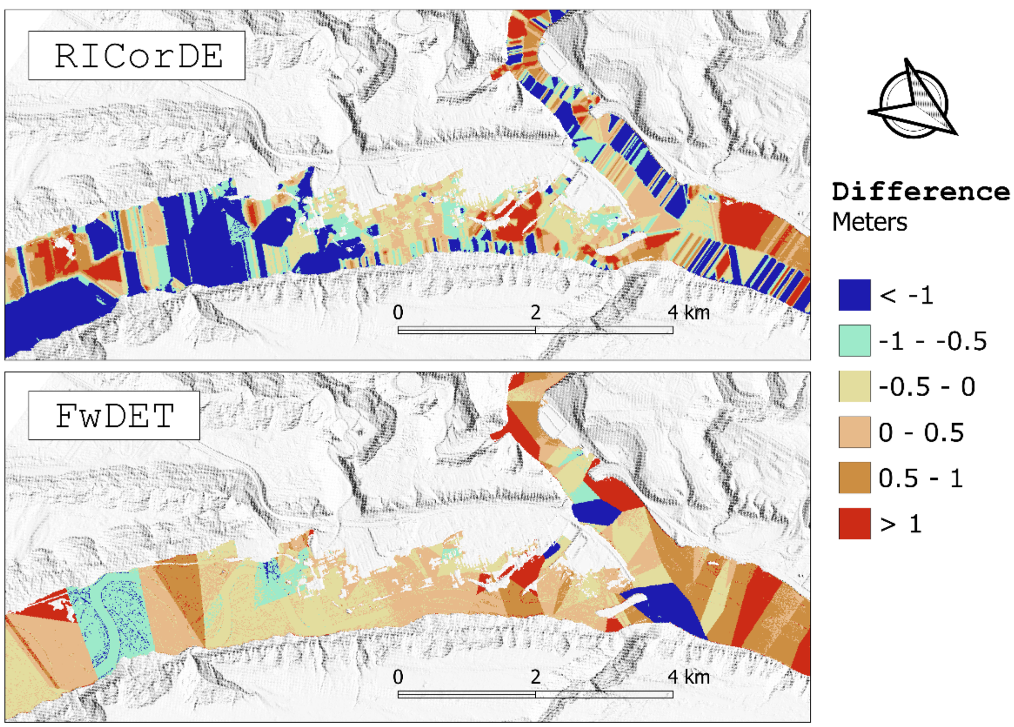

Figure 19. Difference in depth between the calibrated HEC-RAS depth on FwDET with a 3% slope filter and the user calibrated RICorDE model.

For the linear-regression correlation evaluation, the case study was segmented into three domains, as depicted in Figure 20abc. On the left side of Figure 20, the heatmap gridded depth of both RICorDE and FwDET are presented. In their default forms within the first and second rows and in their calibrated form in the third and forth row. Each heatmap panel displays metrics such as the Miss Rate, reflecting overlapped no data areas within the hand-drawn flood extent, as well as the coefficient of determination (R^2). On the right the domains presented are visualized. Results reveal that, in their calibrated form and under the bigger a)Full Extent domain, FwDET achieved a correlation between the modelled HEC-RAS depth and calibrated FwDET depth of 0.35 points higher (0.86 vs. 0.51) than its default form, while calibrated RICorDE achieved a correlation 0.14 points higher than its default form (0.69 vs. 0.55). Among the three evaluated domains, a higher correlation was obtained under the a)Full domain and the b)Clearwater River area. However, FwDET achieved higher flood depth similarities, more specifically 0.17 points higher than RICorDE under the Full domain and 0.10 points higher under the Fort McMurray town. Therefore, applying a slope filter in FwDET yielded a higher correlation than RICorDE in its calibrated form, particularly in case study extents that reports slope inclinations of up to 40°.

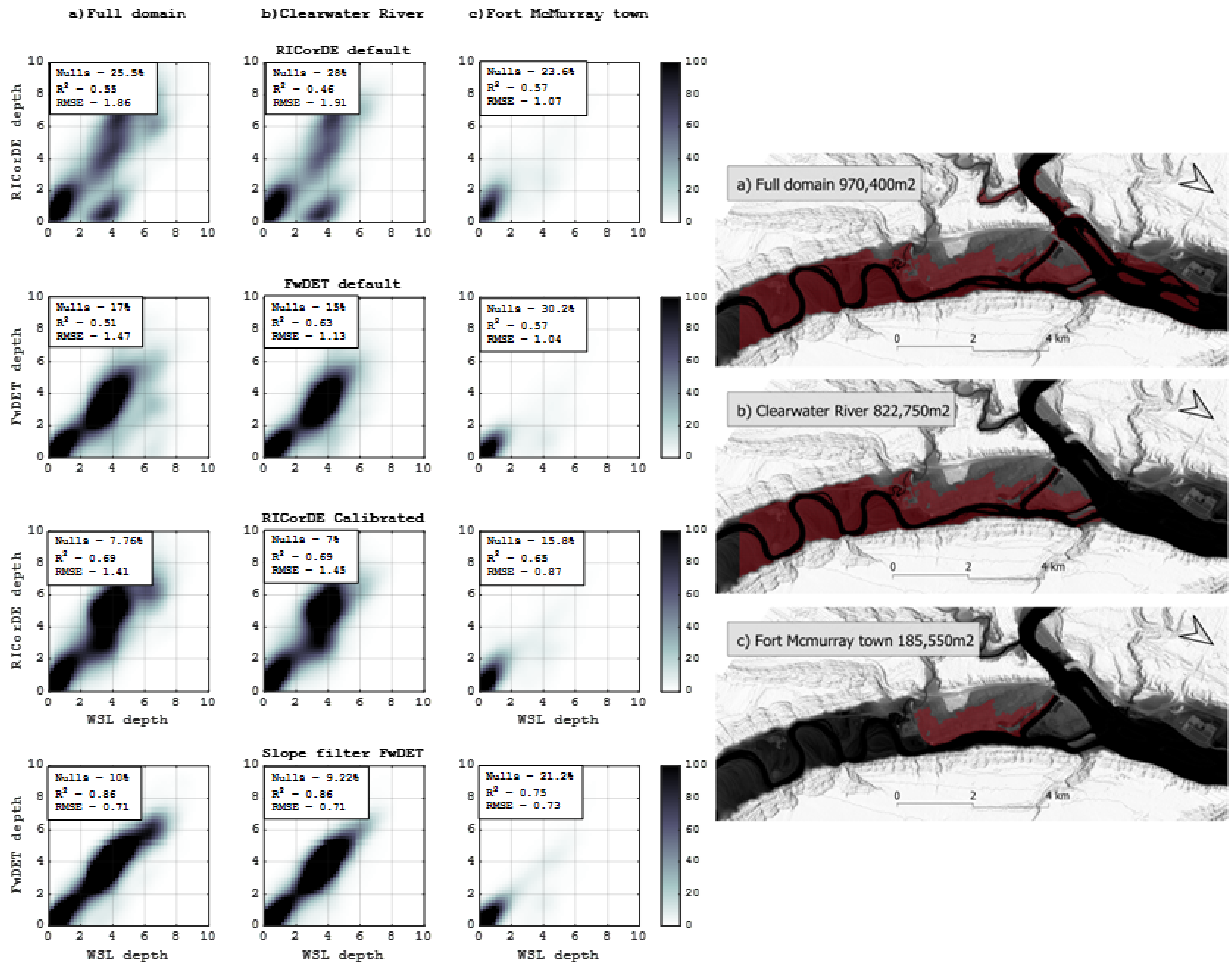

Figure 20. On the left, a Heatmap showcases the linear-regression correlation between the calibrated HEC-RAS model depth on the x-axis and depth values derived from hand-drawn extent data using FwDET and RICorDE on the y-axis. On the right, the domains are visually presented in red.

Figure 20 presents FwDET results against the case study DEM mentioned in Section 3.5.7. However, to assess whether a slope filter of FwDET v2.1 could yield positive results when implemented into RICorDE that operates under a HAND map instead of a DEM, a linear-regression comparison is presented in Figure 21 by using FwDET v2.1 with the HAND map as input. The HAND map used in this comparison defines drainage as a flow accumulation derived streamline. The results of this comparison revealed a linear correlation like the one attained with slope filtered

FwDET using a DEM, albeit with a slightly lower linear-regression correlation of 0.81, down by 0.05 points from its calibrated DEM iteration (Figure 20a).

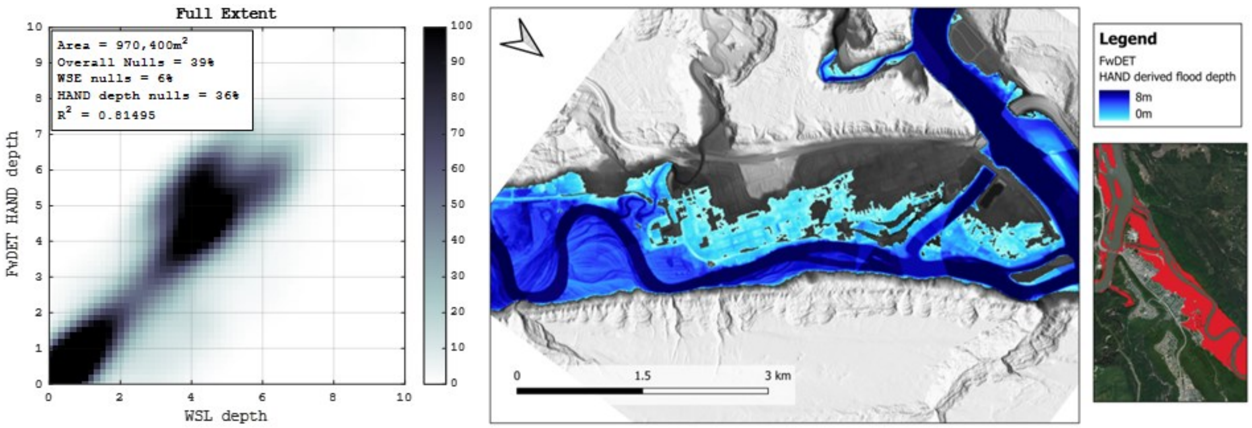

Figure 21. On the left: Heatmap linear-regression correlation between flood depths from the PCRaster toolbox derived HAND dataset on a slope threshold FwDET and the calibrated HEC-RAS WSL under the Full Extent. On the right: Flood depth map and minimap where the red area shows the "Full Extent" domain evaluated.

Similarly, RICorDE underwent testing utilizing the flow accumulation derived HAND map. Figure 22 presents the outcomes from the evaluation of RICorDE against an alternative HAND map, findings indicate a slightly lower correlation, registering at 0.66 points, 0.03 points less than the correlation achieved with the HAND map where drainage is defined at the water-land boundary (Figure 20a). Nevertheless, a slightly diminished RMSE was observed in this dataset, reaching 1.34 meters, which is 0.07 meters lower than its counterpart (Table 11).

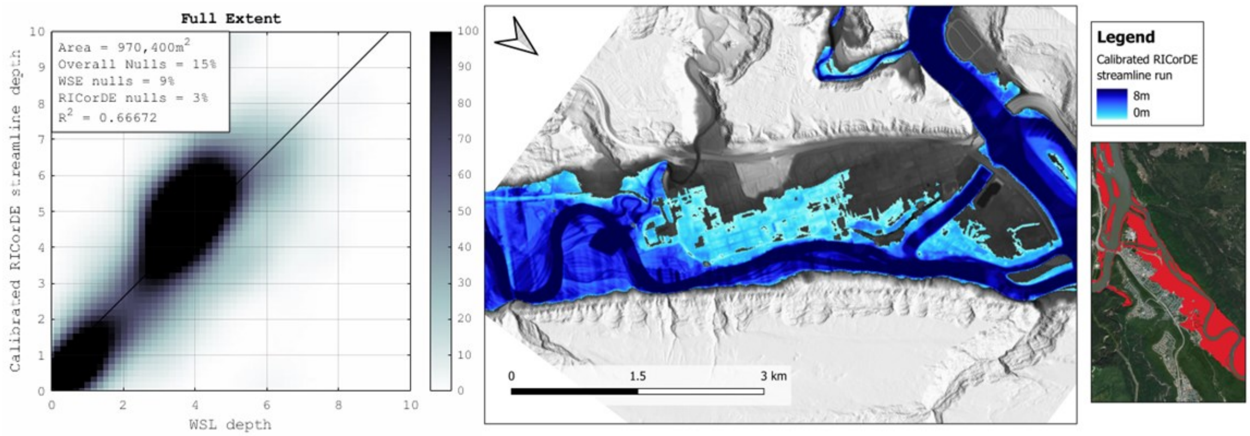

Figure 22. On the left: Heatmap linear-regression correlation between flood depths from a calibrated RICorDE run with a streamline instead of waterbodies and the calibrated HEC-RAS WSL under the Full Extent. On the right: Flood depth map and minimap where the red area shows the "Full Extent" domain evaluated.

Outliers were detected in both the non-calibrated and calibrated flood depth datasets. However, many outliers were not immediately noticeable in our linear regression correlations heatmap (Figure 20, 21, 22) due to the low count of data points. Additionally, Table 11 provides an additional perspective of the depths derived from RICorDE and FwDET, statistical measures from the presented figures are presented in Table 11. Interestingly, RICorDE achieved a RMSE of 1.41 points under the HIGH extent in its calibrated form and 1.34 points when utilizing an alternative HAND layer, indicating an improvement in performance with the flow accumulation-based HAND map. Additionally, the data suggests that RICorDE tended to overestimate the overall maximum depth, reaching a maximum of 12.54 in its calibrated form, compared to the HEC-RAS depth which achieved a maximum of 9.74. This discrepancy likely contributed to the overestimation of averaged measurements such as the mean value.

Table 11. Maximum elevation "Max", minimum elevation "Min", mean average elevation "AVG", standard deviation "SD", interquartile range "IQR" values, and RMSE for RICorDE, and FwDET against the HEC-RAS depth.

Extent	Layer	Max	Min	Mean (AVG)	Median	Standard Deviation (SD)	Interquartile Range (IQR)	RMSE
HIGH	WSL	9.74	0.01	3.30	3.47	1.85	2.74	
	RICorDE default	12.90	0.10	3.66	3.20	2.72	4.70	1.86
	RICorDE calibrated	12.54	0.00	3.82	3.99	2.30	3.82	1.41
	FwDET default	12.15	0.00	2.84	2.86	1.86	2.89	1.47
	FwDET 3% filter	9.21	0.00	3.22	3.42	1.87	3.09	0.71
MID	WSL	8.59	0.00	2.98	3.29	1.67	2.74	
	RICorDE default	11.60	0.10	3.24	2.40	2.58	4.40	1.91
	RICorDE calibrated	10.88	0.00	3.64	3.73	2.24	3.77	1.45
	FwDET default	10.11	0.00	2.81	2.86	1.82	2.88	1.13
	FwDET 3% filter	9.20	0.00	3.01	3.27	1.75	3.01	0.65
LOW	WSL	8.10	0.01	1.32	0.81	1.41	1.08	
	RICorDE default	9.60	0.10	1.67	1.30	1.47	1.60	1.07
	RICorDE calibrated	9.49	0.00	1.38	0.95	1.32	1.35	0.87
	FwDET default	8.47	0.00	1.02	0.73	1.11	0.90	1.04
	FwDET 3% filter	9.20	0.00	1.16	0.79	1.28	0.95	0.73
HIGH	RICorDE streamline	10.88	0.00	3.80	4.19	2.10	3.52	1.34
	FwDET HAND	9.77	0.00	3.19	3.45	2.15	4.06	0.92

Note: The statistical measures of elevation are distributed within the three designated domains presented in Figure 20.

The evaluation of cell elevation distribution in Figure 23 presents a smoothed average analysis, showcasing the histogram cell distribution for RICorDE and FwDET compared to the expected distribution of the calibrated HEC-RAS model depth. A Chi-Square Test was conducted to quantitatively assess the resulting distribution of cells; however, no significant relationship between the two distributions was found (Null hypothesis). Visual inspection of the results suggests a stronger similarity in the initial 1.5 meter distribution of cells. Beyond this threshold, a lower similarity is observed in the RICorDE dataset compared to FwDET, which exhibits a slightly higher similarity to the HEC-RAS depth. These discrepancies may arise from issues such as errors in flood extent delineation, DEM resampling or backscattering, or flood boundary filtering.

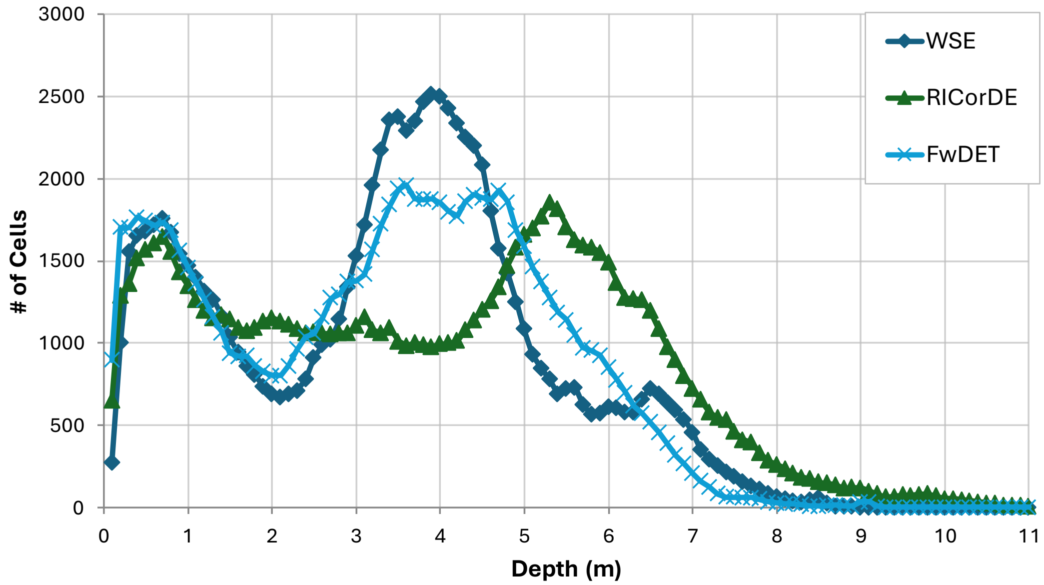

Figure 23. Cell distribution comparison between the HEC-RAS depth, RICorDE, and FwDET generated flood depth smoothed averages within the vicinity of Clearwater River leading to Fort McMurray town, excluding stream areas. The y-axis represents the number of cells, while the x-axis signifies the depth values.

To provide a clearer understanding of the variations in water surface elevation (WSE) across different topographies, a WSE profile is depicted on the left side of Figure 24. This profile illustrates depths obtained from fast response tools: green lines represent data from RICorDE, while yellow lines represent data from FwDET. Additionally, cyan lines indicate WSE values generated by the HEC-RAS model in the presented water surface profile plot. On the right side of the figure, the profile line is overlaid on the extent map of the case study area. Results suggest that FwDET yielded a flatter WSE profile line compared to RICorDE, indicating that the removal of high-slope outliers contributes to the smoothness of the water surface. Conversely, RICorDE exhibited clear and abrupt changes in WSE in areas such as the meandering river and near the confluence of the Clearwater River with the Athabasca River. These abrupt changes are hypothesized to be caused by the HAND map algorithm (with drainage at the water-land boundary) encountering challenges in depicting vertical elevations in sections where rivers are closely situated (meandering regions and conjunctions) because of flow direction depicting the vertical elevation reference point at sections of drainage with high sloping terrain along the water-land boundary.

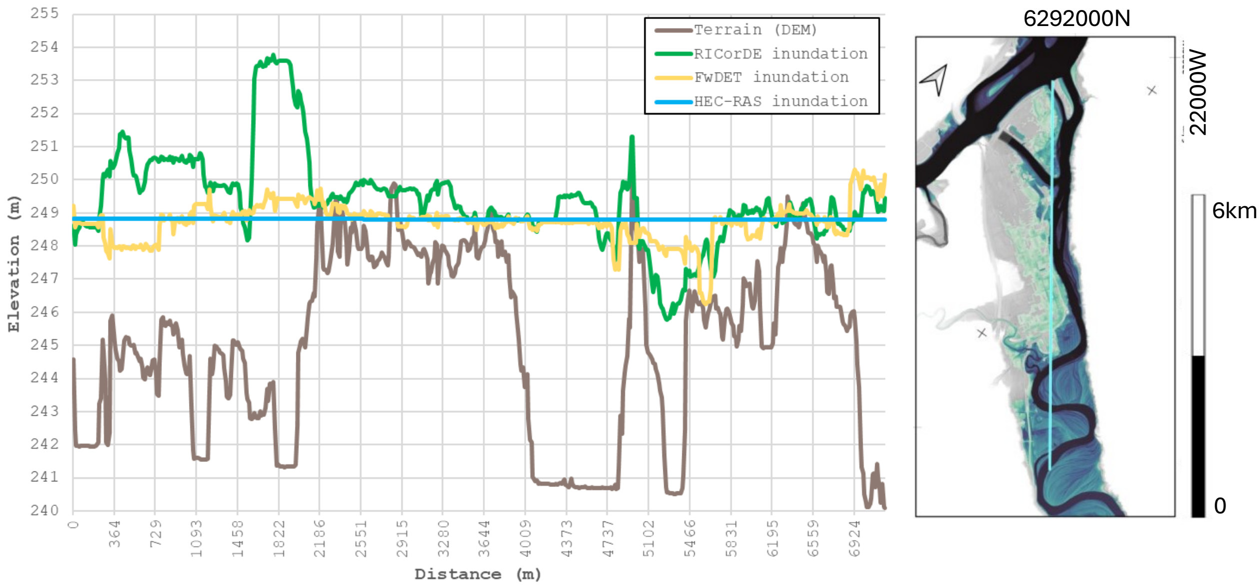

Figure 24. Water Surface Elevation (WSE) of the calibrated case study fast response tools as well as the HEC-RAS model depth presented in this thesis along the profile line in cyan.

5.3.2. High Water Mark differences

To assess the performance of RICorDE and FwDET in predicting depth, eight HWMs classified under the "above ground level" category were used. They were converted into depth values and then compared to the HWM data points. Figure 25 compares the resulting HWM depths and depth predicted by the fast-response tools as well as the case study HEC-RAS model depth. Regarding the point connection with the HWMs, the case study HEC-RAS model depth exhibited a point connection in 6 out of the 8 surveyed HWMs utilized in this analysis that depicted depth. In comparison, RICorDE and FwDET each displayed connections for 3 out of 8 points. In terms of correlation, the calibrated HEC-RAS model-derived depth showed an RMSE of 0.41m. RICorDE achieved an RMSE of 0.58m, while FwDET displayed an RMSE of 0.20m. It is important to acknowledge the potential bias in the RMSE assessment due to the scarcity of predicted depth data points connected with the HWMs. Additionally, the three data points connected by both RICorDE and FwDET are identical to those connected by the HEC-RAS modelled depth. Results suggest that the HEC-RAS model outperformed the fast response tools. However, it is hypothesised that the low point connection of both RICorDE and FwDET suggests possible discrepancies introduced during DEM resampling or erroneous delineation of flood extent.

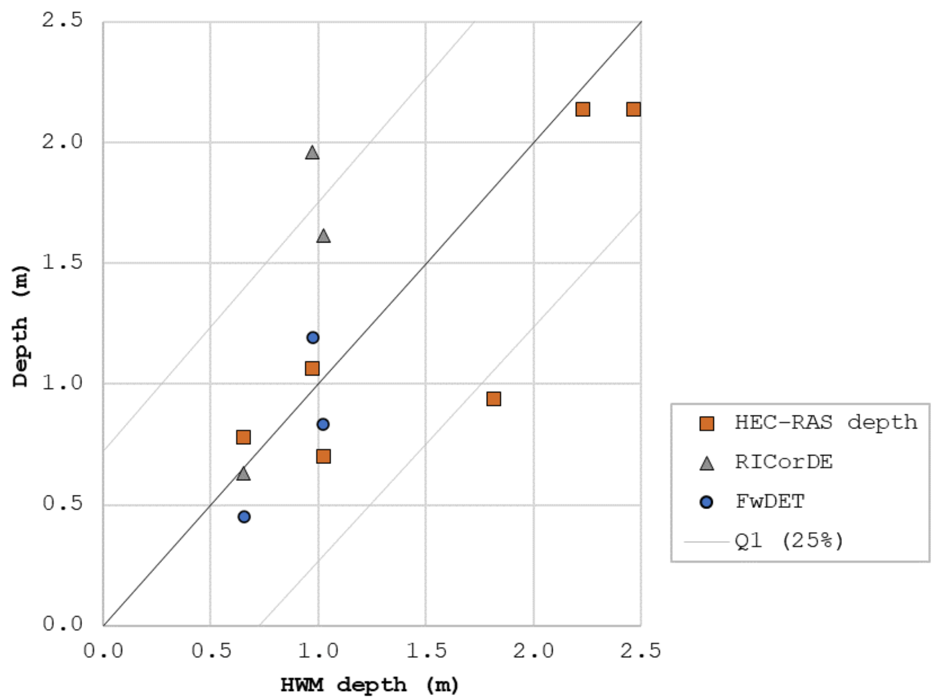

Figure 25. The x-axis HWM depth include the calibrated HEC-RAS modelled depth denoted by squares, the calibrated RICorDE depth represented by triangles, and the depth data obtained from FwDET with a 3% slope filtering applied, visualized as circles.

A more detailed description of the presented data is found in Table 12 where each data points is listed and described. Table 12 values suggest that both RICorDE and FwDET successfully predicted floods under silt line HWMs in urban areas (#51, 52, 62), but not in vegetation-covered areas such as under trees (#66, 67). This discrepancy could be attributed to scattering effects on forest areas and DEM resampling (Tretyak et al., 2021). For the remaining HWMs where predictions were inaccurate, no clear reason was identified, although it is suspected that flood extent delineation may have contributed to the missing data points.

Table 12. High water marks used for the HWM gridded depth comparison.

#	Site	Latitude (NAD83)	Longitude (NAD83)	Elevation(m) (CGVD28)	CGVD28 - epoch2011	H2013	HWM Category	HWM Description	DEM (m)	HWM depth	RICorDE	FwDET3%	WSE
41	CLR5D-1	56.74403	-111.387	248.877	248.895	248.859	above ground	Silt line on rock	248.65	0.21	N/A	N/A	N/A
51	CLR5D-6	56.7123	-111.345	248.92	248.93	248.90		Silt line on playground slide	247.93	0.97	1.96	1.19	1.07
52	CLR5D-6	56.7127	-111.345	248.91	248.92	248.89		Silt line on garbage can (no rod)	247.87	1.02	1.62	0.83	0.70
59	CLR5D-10	56.69443	-111.331	248.875	248.893	248.871		Wash line on barricades	248.78	0.09	N/A	N/A	N/A
61	CLR5D-12	56.6847	-111.302	248.91	248.92	248.91		Debris line on top of wooden fence	247.09	1.82	N/A	N/A	0.94
62	CLR5D-13	56.6768	-111.255	248.95	248.96	248.95		Silt wash line on solitary iron loader bucket	248.30	0.65	0.63	0.45	0.78
66	CLR5D-15	56.672	-111.232	249.04	249.06	249.05		Brown high water line on tree trunk	246.82	2.23	N/A	N/A	2.14
67	CLR5D-15	56.672	-111.232	249.05	249.07	249.06		Brown high water line on tree trunk	246.60	2.46	N/A	N/A	2.14

6. Conclusion

The performance of two fast flood depth estimation tools, RICorDE and FwDET, was evaluated for the Fort McMurray 2020 ice jam flood event. Results were compared against HWM values and a case study HEC-RAS hydrodynamic model. RICorDE is dependant on hydro-correction as well as HAND map generation techniques for its flood depth computations; therefore, we conducted an in-depth examination of depressions and HAND maps. Additionally, we explored the generation of flood extent maps using HAND maps and surveyed HWMs. The conclusions presented in this section encapsulate the findings and implications of our research, highlighting significant discoveries and suggesting potential future directions.

6.1. Conclusion on fast response flood depth estimation tools

Implementing rapid-response SAR-based flood depth estimations under the ice jam flood events in Fort McMurray using RICorDE and FwDET presents challenges. The area topography, comprising flat and gently rolling terrain with some low hills, hinders the generation of a WSL under default tool conditions due to sloping formations along the river water-land and flood boundaries. However, under altered configurations, both tools can address complications caused by sloping formations along the river with distinct methodologies. For example, RICorDE generates a dynamic flood surface by statistically filtering outliers, utilizes a HAND map as an inundation proxy, and incorporates a wide range of parameters and potential algorithmic adjustments(Bryant et al., 2022). On the other hand, FwDET generates a static flood surface, averages the boundary values, and removes hilly elevations from the flood boundaries, resulting in a smoother surface.

RICorDE v1.0.1 performance during ice jam flood events suggests it may not be suitable for meandering rivers and areas with prominent steepness, although it has performed satisfactorily under pluvial, coastal, and riverine flooding case studies. In conclusion, areas with sloping terrain and close river networks, expecting a flat WSL, may benefit from FwDET v2.1. Conversely, in areas anticipating a dynamic

WSL, such as coastal regions, RICorDE v1.0.1 is preferred. Employing low-input data approaches for flood depth or extent mapping proves valuable for swift response, provided accurate flood extent information and high-quality DEM data are available.

- In flood depth estimations, simpler models like RICorDE and FwDET benefit from lower data requirements and computational intensity. Conversely, more complex physics-based models such as MIKE FLOOD, HEC-RAS, SWAT, and TOPMODEL are expected to provide more precise estimates due to their construction of a hydro-system using fundamental mathematical representations and the principles of mass and momentum conservation (Nguyen et al., 2024). However, the development of these models entails gathering comprehensive site data, including topography, meteorological information, hydrological data series, and soil properties, which can be costly and time-consuming (Nguyen et al., 2024).
- Integrating ice jam dynamics into flood modelling introduces significant complexity, as it involves considering factors like ice formation, accumulation, initiation, movement, and hydraulic effects. Each of these elements introduces additional variables and considerations that must be carefully addressed in the modelling process. However, data-reliant models such as RICorDE and FwDET offer an alternative approach, providing depth estimations with R^2 correlations to a HEC-RAS model of up to 0.86 with reduced data requirements. These models, while efficient, do not account for the complexities of ice dynamics, highlighting a trade-off between model complexity and data dependency in flood depth estimation.
- In terms of performance using their default configurations, both FwDET and RICorDE demonstrated similar performance. However, RICorDE achieved a slightly higher correlation than FwDET under their default settings during the case study event, with a difference of 0.04 points. Interestingly, upon calibration, FwDET surpassed RICorDE with a correlation that was 0.17 points higher.
- Regarding parameters, RICorDE v1.0.1 offers a greater number of parameters and increased flexibility, allowing developers to interact with QGIS functionality using Python scripts. This enhanced flexibility provides advantages but also necessitates a higher level of expertise and, depending on the case study, more adjustments from users. Furthermore, users may discover that modifying

RICorDE parameters does not always result in immediately visible changes. For instance, adjusting the parameter "qhigh" may alter the dataset, but these changes might not be immediately apparent. For this study, the calibration criterion of RICorDE was extent, and calibrating to maximize the case study flooded polygon resulted in a higher number of valid flood targets. In comparison, the setup and calibration process of QGIS FwDET v2.1 consisted of a low number of iterations of the slope filter until the desired flood extent delineation was achieved.

- In terms of computational time, although not quantitatively measured, the processing time of FwDET was lower than RICorDE due to the integration of a higher number of sub-processes in the latter. It is important to note that this difference was in seconds since the case study file size was relatively low (around 20 megabytes).

6.2. Conclusion on Hydro-Correction method

Numerous depression filling algorithms from the WBT provider were examined, with little observed quantitative differences in their results. More specifically, minimal discrepancies in terms of the total number of altered cells, in the cumulative elevation changes, and in the number of cells hydro-connected to the water-land boundary. Similarly, breaching methodologies achieved similar results to the filling methodologies

- The quantitative assessment suggests that the hydro-correction methodology produced consistent results in terms of stream hydro-connection. Differences were only encountered in stream burn methodologies and the simple fill single cell pits. Although results suggest a low number of differences between the hydro-correction methods it is important to mention that changes in flow direction were not quantitatively evaluated in this study. It is hypothesised that fill depression methodologies will result in the same flow direction, however differences may be expected under the breach depression methodologies.
- In terms of computational time, only seconds of differences were observed between the methods. However, it is important to mention that the case study

dataset had low computational demand (package of 20 megabytes). On smaller DEM resolutions and larger extents, changing the hydro-correction method could result in substantial decreases in computational time. For example, there was a 3.1 times reduction in time when comparing Wang and Liu (2006) to Planchon and Darboux (2001). Therefore, I recommend utilizing the FillDepression or Wang and Liu (2006) depression fixing algorithm from the WBT provider.

- The depression breaching methodology was not utilized because during RICorDE flood depth computations using the depression breaching approach, downtown Fort McMurray was inaccurately represented as not inundated. The exact cause of these gaps in the flood depth raster when utilizing the BreachDepressionLeastCost method remains unclear. However, it is hypothesized that these issues may be attributed to changes in flow direction. Finally, switching the hydro-correction method to fill depression effectively addressed the issue of areas incorrectly depicted as not flooded in the RICorDE case study flood depth analysis.

6.3. Conclusion on Height Above Nearest Drainage map

Two HAND maps were evaluated, each employing a different definition of drainage point. One defined drainage as streamlines where the highest volume of water drains, while the other considered the observed water-land boundary of the river or waterbody. The quantitative assessment of HAND maps revealed that the choice of drainage influences HAND values and their potential in delineating flood maps and depth. Notably, generating flood extent maps with HAND maps that establish drainage at the water-land boundary resulted in a higher number of miss predictions of delineated extent compared to the streamline approach. Due to the higher number of falsely depicted flooded areas under the water-land boundary HAND map and depending on the topography of the case study area, establishing drainage from a flow accumulation algorithm or the river thalweg could lead to a more accurate depiction of the extent.

In terms of topography, it is hypothesized that slopes along the water-land boundary may result in significant elevation variations on the HAND map, leading to an increased number of falsely depicted flooded areas. It is suggested that the false depiction of flooded extent is particularly influenced by neighboring high-slope cells adjacent to the water-land boundary that are not corrected by the depression fixing algorithm. Additionally, in the terrain of Fort McMurray, the Clearwater River follows a lengthy, meandering path with closely connected streams, potentially impacting the reliability of HAND map that define drainage at the water-land boundary in similar topographies.

In terms of flow direction, users generating HAND maps have the option to select between the D8 and D-INF flow direction algorithms to determine the drainage point corresponding to the gridded HAND value. While the literature often favors the D-INF approach for generating HAND maps, quantitative differences between the D8 and D-INF algorithms were not assessed in the case study of the 10-meter DEM. Ultimately, the D8 approach was selected for this study due to its simplicity and compatibility with the evaluated HAND map generation algorithms.

In summary, the choice between the water-land boundary and streamline approaches depends on factors such as topography, analysis type, and available survey data. While utilizing HAND maps for flood extent delineation offers benefits, further studies assessing their performance across various topographies are necessary to determine if their effectiveness is influenced by specific terrain characteristics. For example, the lack of sloping terrain and meandering rivers could result in different outcomes. It would be advisable for further studies to determine if defining drainage at the water-land boundary under flatter terrain would result in a higher correlation of depth and extent. Additionally, evaluating if utilizing the D-INF flow direction algorithm under HAND maps of lower resolution increases their validity would be beneficial.

6.4. Limitations on data availability for the Fort McMurray 2020 flood

Limitations were present in the overall case study, mostly related to the availability of flood event data, resolution chosen for the rapid response flood depth estimations, and assessment of flow direction alterations for the evaluation of hydro-correction techniques. These are presented as bullet points below:

- During the flood event in the Fort McMurray area, discharge and level data exhibited numerous gaps across three stations, particularly coinciding with the flood occurrence. This phenomenon is common in river ice operations, as floating ice can damage gauge stations and disrupt data collection methods. Additionally, the publicly available flood extent layer was considered unreliable when compared to flood event imagery, prompting the creation and utilization of a hand-drawn flood extent overlaying aerial imagery. However, it is possible that previously left-behind remnant ice or shear walls along the river bluffs could have been inaccurately interpreted as flooded areas during manual delineation, potentially leading to minor misinterpretations in flood extent delineation and in turn depth estimations.
- Like any other form of data analysis, flood depth modelling is subject to limitations, as the accuracy of its outputs is contingent upon the quality of its inputs. Furthermore, existing literature has noted that resolution can influence the effectiveness of rapid response flood depth modelling. However, this study did not quantitatively assess the impact of DEM resolution on flood depth estimations.

6.5. Recommendations and future direction

In terms of flood depth estimations:

- Results obtained from FwDET indicate that incorporating a slope filter leads to a notable improvement in performance, increasing correlation by 0.35 R^2 points. Integrating a slope filter into future iterations of RICorDE could enhance the accuracy of its depth estimations, especially in areas characterized by steep terrain. However, it remains uncertain whether the methodologies employed in RICorDE would seamlessly accommodate the application of a slope filter to its flood boundaries.
- The adjustment in HAND map generation methodology appeared to have an impact of -0.03 R^2 points on the performance of flood extent delineation and flood depth estimation. However, it is important to mention that a HAND map generated via a flow accumulation streamline did not require prior delineation of the waterbodies resulting beneficial for fast response. Additionally, given the significance of drainage it is advised to meticulously delineate the waterbodies to enhance their accuracy under the water-land boundary method.
- To broaden the accessibility of RICorDE and make it more user-friendly, several strategies can be considered. Firstly, enhancing compatibility with popular platforms like Google Earth Engine and ArcGIS would extend its usability to a wider audience. Additionally, developing a user-friendly interface for RICorDE could facilitate easier navigation and utilization of its features. Furthermore, altering the methods of RICorDE to slightly different alternatives to seamlessly integrate as a QGIS plugin would cater to users looking for a more straightforward approach or individuals lacking programming skills, thereby democratizing access to the tool.

In terms of hydro-correction and HAND maps:

- When applied for flood depth estimations, study findings indicate that filling method of hydro-correction was the preferred method when generating HAND maps, principally because breaching methodologies were not entirely compatible with the RICorDE model under the case study extent, which resulted in notable gaps of the flooded domain extent.

- The quantitative impact of flow direction algorithms on HAND maps was not measured in this study. While literature suggests that the D-INF algorithm may outperform the D8 algorithm, it is hypothesized that changes in elevation along the HAND map resulting from alterations in flow direction methods would be minimal, especially considering the extent and resolution of the case study dataset. However, it is likely that switching between breaching and filling depression-fixing methods could induce changes in the HAND dataset. This study did not directly assess the modifications incurred by the HAND dataset when altering flow direction or hydro-correction techniques. Future research could investigate the effects of switching between breaching and filling methods, as well as between D8 and D-INF algorithms, on the HAND dataset.

Finally, conducting a comprehensive assessment of RICorDE and FwDET may not be entirely equitable, given that RICorDE is still in its nascent stages. There remains substantial potential for further optimization and adaptation, including exploring possible variations in its methodology, expanding RICorDE to additional platforms such as ArcGIS and Google Earth Engine, and developing a dedicated QGIS plugin for its seamless integration.

Bibliography

Adriano, L. 2021. Fort McMurray to spend $10 million on flood mitigation. Insurance Business Canada. April 19, 2021. From https://www.insurancebusinessmag.com/ca/news/flood/fortmcmurray-to-spend-10-million-on-flood-mitigation-252601.aspx [Accessed June 1, 2021].

Airborne Imaging. (2017). LiDAR acquisition and Processing (Report No. 13797_AEP_FortMcMurray).

Amitrano, D., Di Martino, G., Guida, R., Iervolino, P., Iodice, A., Papa, M. N., ... & Ruello, G. (2021). Earth environmental monitoring using multi-temporal synthetic aperture radar: A critical review of selected applications. *Remote Sensing*, *13*(4), 604.

Aristizabal, F., Salas, F., Petrochenkov, G., Grout, T., Avant, B., Bates, B., ... & Judge, J. (2022). Extending Height Above Nearest Drainage to Model Multiple Fluvial Sources in Flood Inundation Mapping Applications for the US National Water Model. *Water Resources Research*, e2022WR032039.

Australian Bureau of Statistics. (2024). Measures of spread. Retrieved from https://www.abs.gov.au/statistics/understanding-statistics/statistical-terms-and-concepts/measures-spread

Azizat, N. (2018, March). Spatial and temporal flood risk assessment for decision making approach. In IOP Conference Series: Materials Science and Engineering (Vol. 318, No. 1, p. 012022). IOP Publishing.

Ballocci, M., Molinari, D., Ballio, F., & Marin, G. (2023). *Econometric modelling for the estimation of direct flood damage to enterprises: a local-scale approach from post-event records in Italy* (No. EGU23-11320). Copernicus Meetings.

Band, L. E. (1986). Topographic partition of watersheds with digital elevation models. *Water resources research*, *22*(1), 15-24.

Barber, C. P., & Shortridge, A. (2005). Lidar elevation data for surface hydrologic modeling: Resolution and representation issues. *Cartography and Geographic Information Science*, *32*(4), 401-410.

Barnes, R. (2018). *RichDEM: High-performance terrain analysis* (No. e27099v1). PeerJ Preprints.

Barnes, R., Lehman, C., & Mulla, D. (2014). Priority-flood: An optimal depression-filling and watershed-labeling algorithm for digital elevation models. *Computers & Geosciences*, *62*, 117-127.

Beltaos, S. (2008). Progress in the study and management of river ice jams. *Cold regions science and technology*, *51*(1), 2-19.

Beltaos, S. (2010, June). Assessing ice-jam flood risk: Methodology and limitations. In *Proceedings of the 20th IAHR International Symposium on Ice, Lathi, Finland* (pp. 14-17).

Beltaos, S. (2014). Hydrodynamic properties of ice-jam release waves in the Mackenzie Delta, Canada. *Cold regions science and technology*, *103*, 91-106.

Benke, A. C., & Cushing, C. E. (Eds.). (2011). *Rivers of North America*. Elsevier.

Bogaart, P.W., and Troch, P.A., Curvature distribution within hillslopes and catchments and its effect on the hydrological response. Hydrology and Earth System Sciences 10, 925-936 (2006).

Bonsal B.R., Prowse T.D., Duguay C.R., and Lacroix M.P. 2006. Impacts of large-scale teleconnections on freshwater-ice break/freeze-up dates over Canada. J. Hydrol. 330(1): 340–353.

Borshch S.V., Ginzburg B.M., and Soldatova I.I. 2001. Modeling the development of ice phenomena in rivers as applied to the assessment of probable changes in ice conditions at various scenarios of the future climate. Water Resources, 28(2): 194–200.

Bryant, S., McGrath, H., & Boudreault, M. (2022). Gridded flood depth estimates from satellite-derived inundations. *Natural Hazards and Earth System Sciences*, *22*(4), 1437-1450.

Bryant, S., Schumann, G., Apel, H., Kreibich, H., & Merz, B. (2023). Resolution enhancement of flood inundation grids. *Hydrology and Earth System Sciences Discussions*, *2023*, 1-18.

Catastrophe Indices and Quantification Inc. (n.d.). Flood category. CatIQ. https://public.catiq.com/blog_category/flood/

Chang, S., Singh Wilkho, R., Gharaibeh, N., Lyle, S., & Zou, L. (2023). Predicting Flash Flood Economic Damage at the Community Scale: Empirical Zero-Inflated Model with Semicontinuous Data. *Natural Hazards Review*, *24*(4), 04023030.

Cian, F., Marconcini, M., Ceccato, P., & Giupponi, C. (2018). Flood depth estimation by means of high-resolution SAR images and lidar data. *Natural Hazards and Earth System Sciences*, *18*(11), 3063-3084.

Cohen, S., Brakenridge, G. R., Kettner, A., Bates, B., Nelson, J., McDonald, R., ... & Zhang, J. (2018). Estimating floodwater depths from flood inundation maps and topography. *JAWRA Journal of the American Water Resources Association*, *54*(4), 847-858.

Cohen, S., Peter, B. G., Haag, A., Munasinghe, D., Moragoda, N., Narayanan, A., & May, S. (2022). Sensitivity of Remote Sensing Floodwater Depth Calculation to Boundary Filtering and Digital Elevation Model Selections. *Remote Sensing*, *14*(21), 5313.

Cohen, S., Raney, A., Munasinghe, D., Loftis, J. D., Molthan, A., Bell, J., ... & Tsang, Y. P. (2019). The Floodwater Depth Estimation Tool (FwDET v2. 0) for improved remote sensing analysis of coastal flooding. *Natural Hazards and Earth System Sciences*, *19*(9), 2053-2065.

Confusion matrix. (n.d.). In *GIS Wiki*. https://wiki.gis.com/wiki/index.php/Confusion_matrix

Contrib, C. (2023). FwDET. GitHub. https://github.com/csdms-contrib/fwdet/tree/master/qgis

Crown, P. H., & Twardy, A. G. (1975). Soils of the Fort McMurray Region, Alberta (Townships 88-89, Ranges 8-11) and Their Relation to Agricultural and Urban Development. University of Alberta.Czuba, J. A., & Foufoula-Georgiou, E. (2015). Dynamic connectivity in a fluvial network for identifying hotspots of geomorphic change. *Water Resources Research*, *51*(3), 1401-1421.

Daniel, C. D., Costache, R., & Popa, M. C. (2021). An Overview of Flood Risk Analysis Methods. Water, 13(4), 474. https://doi.org/10.3390/W13040474

Das, A., & Lindenschmidt, K. E. (2020). Current status and advancement suggestions of ice-jam flood hazard and risk assessment. *Environmental Reviews*, *28*(4), 373-379.

Das, A., & Lindenschmidt, K. E. (2021). Modelling climatic impacts on ice-jam floods: a review of current models, modelling capabilities, challenges, and future prospects. Environmental Reviews, 29(3), 378-390.

Das, A., & Lindenschmidt, K. E. (2021). Modelling climatic impacts on ice-jam floods: a review of current models, modelling capabilities, challenges, and future prospects. *Environmental Reviews*, *29*(3), 378-390.

De Coste, M., Li, Z., Pupek, D., & Sun, W. (2021). A hybrid ensemble modelling framework for the prediction of breakup ice jams on Northern Canadian Rivers. *Cold Regions Science and Technology*, *189*, 103302.

Donchyts, G., Winsemius, H., Schellekens, J., Erickson, T., Gao, H., Savenije, H., & van de Giesen, N. (2016). Global 30m height above the nearest drainage. HAND, 1000(0).

Elkhrachy, I. (2022). Flash flood water depth estimation using SAR images, digital elevation models, and machine learning algorithms. *Remote Sensing*, *14*(3), 440.

Emmer, S., Kovachis Watson, N., & Nafziger, J. (2021, August). A Tale of Two Basins: The 2020 river ice breakup in northern Alberta, Part II: The Peace River. In *CGU HS Committee on River Ice Processes and the Environment 21st Workshop on the Hydraulics of Ice Covered Rivers*.

Endendijk, T., Botzen, W. W., de Moel, H., Aerts, J. C., Slager, K., & Kok, M. (2023). Flood vulnerability models and household flood damage mitigation measures: An econometric analysis of survey data. *Water Resources Research*, *59*(8), e2022WR034192.

Fairfield, J., & Leymarie, P. (1991). Drainage networks from grid digital elevation models. *Water resources research*, *27*(5), 709-717.

Federal Emergency Management Agency. (2020, October 23). Hazus User Technical Manuals. FEMA. https://www.fema.gov/flood-maps/tools-resources/flood-map-products/hazus/user-technical-manuals

Federal Emergency Management Agency. (2021, March 18). Safeguard your future with flood insurance. Retrieved from https://www.fema.gov/press-release/20210318/safeguard-your-future-flood-insurance

Federal Emergency Management Agency. (2024). Flood maps. Retrieved from https://www.fema.gov/flood-maps

Fohringer, J., Dransch, D., Kreibich, H., & Schröter, K. (2015). Social media as an information source for rapid flood inundation mapping. *Natural Hazards and Earth System Sciences*, *15*(12), 2725-2738.

French, H. M. (2017). *The periglacial environment*. John Wiley & Sons.

Giordan, D., Notti, D., Villa, A., Zucca, F., Calò, F., Pepe, A., ... & Allasia, P. (2018). Low cost, multiscale and multi-sensor application for flooded area mapping. *Natural Hazards and Earth System Sciences*, *18*(5), 1493-1516.

Government of Canada. (2022). TRX [Web application]. Retrieved from https://webapp.csrs-scrs.nrcan-rncan.gc.ca/geod/tools-outils/trx.php

Government of Canada. (2023a). National Adaptation Strategy: Action Plan. Retrieved from https://www.canada.ca/en/services/environment/weather/climatechange/climate-plan/national-adaptation-strategy/action-plan.html

Government of Canada. (2023b). Flood Risk Areas. Open Government, Government of Canada. https://open.canada.ca/data/en/dataset/74144824-206e-4cea-9fb9-72925a128189 (Accessed May 01, 2023).

Government of Canada. (2023c). Geodetic Surveyor's Handbook (GPS·H) [Website]. Retrieved from webapp.csrs-scrs.nrcan-rncan.gc.ca/geod/tools-outils/gpsh.php

Groeneveld, J., & Zare, S. (2022). Ice Jam Flooding in the Athabasca River at Fort McMurray – Validation of a Previously Developed Model to the 2020 Ice Jam Event. Retrieved from https://www.iahr.org/library/infor?pid=22121

Hao, C., Yunus, A. P., Subramanian, S. S., & Avtar, R. (2021). Basin-wide flood depth and exposure mapping from SAR images and machine learning models. *Journal of Environmental Management*, *297*, 113367.

Hatch and Golder Associates. 2021. Ice Jam Modelling and Flood Hazard Identification Report (from the Fort McMurray Flood Hazard Study). Prepared for Alberta Environment and Parks. Appendix G. Forthcoming

Heine, R. A., Lant, C. L., & Sengupta, R. R. (2004). Development and comparison of approaches for automated mapping of stream channel networks. *Annals of the Association of American Geographers*, *94*(3), 477-490.

Hicks, F. E. (2016). *An introduction to river ice engineering for civil engineers and geoscientists*. CreateSpace Independent Publishing Platform.

Hutchison, T. K., & Hicks, F. E. (2007). Observations of ice jam release waves on the Athabasca River near Fort McMurray, Alberta. *Canadian Journal of Civil Engineering*, *34*(4), 473-484.

Insurance Bureau of Canada. (n.d.). Severe weather in 2023 caused over $3.1 billion in insured damage. https://www.ibc.ca/news-insights/news/severe-weather-in-2023-caused-over-3-1-billion-in-insured-damage

Intergovernmental Panel on Climate Change. (2022). Summary for policymakers. In Climate Change 2022: Impacts, Adaptation, and Vulnerability. Contribution of Working Group II to the Sixth Assessment Report of the Intergovernmental

Panel on Climate Change. Retrieved from https://www.ipcc.ch/report/ar6/wg2/downloads/report/IPCC_AR6_WGII_SummaryForPolicymakers.pdf

Jenson, S.K. and Domingue, J.O. "Extracting Topographic Structure from Digital Elevation Data for Geographic Information System Analysis". Photogrammetric Engineering and Remote Sensing, Vol. 54, No. 11, November 1988, pp. 1593-1600.

Karssenberg, D., Schmitz, O., Salamon, P., de Jong, K., and Bierkens, M. F. P.: A software framework for construction of process-based stochastic spatio-temporal models and data assimilation, Environmental Modelling & Software 25(4), 489-502, 2010. doi: 10.1016/j.envsoft.2009.10.004.

Kharazi, B. A., & Behzadan, A. H. (2021). Flood depth mapping in street photos with image processing and deep neural networks. *Computers, Environment and Urban Systems*, *88*, 101628.

L.C. Smith, "Satellite remote sensing of river inundation area, stage, and discharge: a review," Hydrological Processes, 11(10), pp. 1427-1439, 1997.

Lindenschmidt, K. E., Huokuna, M., Burrell, B. C., & Beltaos, S. (2018). Lessons learned from past ice-jam floods concerning the challenges of flood mapping. International Journal of River Basin Management, 16(4), 457-468.

Lindenschmidt, K. E., Rokaya, P., Das, A., Li, Z., & Richard, D. (2019). A novel stochastic modelling approach for operational real-time ice-jam flood forecasting. *Journal of Hydrology*, *575*, 381-394.

Lindsay J, Dhun K. 2015. Modelling surface drainage patterns in altered landscapes using LiDAR. International Journal of Geographical Information Science, 29: 1-15. DOI: 10.1080/13658816.2014.975715

Lindsay, J. B. (2014, April). The whitebox geospatial analysis tools project and open-access GIS. In Proceedings of the GIS Research UK 22nd Annual Conference, The University of Glasgow (pp. 16-18).

Lindsay, J. B. (2016). Efficient hybrid breaching-filling sink removal methods for flow path enforcement in digital elevation models. *Hydrological Processes*, *30*(6), 846-857.

Lindsay, J. B., & Creed, I. F. (2005). Removal of artifact depressions from digital elevation models: towards a minimum impact approach. *Hydrological Processes: An International Journal*, *19*(16), 3113-3126.

Lindsay, J. B., & Creed, I. F. (2006). Distinguishing actual and artefact depressions in digital elevation data. *Computers & Geosciences*, *32*(8), 1192-1204.

Liu, Y. Y., Maidment, D. R., Tarboton, D. G., Zheng, X., Yildirim, A., Sazib, N. S., & Wang, S. (2016). A CyberGIS approach to generating high-resolution height above nearest drainage (HAND) raster for national flood mapping.

Madaeni, F., Lhissou, R., Chokmani, K., Raymond, S., & Gauthier, Y. (2020). Ice jam formation, breakup and prediction methods based on hydroclimatic data using artificial intelligence: A review. Cold Regions Science and Technology, 174, 103032.

Magalhães, S. V., Andrade, M. V., Randolph Franklin, W., & Pena, G. C. (2012). A new method for computing the drainage network based on raising the level of an ocean surrounding the terrain. In *Bridging the Geographic Information Sciences: International AGILE'2012 Conference, Avignon (France), April, 24-27, 2012* (pp. 391-407). Springer Berlin Heidelberg.

Maidment, D. R., & Djokic, D. (Eds.). (2000). Hydrologic and hydraulic modeling support: with geographic information systems. ESRI, Inc..

Marks, D., Dozier, J., & Frew, J. (1989). Automated basin delineation from digital elevation data, Geo-proc., 2. pp. 299–311.

Martello, M. V., Whittle, A. J., & Lyons-Galante, H. R. (2023). Depth-damage curves for rail rapid transit infrastructure. *Journal of Flood Risk Management*, *16*(1), e12856.

Martz, L. W., and J. Garbrecht.1998."The Treatment of Flat Areas and Depressions in Automated Drainage Analysis of Raster Digital Elevation Models."Hydrological Processes12:843–855. doi:10.1002/(ISSN)1099-1085.

Martz, L. W., and J. Garbrecht.1999."An Outlet Breaching Algorithm for the Treatment of Closed Depressions inaRaster DEM."Computers & Geosciences25: 835–844.doi:10.1016/S0098-3004(99)00018-7.

Matgen, P., Giustarini, L., Chini, M., Hostache, R., Wood, M., & Schlaffer, S. (2016, July). Creating a water depth map from SAR flood extent and topography data. In *2016 IEEE International Geoscience and Remote Sensing Symposium (IGARSS)* (pp. 7635-7638). IEEE.

Matgen, P., Schumann, G., Henry, J. B., Hoffmann, L., & Pfister, L. (2007). Integration of SAR-derived river inundation areas, high-precision topographic data and a river flow model toward near real-time flood management. *International Journal of Applied Earth Observation and Geoinformation*, *9*(3), 247-263.

McGrath, H., Abo El Ezz, A., & Nastev, M. (2019). Probabilistic depth–damage curves for assessment of flood-induced building losses. *Natural Hazards*, *97*, 1-14.

McGrath, H., Bourgon, J. F., Proulx-Bourque, J. S., Nastev, M., & Abo El Ezz, A. (2018). A comparison of simplified conceptual models for rapid web-based flood inundation mapping. *Natural Hazards*, *93*, 905-920.

McMurray Aviation. Aereal photos taken from 6-7pm on April 27th. Facebook, 27 April 2020, www.facebook.com/117712211590120/posts/3398707506823891/ [Accessed 17 October 2020.

Menduni, G, and Riboni, V., A physically based catchment partitioning method for hydrological analysis. Hydrological Processes 14, 1943-1962 (2000).

Mester, B., Vogt, T., Bryant, S., Otto, C., Frieler, K., & Schewe, J. (2023). Human displacements from tropical cyclone Idai attributable to climate change. *EGUsphere*, *2023*, 1-19.

Mizukoshi, H., and Aniya, M., Use of Contour-Based DEMs for Deriving and Mapping Topographic Attributes. Photogrammetric Engineering & Remote Sensing 68(1), 83-93 (2002).

Mojtahed, V., Giupponi, C., Biscaro, C., Gain, A., & Balbi, S. (2013). Integrated assessment of natural hazards and climate change adaptation: II-The Serra methodology. *University Ca'Foscari of Venice, Dept. of Economics Research Paper Series No*, *7*.

Moore, I. D., Grayson, R. B., & Ladson, A. R. (1991). Digital terrain modelling: a review of hydrological, geomorphological, and biological applications. Hydrological processes, 5(1), 3-30.

Moore, I.D., O'Loughlin, E.M., and Burch G.J., A contour-based topographic model for hydrological and ecological applications. Earth Surface Processes and Landforms, 13, 305-320 (1988).

Nafziger, J., Kovachis, N., & Emmer, S. (2021, August). A Tale of Two Basins: The 2020 River Ice Breakup in Northern Alberta, Part I: The Athabasca River. In *Proceedings of the 21st Workshop on the Hydraulics of Ice Covered Rivers, Saskatoon, SK, Canada* (p. 22).

Nafziger, J., She, Y., & Hicks, F. (2016). Celerities of waves and ice runs from ice jam releases. *Cold Regions Science and Technology*, *123*, 71-80.

National Severe Storms Laboratory. (n.d.). Floods. Retrieved from https://www.nssl.noaa.gov/education/svrwx101/floods/

Natural Resources Canada, Government of Canada. (2020). Geo Deep Learning. GitHub repository. https://github.com/NRCan/geo-deep-learning

Necati, Gulbahar. (2016). A Comparison Study of Some Flood Estimation Methods in terms of Design of Water Structures. International Journal of Engineering, doi: 10.19072/IJET.15736

Nguyen, H. D., Dang, D. K., Nguyen, N. Y., Pham Van, C., Van Nguyen, T. T., Nguyen, Q. H., ... & Bui, Q. T. (2024). Integration of machine learning and hydrodynamic modeling to solve the extrapolation problem in flood depth estimation. *Journal of Water and Climate Change*, *15*(1), 284-304.

NOAA National Centers for Environmental Information (NCEI) U.S. Billion-Dollar Weather and Climate Disasters (2024). https://www.ncei.noaa.gov/access/billions/, DOI: 10.25921/stkw-7w73

Nobre, A. D., Cuartas, L. A., Hodnett, M., Rennó, C. D., Rodrigues, G., Silveira, A., & Saleska, S. (2011). Height Above the Nearest Drainage–a hydrologically relevant new terrain model. *Journal of Hydrology*, *404*(1-2), 13-29.

Nobre, A. D., Cuartas, L. A., Momo, M. R., Severo, D. L., Pinheiro, A., & Nobre, C. A. (2016). Hand contour: A new proxy predictor of inundation extent. Hydrological Processes, 30(2), 320–333. https://doi.org/10.1002/hyp.10581

Notti, D., Giordan, D., Caló, F., Pepe, A., Zucca, F., & Galve, J. P. (2018). Potential and limitations of open satellite data for flood mapping. *Remote sensing*, *10*(11), 1673.

NRCan. (2023). RICorDE. GitHub. https://github.com/NRCan/RICorDE

O'Callaghan, J. F., & Mark, D. M. (1984). The extraction of drainage networks from digital elevation data. *Computer vision, graphics, and image processing*, *28*(3), 323-344.

Pathak, K., & Kaushik, P. (2015). Analysis of time complexities and accuracy of depression filling algorithms in DEM. *IOSR J Comput Eng*, *17*(3), 26-34.

Pawłowski, B. (2019). Ice Jams: Causes and Effects. In Encyclopedia of Water (pp. 1-9). American Cancer Society.

Penton, D. J., Teng, J., Ticehurst, C., Marvanek, S., Freebairn, A., Mateo, C., ... & Pollino, C. (2023). The floodplain inundation history of the Murray-Darling Basin through two-monthly maximum water depth maps. *Scientific Data*, *10*(1), 652.

Pierdicca, N., Pulvirenti, L., & Chini, M. (2018). Flood mapping in vegetated and urban areas and other challenges: models and methods. *Flood monitoring through remote sensing*, 135-179.

Pistrika, Aimilia, George Tsakiris, and Ioannis Nalbantis. "Flood depth-damage functions for built environment." *Environmental Processes* 1 (2014): 553-572.

Planchon, O., & Darboux, F. (2002). A fast, simple and versatile algorithm to fill the depressions of digital elevation models. *Catena*, *46*(2-3), 159-176.

Public Safety Canada. (2022). Departing, rising: A flood risk management guidebook for local governments in Canada. Retrieved from https://www.publicsafety.gc.ca/cnt/rsrcs/pblctns/dptng-rsng-fld-rsk-2022/index-en.aspx

Qin, C., Zhu, A. X., Pei, T., Li, B., Zhou, C., & Yang, L. (2007). An adaptive approach to selecting a flow-partition exponent for a multiple-flow-direction algorithm. *International Journal of Geographical Information Science*, *21*(4), 443-458.

Ramp-Alberta. (n.d.). Clearwater River. Retrieved from http://www.ramp-alberta.org/river/hydrology/river+hydrology/clearwater+river.aspx

Rennó, C. D., Nobre, A. D., Cuartas, L. A., Soares, J. V., Hodnett, M. G., & Tomasella, J. (2008). HAND, a new terrain descriptor using SRTM-DEM: Mapping terra-firme rainforest environments in Amazonia. Remote Sensing of Environment, 112(9), 3469-3481.

Rieger, W. (1998). A phenomenon-based approach to upslope contributing area and depressions in DEMs. *Hydrological Processes*, *12*(6), 857-872.

Rokaya P., Morales L., Bonsal B., Wheater H., and Lindenschmidt K.-E. 2019. Climatic effects on ice-jam flooding of the Athabasca River: Ice phenology and flood probability. Hydrol. Sci. J. 64: 1265–1278.

Rokaya, P. (2018). *Impacts of climate and regulation on ice-jam flooding of northern rivers and their inland deltas* (Doctoral dissertation, University of Saskatchewan).

Scawthorn, C., Flores, P., Blais, N., Seligson, H., Tate, E., Chang, S., ... & Lawrence, M. (2006). HAZUS-MH flood loss estimation methodology. II. Damage and loss assessment. *Natural Hazards Review*, *7*(2), 72-81.

Schumann, G., Bates, P. D., Horritt, M. S., Matgen, P., & Pappenberger, F. (2009). Progress in integration of remote sensing–derived flood extent and stage data and hydraulic models. *Reviews of Geophysics*, *47*(4).

Schwanghart, W., Groom, G., Kuhn, N. J., & Heckrath, G. (2013). Flow network derivation from a high resolution DEM in a low relief, agrarian landscape. *Earth Surface Processes and Landforms*, *38*(13), 1576-1586.

Scorzini, A. R., & Frank, E. (2017). Flood damage curves: new insights from the 2010 flood in Veneto, Italy. *Journal of Flood Risk Management*, *10*(3), 381-392.

Soille, P. (2004)a. Optimal removal of spurious pits in grid digital elevation models. *Water Resources Research*, 40(12).

Soille, P. (2004)b. Morphological carving. *Pattern Recognition Letters*, *25*(5), 543-550.

Soille, P., J. Vogt, and R. Colombo. (2003) ."Carving and Adaptive Drainage Enforcement of Grid Digital ElevationModels. "Water Resources Research39: 1366–1378.doi:10.1029/2002WR001879

Statistics By Jim. (2024, March 29). Interquartile Range (IQR): How to Find and Use It. Retrieved from https://statisticsbyjim.com/basics/interquartile-range/

Sulong, S., & Romali, N. S. (2022). The role of socio-economic and property variables in the establishment of flood depth-damage curve for the data-scarce area in Malaysia. *Urban Water Journal*, *19*(8), 859-878.

Tarboton, D. G., Bras, R. L., & Rodriguez-Iturbe, I. (1991). On the extraction of channel networks from digital elevation data. *Hydrological processes*, *5*(1), 81-100.

Tarboton, D.G. 2016. "Terrain Analysis Using Digital Elevation Models (TauDEM)." Utah Water Research Laboratory, Utah State University. http://hydrology.usu.edu/taudem.

Tarboton, David G. (1997). A new method for the determination of flow directions and upslope areas in grid digital elevation models. *Water resources research*, *33*(2), 309-319.

Topp, M. J. (2014). LiDAR data for DEM generation and flood plain mapping.

Tretyak, K., Kukhtar, D., Prykhodko, M., Romaniuk, V., Bodnaruk, I., & Vyrstyuk, O. (2021, May). Opportunities and Limitations for Ground Motion Mapping Using InSAR Technique. In *Geoinformatics* (Vol. 2021, No. 1, pp. 1-6). European Association of Geoscientists & Engineers.

U.S. Geological Survey. (n.d.). Science - Water Resources - Mission Areas. U.S. Geological Survey. https://www.usgs.gov/mission-areas/water-resources/science

USU Watershed Sciences. (n.d.). PitRemove. Retrieved from https://hydrology.usu.edu/taudem/taudem5/help53/PitRemove.html

Wang, L. and Liu, H. 2006. An efficient method for identifying and filling surface depressions in digital elevation models for hydrologic analysis and modelling. International Journal of Geographical Information Science, 20(2): 193-213.

Wang, L., & Liu, H. (2006). An efficient method for identifying and filling surface depressions in digital elevation models for hydrologic analysis and modelling. *International Journal of Geographical Information Science*, *20*(2), 193-213.

Wang, T., Guo, X., Liu, J., Chen, Y., She, Y., & Pan, J. (2024). Ice Process Simulation on Hydraulic Characteristics in the Yellow River. Journal of Hydraulic Engineering, 150(3), 05024001.

Wang, Y. J., Qin, C. Z., & Zhu, A. X. (2019). Review on algorithms of dealing with depressions in grid DEM. *Annals of GIS*, *25*(2), 83-97.

Weatherstats. (2024). Fort McMurray yearly precipitation charts. Retrieved from https://fortmcmurray.weatherstats.ca/charts/precipitation-yearly.html

Whitebox Geospatial Analysis Tools. (n.d.). Fill Depressions. In Whitebox Geospatial Analysis Tools User Manual. Retrieved from https://www.whiteboxgeo.com/manual/wbt_book/available_tools/hydrological_analysis.html#FillDepressions

Whitebox Geospatial Analysis Tools. (n.d.). Hydrological analysis. Whitebox Geospatial Analysis Tools Manual. Retrieved from https://www.whiteboxgeo.com/manual/wbt_book/available_tools/hydrological_analysis.html#FillSingleCellPits

Wienhold, K. J., Li, D., Li, W., & Fang, Z. N. (2023). Flood Inundation and Depth Mapping Using Unmanned Aerial Vehicles Combined with High-Resolution Multispectral Imagery. Hydrology, 10(8), 158.

Wise, S., Assessing the quality for hydrological applications of digital elevation models derived from contours, Hydrology Processes14,1909-1929 (2000).

World Meteorological Organization. (n.d.). WMO Guidelines on flood mapping and management. Retrieved from https://library.wmo.int/viewer/51415?medianame=wmo_1123_en_#page=1&viewer=picture&o=bookmarks&n=0&q=

WT Tech. (2024, March 31). A guide to model calibration. Retrieved from https://wttech.blog/blog/2021/a-guide-to-model-calibration/

Wu, Y., Liu, Y., Hu, H., & Yang, C. (2009, October). Flow paths tracing from raster contours using distance transform. In *International Symposium on Spatial Analysis, Spatial-Temporal Data Modeling, and Data Mining* (Vol. 7492, pp. 1510-1519). SPIE.

Yamazaki, D., Ikeshima, D., Sosa, J., Bates, P. D., Allen, G. H., & Pavelsky, T. M. (2019). Merit hydro: A high-resolution global hydrography map based on latest topography dataset. Water Resources Research, 55(6), 5053–5073. https://doi.org/10.1029/2019wr024873

Yuan, S., Fan, W., & Jiang, C. (2023). The Profiles Based on Ridge and Valley Lines to Extract Shoulder Lines on the Loess Plateau. Remote Sensing, 15(2), 380.

Zare, S. E., & Groeneveld, J. G. (2022, June). Ice Jam Flooding in the Athabasca River at Fort McMurray – Validation of a Previously Developed Model to the 2020 Ice Jam Event.

Zheng, X., Tarboton, D. G., Maidment, D. R., Liu, Y. Y., & Passalacqua, P. (2018). River channel geometry and rating curve estimation using height above the nearest drainage. *JAWRA Journal of the American Water Resources Association*, *54*(4), 785-806.

Zwenzner, H., & Voigt, S. (2009). Improved estimation of flood parameters by combining space based SAR data with very high resolution digital elevation data. *Hydrology and Earth System Sciences*, *13*(5), 567-576.

Appendix A: Case Study Flood Events Evaluated

Validation (News, IDD, CDD, CFO, FiC)					Began	Ended	Province	Place	Event type	Evacuated	Rain (mm/tin	Associated (
				FloodsInCana	2017-4-4	2017-4-23	MB	LakeWinnipegosis, Assiniboine, Fisher, Souris, LowerRed, LakeMar				
News			ColoradoFloo	FloodsInCana	2017-04-19	2017-05-15	Quebec	Montreal, Otta	Heavy Rain and Snowmelt		70mm/12h	
News	International I	Canadian Dis			2017-05-07	2017-5-20	Ontario	Ottawa (Cum	Heavy rain	248	50mm/day	
News					2017-05-11	2017-5-20	B.C	Ottawa (Cum	Rainfall	3641	50mm/day	
	International I	Canadian Disaster Database			2017-8-28	2017-08-30	Ontario	Windsor, Tec	Heavy rain			
News					2018-01-12	n/a	New Brunswick		Ice Jam Floo	200		
News		Canadian Disaster Database			2018-02-16	2018-02-21	Ontario	Grand River	Heavy Rain a	4900	50mm/day	
News		Canadian Disaster Databa		FloodsInCana	2018-04-23	2018-05-13	New Brunswick		Heavy Rain a	1400	n/a	
News				FloodsInCana	2018-04-17	2018-04-25	Alberta		Snowmelt			
News	International Disaster Data		ColoradoFloo	FloodsInCana	2018-05-10	2018-5-23	B.C	Spallumchee	Heavy Rain a	4000		
News	n/a	Canadian Dis	ColoradoFloodObservatory		2018-08-07	2018-08-08	Ontario	Toronto/Whit	Heavy rain		70mm/2hours	
News	n/a				2018-12-11	n/a	Vancouver		Heavy rain		77mm/day	
				FloodsInCana	2019-04-14	2019-04-27	MB	Red River | LowerRed				
News	International I	Canadian Dis	ColoradoFloo	FloodsInCana	2019-04-18	2019-5-5	Quebec	Ontario, Nouv	Heavy Rain a	10000	n/a	Broken Dam /
News		Canada Disaster Database		FloodsInCana	2019-04-15	2019-04-15	Ontario	Kashechewa	Heavy Rain a	2500	72.4mm/12hr	
				FloodsInCana	2019-05-09	2019-05-22	Ontario	Ottawa River, French River | CentralOttawa				
				FloodsInCana	2019-05-22	2019-05-27	New Brunswi	StJohn				
News					2019-07-16	n/a	Saskatchewa	Edmonton, re	Heavy rain		34 mm/day	
				FloodsInCana	2019-10-19	2019-10-22	MB	Red River | LowerRed				
News					2020-01-30	2020-02-01	B.C	Cowichan Va	Heavy rain	30	75mm/day	
				FloodsInCana	2020-4-14	2020-5-10	MB	Red River | LowerRed				
				FloodsInCana	2020-6-10	2020-6-11	MB	Red River | LowerRed				
	International Disaster Database			FloodsInCana	2020-4-26	2020-5-8	Alberta	Peace River,	Ice Jam Flood			Rising tempe
News			ColoradoFloodObservatory		2020-07-01	2020-07-05	MB		Heavy rain		190mm/3days	
News					2021-06-03	n/a	B.C	Kitimat-Stikin	Heavy rain			
				FloodsInCana	2021-07-08	2021-07-21	YK	Headwaters Yukon				
News	International Disaster Data		ColoradoFloodObservatory		2021-11-13	2021-11-16	B.C	Fraser Valley	Heavy rain	20,000	277.5mm/2da	Slide (land, m
News	International Disaster Database			FloodsInCana	2022-04-01	2022-06-06	MB	Southern Mar	Heavy rain	1000	120m/day	
News	International Disaster Database			FloodsInCana	2022-06-06	2022-6-16	Alberta	Perry River, I	Ice jams, rain	250		
					2022-06-13	2022-6-30	YK	Liard River, Pelly River, Teslin, Carmacks				
News	n/a				2022-06-13	n/a	Sasketchewa	Rosetown &	Heavy rain		100mm/6hours	
News					2022-09-23	2022-09-24		Newfoundlan	Storm Surge / Huricane			

Appendix B: RICorDE Hydro-correction Evaluation

The table below outlines the hydro-correction algorithms evaluated under RICorDE. The black areas on the right side of the table indicate the DEM extent hydro-connected to the waterbody boundary, while the grey areas represent areas not hydro-connected. In essence, gaps in hydro-connection towards the stream indicate an incompatibility with the RICorDE tool. The hydro-correction algorithms evaluated include: BreachDepression, BreachDepressionLeastCost, FillDepressions, FillDepressionsPlanchonAndDarboux, FillSingleCellsPits, and FillDepressionsWangAndLiu.

algorithm	DEM (resampling)	parameters	analysis	results filename	ElevationAboveStream
wbt BreachDepressions	10m resolution			BreachDepression Ele vationAboveStream.tif	
wbt BreachDepressions	bilinear DEM, 10m resolution			BreachDepression_Bili near.tif	
wbt BreachDepressionsLeastCost	10m resolution	cells=4		LeastCost.tif	
	10m resolution	cell=50, maxz=1		BreachDepression_Lea stCost_c50_zunit1_EAS	
	10m resolution	cell=50, maxz=1, flatz=0.01	Manflow paths departing outside of the DEM area, leaving the algorithm unable to compute such value.	BreachDepression Lea stCost c50 z1 z0.01 E AS	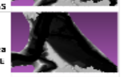
	10m resolution	cell=50, maxz=1, flatz=0.01, untick min& fill		BreachDepression_Lea stCost_c50_z1_z0.01_u ntickmin&fill EAS	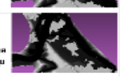
	10m resolution	cell=50, maxz=1, flatz=0.01, untick min		BreachDepression Lea stCost c50 z1 z0.01 u ntickmin_EAS	
	bilinear DEM, 10m resol	cell=50, maxz=1, flatz=0.01, untick min	Streams generated under urban area, hills edges are underestimated and stream not correctly generated.	bilinear dem breachdepressionleast cost untick min	
	10m resolution	cell=50, maxz=1, flatz=0.01, untick fill unbreached		BreachDepression Lea stCost_c50_z1_z0.01_u ntickfill_EAS	
	10m resolution	cell=50, maxz=2	failed to produce pixel in areas done flat with slope gradient variables identical for each of the three pixels on the drainage edge of the matrix.	BreachDepression Lea stCost c50 zunit2 EAS	
	10m resolution	cells=50		BreachDepression_Lea stCost_c50_EAS.tif	
	10m resolution	cell=50, untick min& fill		BreachDepression Lea stCost_c50_untickmin& fill EAS	
	10m resolution	cells=100		BreachDepression_Lea stCost_c100_EAS	
wbt BreachDepressionsLeastCost	bilinear DEM, 10m resol	cells: 4		LeastCost Bilinear.tif	
wbt FillDepressions	10m resolution		Flow obstructed by single cell generated elevations. Results suggest that flow accumulation might not be taken into account.	FillDepression.tif	
	10m resolution	Flat increment (z)=0.001	Results suggest that flow accumulation might not be taken into account in such scenarios.	FillDepression Yz0.001 .tif	
	10m resolution	Fix flat areas=N, Flat increment (z)=0.001		FillDepression Nz0.001 .tif	

	10m resolution	Fix flat areas=Y, Flat increment (z)=0.01		FillDepressionYz0o01_EAS	
	10m resolution	Fix flat areas=Y, Flat increment (z)=0.01, Maximum depth (z)=1	Small areas with flow paths obstructed by single-cell generated elevations.	FillDepression_Yz0o01z1	
	10m resolution	Fix flat areas=Y, Flat increment (z)=0.01, Maximum depth (z)=0.5	While the coverage expands to the full extent it also ends up generating unrealistic scale-like patterns under corrected areas	FillDepressionYz0o01z0o5_EAS	
wbt FillDepressions	bilinear DEM, 10m resolution			FillDepression_Bilinear.tif	
wbt FillDepressionsPlanchonAndD	10m resolution		might be same as 0.005	FillDepressionPlanchonAndDarboux_EAS	
	10m resolution	Flat increment=0.001		EAS_FillDepressionPlanchonAndDarboux0.001	
	10m resolution	Flat increment=0.001, Fix flat areas unticked		EAS_FillDepressionPlanchonAndDarboux0.001nofix	
	10m resolution	Flat increment=0.005	Undrawn pixels from the drainage flow path flowing outside of the area of interest.	EAS_FillDepressionPlanchonAndDarboux0.005	
	10m resolution	Flat increment=0.005, Fix flat areas unticked		EAS_FillDepressionPlanchonAndDarboux0.005nofix	
	10m resolution	Flat increment=0.01		EAS_FillDepressionPlanchonAndDarboux0.01	
	10m resolution	Flat increment=0.01, Fix flat areas unticked		EAS_FillDepressionPlanchonAndDarboux0.01nofix	
	10m resolution	Flat increment=0.05		EAS_FillDepressionPlanchonAndDarboux0.05	
	10m resolution	Flat increment=0.1		EAS_FillDepressionPlanchonAndDarboux0.1	
wbt FillDepressionsPlanchonAndD	bilinear DEM, 10m resolution			FillDepressionPlanchonAndDarboux_bilinear_EAS	
wbt FillDepressionsWangAndLiu	10m resolution			FillDepressionPlanchonAndDarboux_EAS	
wbt FillSingleCellPits	bilinear DEM, 10m resolution		Flow obstructed by single cell generated elevations. Results suggest that flow accumulation might not be taken into account	FillSingleCellPits_EAS_bilinear	

Appendix C: RICorDE Run Workflow

The workflow followed to run RICorDE and acquire the flood depth output was not the conventional one listed under its GitHub repository. It was in fact run under an alteration of the batch tutorial script. The simplified workflow followed to achieve the flood depth output presented in this thesis is outlined below (as of 2023/11/23):

1. Install both QGIS 3.22.8 and WhiteboxTools v2.1.0.
2. Make sure WhiteboxTools is integrated in the QGIS software via its plugin
3. Under the executable run_tutorial.bat, define the parameter file location on line 5, the output folder path on line 8, and the file directory for the .bat defining the pyQGIS environment path on line 14. Note: The .bat utilized to establish the pyQGIS environment path is encountered under the QGIS 3.22.8 program files, more specifically: C:\Program Files\QGIS 3.32.0\bin\python-qgis-ltr.bat
4. Define the WBT file path under the definitions.py file.
5. Run the tutorial batch script to test if RICorDE has been set up successfully. A short video showing what a successful run look is presented by the author on its GitHub page.
6. Define the case study inputs under the parameter.ini file.
7. Run RICorDE via run_tutorial.bat.
8. Extract the Depth layer from the output folder.
9. If required, alter the step 6 parameter.ini file and repeat step 7.

Appendix D: Accumulation stream as drainage HAND map

Below is the QGIS plugin script utilized to generate a HAND map in relation to a flow accumulation streamline. It is used in Section 5.2. and 5.3.1 for the comparison of depth grids and evaluation of HAND map flood extent delineation. It requires for QGIS to have the PCRaster plugin installed to work and was tested on QGIS 3.34.3. All credit to the methodology used in this script is given to Hans van der Kwast.

```
import processing
from qgis.PyQt.QtCore import QCoreApplication, QVariant
from qgis.core import (
QgsProcessing,
QgsProcessingAlgorithm,
QgsProcessingParameterRasterLayer,
QgsProcessingParameterNumber,
QgsProcessingParameterRasterDestination,
QgsRasterLayer)
from qgis.analysis import QgsRasterCalculator, QgsRasterCalculatorEntry
class ExAlgo(QgsProcessingAlgorithm):

    raster_layer = 'INPUT'
    stream_threshold = 'stream_threshold'
    OUTPUT = 'OUTPUT'

    def __init__(self):
        super().__init__()
    def name(self):
        return "pcrasterhand"
    def tr(self, text):
        return QCoreApplication.translate("exalgo", text)
    def displayName(self):
        return self.tr("HAND map derived from PCRaster plugin")
    def shortHelpString(self):
        return self.tr("Implements PCRaster tools plugin to generate a HAND map. \
        As explained by Hans van der Kwast")
    #def helpUrl(self):
    #    return "https://qgis.org"
    def createInstance(self):
        return type(self)()
    def initAlgorithm(self, config=None):

        self.addParameter(QgsProcessingParameterRasterLayer(
            self.raster_layer,
            self.tr("Input Digital Elevation Model"),
            [QgsProcessing.TypeRaster]))
```

```
        #STREAM THRESHOLD
        self.addParameter(QgsProcessingParameterNumber (
            self.stream_threshold,
            self.tr("Stream threshold"), defaultValue=3000
            ))

        self.addParameter(QgsProcessingParameterRasterDestination(
            self.OUTPUT,
            self.tr("Output Directory"),
            ))

    def processAlgorithm(self, parameters, context, feedback):
        raster_a = self.parameterAsRasterLayer(parameters, self.raster_layer,
context)
        stream_threshold_a = self.parameterAsString(parameters,
self.stream_threshold, context)
        output_path_raster_a = self.parameterAsOutputLayer(parameters,
self.OUTPUT, context)

        #STEPS
        #1.Convert to workable format
        processing.run("pcraster:converttopcrasterformat",\
            {'INPUT':raster_a,\
            'INPUT2':3,\
                'OUTPUT':'pcraster_temp'})
        #2. Generate flow direction
        processing.run("pcraster:lddcreate", \
            {'INPUT':'pcraster_temp',\

'INPUT0':0,'INPUT1':0,'INPUT2':9999999,'INPUT4':9999999,'INPUT3':9999999,'INP
UT5':9999999,\
                'OUTPUT':'lddcreate_temp'})
        #3. Create raster with scalar value 1.
        processing.run("pcraster:spatial", \
            {'INPUT':1,'INPUT1':3,\
            'INPUT2':'lddcreate_temp',\
                'OUTPUT':'scalar_temp'})
        #4. Generate accumulated material flowing downstream
        processing.run("pcraster:accuflux", \
            {'INPUT':'lddcreate_temp',\
            'INPUT2':'scalar_temp',\
                'OUTPUT':'accuflux_temp'})
        #5. Extract accumulated material
        processing.run("pcraster:spatial", \
            {'INPUT':stream_threshold_a,'INPUT1':3,\
            'INPUT2':'accuflux_temp',\
                'OUTPUT':'spatial_temp'})
```

```
    #6. Clean
    processing.run("pcraster:comparisonoperators", \
      {'INPUT':'accuflux_temp',\
      'INPUT1':1,'INPUT2':'spatial_temp',\
        'OUTPUT':'comparison_operator_temp'})
    #7. Clean
    processing.run("pcraster:uniqueid", \
      {'INPUT':'comparison_operator_temp',\
        'OUTPUT':'uniqueid_temp'})
    #8. Convert from scalar to nominal
    processing.run("pcraster:convertdatatype", \
      {'INPUT':'uniqueid_temp',\
      'INPUT1':1,\
        'OUTPUT':'convertlayerdatatype_temp'})
    #9. Generate sub-catchments
    processing.run("pcraster:subcatchment", \
      {'INPUT1':'lddcreate_temp',\
      'INPUT2':'convertlayerdatatype_temp',\
        'OUTPUT':'subcatchment_temp'})
    #10. Areaminimum
    processing.run("pcraster:areaminimum", \
      {'INPUT':'subcatchment_temp',\
      'INPUT2':'pcraster_temp',\
        'OUTPUT':'areaminimum_temp'})
    #11. HAND elevation subtraction
    #RasterCalculator inputs and outputs
    areaminimum_rastercalculator_temp                              =
QgsRasterLayer(r'areaminimum_temp')
    pcraster_rastercalculator_temp = QgsRasterLayer(r'pcraster_temp')

    #preparing layers for RasterCalculator
    entries = []
    amr = QgsRasterCalculatorEntry()
    amr.ref = 'amin@1'
    amr.raster = areaminimum_rastercalculator_temp
    amr.bandNumber = 1
    entries.append( amr )
    pcr = QgsRasterCalculatorEntry()
    pcr.ref = 'pcr@2'
    pcr.raster = pcraster_rastercalculator_temp
    pcr.bandNumber = 1
    entries.append( pcr )

    #Process calculation with input extent and resolution
    calc = QgsRasterCalculator( 'pcr@2 - amin@1',
                          output_path_raster_a,
                          'GTiff',
                          pcraster_rastercalculator_temp.extent(),
```

```
                    pcraster_rastercalculator_temp.width(),
                    pcraster_rastercalculator_temp.height(),
                    entries )

calc.processCalculation()

results = {}
results[self.OUTPUT] = output_path_raster_a
return results
```

Appendix E: Generating Streams from Flow Accumulation

During the evaluation of depression fixing algorithms, disparities were visually evident in stream generation via flow accumulation using breach hydro-correction methods. The breach method resulted in the failure to produce a continuous streamline along the river. Figures 26 and 27 depict a linear stream with its threshold set at high accumulation zones, presenting two depression-fixing algorithms: Wang and Liu (2006) in Figure 26 and BreachDepressionLeastCost in Figure 27. Figure 26 highlight the following observations: a) Incorrect stream generation under the Downtown area, a high accumulation zone. b) Correct stream generation achieved using a higher threshold. Figure 27 highlight the following observation: a) non-continuous stream and erroneous stream under downtown area. b) no stream under downtown but non-continuous stream generated. These results underscore the influence of hydrologic correction on the threshold and emphasize that it may not always portray its full extent. The generation of streams via flow accumulation was an important part of the HAND map generation since drainage was derived from the following (Figure 26b).

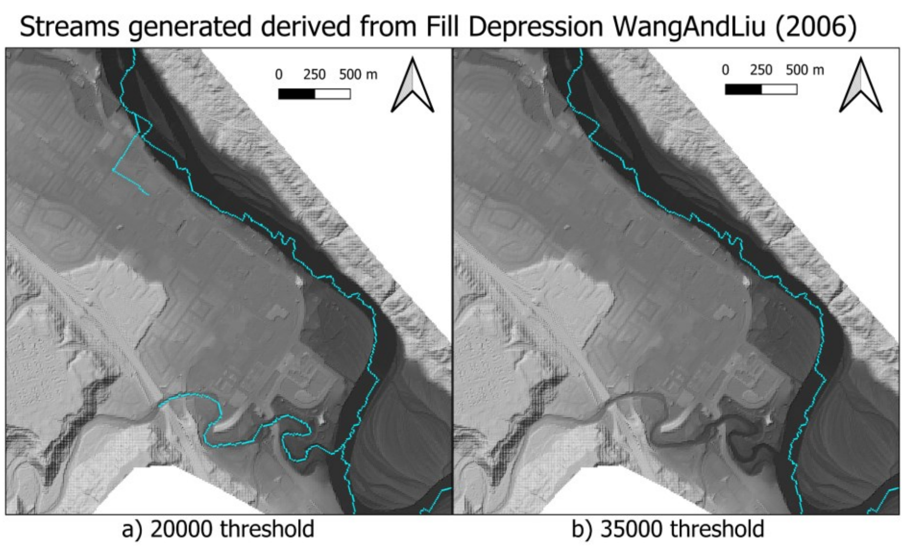

Figure 26. Threshold calibration on streams generated of a Wang and Liu (2006) depression fixed DEM.

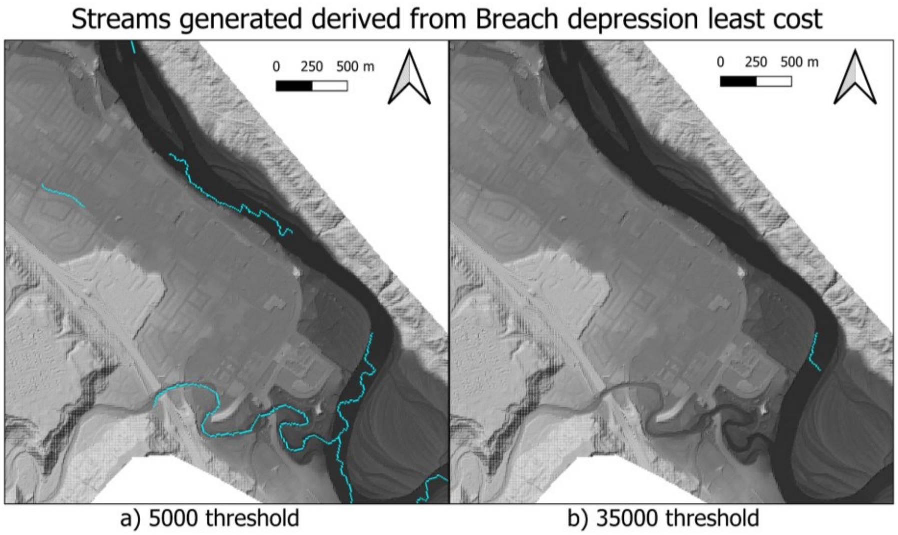

Figure 27. Threshold calibration on streams generated of a BreachDepressionLeastCost fixed DEM.

Appendix F: Interpolation Method Visualization

To visualize the difference between interpolation and a flat WSE, it was plotted in Figure 27. Abrupt differences in water surface elevation were observed on the interpolated IDW surface layer, likely resulting from the lack of processing of the flooded boundaries. While Euclidean distance was evaluated, it was not presented in this context. Euclidean distance was characterized by straight-line vertical transitions.

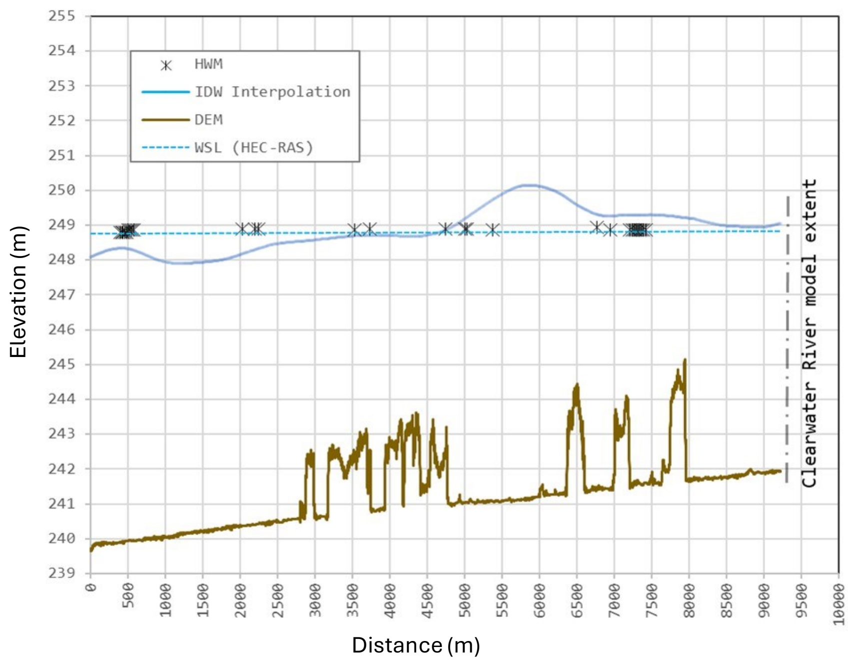

Figure 28. Clearwater River terrain profile for the model WSE and DEM, surveyed HWM, and IDW interpolated flood surface.